**Growth and Electronic Properties of GaAsN and GaAsBi Alloys**

**by**

**Richard L. Field III**

A dissertation submitted in partial fulfillment
of the requirements for the degree of
Doctor of Philosophy
(Physics)
in the University of Michigan
2015

Doctoral Committee:

Professor Rachel S. Goldman, Co-Chair
Professor Cagliyan Kurdak, Co-Chair
Professor Roy Clarke
Assistant Professor Emmanouil Kioupakis
Associate Professor Vanessa Sih

©2015 Richard L. Field III
All rights reserved

## Acknowledgements

First, I would like to thank my advisors, Prof. Rachel Goldman and Prof. Cagliyan Kurdak, for their guidance and support throughout my studies at the University of Michigan. I would also like to thank my thesis committee members, Roy Clarke, Emmanouil Kioupakis, and Vanessa Sih, for their valuable discussions and suggestions.

This dissertation would not have been possible without the help of my collaborators. Especially, I would like to acknowledge Marta Luengo-Kovac and Brennan Pursley in Prof. Sih's group at the University of Michigan.

I thank all of my fellow group members for their help and support. In particular, I would like to thank Steven Wolgast, Yun Suk Eo, Tim Jen, Jordan Occena, Simon Huang, Sunyeol Jeon, Davide Del Gaudio, Myungkoo Kang, and Jia-Hung Wu for their assistance, discussions, suggestions, and encouragement.

I gratefully acknowledge support from the National Science Foundation (Grant Nos. DMR 1006835 and DMR 1410282), monitored by C. Ying and H. Wang.

Finally, my greatest gratitude to my parents, sister, and friends, for their love and support.

## Table of Contents

**Acknowledgements** ........ ii

**List of Figures** ........ v

**List of Tables** ........ xiii

**List of Appendices** ........ xv

**Abstract** ........ xvi

**Chapter 1 Introduction** ........ 1

1.1 Overview ........ 1
1.2 Synthesis of GaAsN and GaAsBi alloys ........ 3
1.3 Properties of GaAsN and GaAsBi alloys ........ 5
1.4 Device applications ........ 11
1.5 Dissertation objectives ........ 13
1.6 Outline of dissertation ........ 14
1.7 Figures ........ 16
1.8 Tables ........ 25
1.9 References ........ 26

**Chapter 2 Experimental Procedures** ........ 35

2.1 Overview ........ 35
2.2 Molecular-beam epitaxy ........ 37
2.3 Rapid-thermal annealing ........ 44
2.4 High-resolution X-ray diffraction ........ 44
2.5 Atomic force microscopy ........ 45
2.6 Scanning electron microscopy ........ 45
2.7 Ion beam analysis ........ 46
2.8 Hall and magnetoresistance measurements ........ 47
2.9 Photoluminescence ........ 52
2.10 Figures ........ 53

2.11 References ..... 66

**Chapter 3 GaAsN: Electronic States ..... 68**
3.1 Overview ..... 68
3.2 Background ..... 69
3.3 Experimental details ..... 73
3.4 Origins of persistent photoconductivity ..... 74
3.5 Using PPC to probe the metal-insulator transition in GaAsN ..... 80
3.6 Conclusions ..... 82
3.7 Figures ..... 84
3.8 References ..... 98

**Chapter 4 GaAsBi: Growth and Properties ..... 103**
4.1 Overview ..... 103
4.2 Background ..... 104
4.3 Experimental details ..... 105
4.4 Growth of GaAsBi ..... 107
4.5 Optical and electronic properties of GaAsBi alloys ..... 112
4.6 Conclusions ..... 115
4.7 Figures ..... 116
4.8 References ..... 128

**Chapter 5 Summary and Suggestions for Future Work ..... 132**
5.1 Summary ..... 132
5.2 Suggestions for future work ..... 134
5.3 Figures ..... 139
5.4 References ..... 141

**Appendices ..... 144**

## List of Figures

Figure 1.1 Surface reconstructions observed during growth of GaAsN films: growth rate vs substrate temperature for (a) $As_4$/Ga BEP ratio ~30; (b) $As_2$/Ga BEP ratio ~20; and (c) $As_2$/Ga BEP ratio ~10. Solid (open) symbols denote 500 nm (10–100 nm) thick GaAsN films. The shaded regions indicate the conditions which lead to significant surface roughness, referred to as the "forbidden window." Reprinted with permission from Ref. 39. (Copyright 2007, AIP Publishing LLC). ....16

Figure 1.2 Bandgap energy vs. bond length for various III-V compound and elemental semiconductors. The points correspond to the bandgap energy and bond length for each elemental and binary semiconductor, and connecting lines correspond to alloys. The quaternary GaAsNBi can maintain lattice matching to GaAs using a relationship [Bi] ≈ 1.7[N], over a variety of bandgap energies. Adapted and printed with permission from Ref. 117. (Copyright 2010, Yu Jin). ....17

Figure 1.3 Schematic of dispersion relationships for sub-bands (solid lines) of GaAsN using the band anti-crossing model. The dotted lines represent the unperturbed energies of the N-induced localized states and the GaAs conduction band; the solid lines represent the hybridized $E_+$ and $E_-$ sub-bands. Reprinted with permission from Ref. 117 (Copyright 2010, Yu Jin). ....18

Figure 1.4 Calculated dispersion relationships for sub-bands of GaAsBi using the valence band anti-crossing model. A Bi-induced localized state resonant with the valence band splits the heavy-hole (HH), light-hole (LH), and spin-orbit (SO) sub-bands of the valence band into two groups, $E_+$ ($HH^+$, $LH^+$, $SO^+$) and $E_-$ ($HH^-$, $LH^-$, $SO^-$). Reprinted with permission from Ref. 75. (Copyright 2007, AIP Publishing LLC). ....19

Figure 1.5 Reduction of bandgap energy, $E_g$, and splitting of the spin-orbit sub-band, $\Delta_{SO}$, as a function of percent Bi fraction for GaAsBi alloys, as reported by Batool.[77] There is a crossover such that $\Delta_{SO} > E_g$ at a Bi fraction of 0.105. Reprinted with permission from Ref. 77 (Copyright 2012, AIP Publishing LLC). ....20

Figure 1.6 GaAsN band structure, and N cluster states, considered by the linear combination of isolated N resonant states (LCINS) model. ....21

Figure 1.7 Electron mobility, $\mu_e$, vs. N composition, $x$, for bulk $GaAs_{1-x}N_x$ films of various targeted free carrier concentrations, in units of $cm^{-3}$. The calculated $\mu_e$ by Fahy and Vaughan are included for comparison to experimental values. The measured $\mu_e$ decreases substantially with increasing $x$, and is lower than the prediction of all the theories....22

Figure 1.8 Seebeck coefficient, $S$, as a function of temperature for various GaAsN alloys. N incorporation significantly enhances $|S|$ in the $T < 140$ K regime, due to increased electron-phonon coupling, often termed phonon drag. For the $T > 140$ K regime, $S$ decreases monotonically with $T$, due to electron diffusion driven by the $T$ gradient. Reprinted with permission from Ref. 94 (Copyright 2010, American Physical Society)....23

Figure 1.9 A schematic of a GaAsN/GaAsBi superlattice. GaAsBi and GaAsN induce a bandgap reduction due to a shift in the valence band ($\Delta E_v$) and conduction band ($\Delta E_c$), respectively....24

Figure 2.1 Schematic of the Modified Varian Gen II molecular-beam epitaxy system. The radio frequency plasma source (separated from the main chamber by a gate valve) and seven solid sources (Ga, In, Al, Si, Be, Bi, and As cracker) are each located in one of the effusion cell ports....53

Figure 2.2 Schematic of the Riber Compact 21 molecular-beam epitaxy system. Seven solid sources (Ga, In, Al, Si, Be, Bi, and As cracker) are each located in one of the effusion cell ports....54

Figure 2.3 Reflection high-energy electron diffraction intensity as a function of measurement time for a typical GaAs growth rate calibration, for which the Ga and As shutters are always open....55

Figure 2.4 Reflection high-energy electron diffraction intensity as a function of measurement time for an incorporation rate ratio measurement. Here, the Ga shutter is always open; the As shutter closing, reopening, and the surface reconstruction recovery are labeled as $t_1$, $t_2$, and $t_3$, respectively.....56

Figure 2.5 Cross section of $GaAs_{1-x}N_x$ film structure grown by molecular-beam epitaxy, including layer thickness and substrate temperature, $T_s$. ....57

Figure 2.6 Cross section of $GaAs_{1-y}Bi_y$ film structure grown by molecular-beam epitaxy, including layer thickness and substrate temperature, $T_s$. ....58

Figure 2.7 Bi fraction, $y$, vs. Bi:Ga BEP Ratio, κ, for $GaAs_{1-y}Bi_y$:(Si) films. The target Bi fraction can be estimated from a linear interpolation of the $y$ vs. κ data....59

Figure 2.8 Schematic of high-resolution X-ray rocking curve geometries: (a) symmetric (004) scan, and (b) asymmetric (224) scan. Reprinted with permission from Ref. 13 (Copyright 2010, Yu Jin).....60

Figure 2.9 Schematic of a 4-probe measurement from a sample of arbitrary shape, with contacts on the perimeter located at *M*, *N*, *O,* and *P*. ....................................61

Figure 2.10 Schematic of a typical symmetric Van der Pauw specimen wired for (a) longitudinal, $V_{xx}$, and (b) transverse, $V_{xy}$, transport measurements. ................62

Figure 2.11 Schematic of a photolithographically defined 6-arm Hall bar used for transport measurements. Hall bars enable simultaneous measurements of voltage in both the longitudinal, $V_{xx}$, and transverse, $V_{xy}$, directions. .............63

Figure 2.12 Schematic of the cryostat used for variable-temperature transport measurements. The cryostat is equipped with a superconducting magnet ranging from –8 to +8 Tesla, and can reach temperatures from 1.5 to 300 K. For persistent photoconductivity studies, a light-emitting diode was mounted on the sample holder directly beside the sample. Reprinted with permission from Ref. 13 (Copyright 2010, Yu Jin). ................................................................64

Figure 2.13 Schematic of the liquid nitrogen cryostat used for 77-K resistivity measurements. For persistent photoconductivity studies, a light-emitting diode was mounted on the sample holder directly beside the sample. Adapted and printed with permission from Ref. 13 (Copyright 2010, Yu Jin)......................65

Figure 3.1 Large-lattice relaxation model for persistent photoconductivity. An energy barrier, $E_c$, hinders the relaxation of the photoexcited state to the ground state ..........................................................................................................84

Figure 3.2 Electron effective mass, $m_e$*, as a function of N fraction, $x$, for GaAsN, determined by various experimental methods and calculations for (a) Si doping, (b) Te doping, and (c) Se doping. Our measured value of $m_e$* (the star symbol) and lower-bounds of $m_e$* (the upward-pointing arrows) for Si-doped GaAsN is consistent with predictions of the LCINS model, which considers N clustering. Reprinted with permission from [a]Ref. 32 (Copyright 2012, American Physical Society). ....................................................................................85

Figure 3.3 Interdonor distance, $a$*, vs. critical carrier concentration, $n_c$, for a variety of materials. An interpolation of the data reveals the universality of the Mott criterion, corresponding to the metal-insulator transition. Reprinted with permission from Ref. 35 (Copyright 1978 by the American Physical Society).. ..........................................................................................................86

Figure 3.4 Persistent photoconductivity (PPC) magnitude plotted as a function of N fraction for $GaAs_{1-x}N_x$ films measured at 77 K. Although the PPC effect is negligible for $x < 0.006$, it increases with $x$ for $x > 0.006$. The open square shows the suppression of the PPC magnitude due to rapid-thermal annealing (RTA) at 763 °C on a $GaAs_{0.985}N_{0.015}$ film. The inset shows a typical PPC

trace for a $GaAs_{0.985}N_{0.015}$ film, with an illumination duration from $t$ = 300 to 1000 s. ....87

Figure 3.5a Examples of persistent photoconductivity data and analysis for a $GaAs_{0.987}N_{0.013}$:Te film. The normalized conductivity, $\sigma_t^N$, with $t$ = 0 defined as the instant of illumination termination, plotted as a function of time and measured at various $T$. ....88

Figure 3.5b Examples of persistent photoconductivity data and analysis for a $GaAs_{0.987}N_{0.013}$:Te film. Plot of $\sigma_t^N$ in the form of a stretched-exponential, $\sigma_t^N \propto \exp\left[-\left(\frac{t}{\tau}\right)^\beta\right]$, where the $x$-intercept at $y$ = 0 is identified as the characteristic decay time, $\tau$. The inset shows a plot of ln($\tau$) vs. 1000/$T$, from which the electron-capture energy, $E_c$, is determined. ....89

Figure 3.6 Free carrier concentration, $n$, as a function of 1000/$T$ for various GaAsN films in comparison with that of GaAs. For GaAs $n$ is $T$ independent, while for GaAsN two distinct regimes of $n$ are apparent: for high measurement $T$, $n$ increases exponentially with increasing $T$; for low measurement $T$, $n$ is $T$-independent. For $n > n_s$, $\sqrt{n(n-n_S)}$ is also plotted vs. 1000/$T$ in open circles. A two-level system formalism is then used to extract the activation energy of N-induced deep donor states, $E_a$. ....90

Figure 3.7 Activation energy, $E_a$, plotted as a function of N fraction, $x$, for $GaAs_{1-x}N_x$ films. The activation energy decreases with increasing $x$, signifying that the N-related deep donor state moves toward the conduction band edge as $x$ increases. ....91

Figure 3.8 Free carrier concentration, $n$, as a function of 1000/$T$, for GaAsN films annealed at various temperatures via rapid-thermal annealing (RTA): (a) a $GaAs_{0.985}N_{0.015}$:Si film, and (b) a $GaAs_{0.984}N_{0.016}$:Te film.. ....92

Figure 3.9 Interstitial N concentration vs. total N concentration for $GaAs_{1-x}N_x$ films with various N fractions, $x$. Linear interpolation of the interstitial N concentration for as-grown films suggests that approximately 20% of N are incorporated interstitially, as indicated in the plot. Following rapid-thermal annealing (RTA), the interstitial N concentration decreases to ~10%, while the total N concentration remains constant to within experimental error. ....93

Figure 3.10 Schematic energy diagram of "ground" (left) and "photoexcited" (right) configurations of GaAsN. Prior to illumination, carriers reside in the ground N-pair [either $(N\text{-}N)_{As}$ or $(N\text{-}As)_{As}$] state. Upon illumination, the carriers are excited from the N-pair state to the conduction-band edge (CBE), leading to enhanced conductivity. Carrier photoexcitation leads to a re-arrangement of

the N-pair molecular bonds, with the photoexcited N-pair state at a higher energy than that of the ground N-pair state, namely above the CBE. In order for carriers to return to the ground N-pair state (resulting in a decay of the conductivity with respect to its pre-illumination value), the ground N-pair state configuration must be restored by overcoming the electron-capture barrier, $E_c$. ....................94

Figure 3.11 Resistivity, $\rho$, as a function of temperature, $T$, for a $GaAs_{0.987}N_{0.013}$:Si film. Illuminating the film induces persistent photoconductivity, thereby increasing $n$ of the film from 2.4 x $10^{17}$ to 3.3 x $10^{17}$ at saturation of the PPC effect.. ...95

Figure 3.12 Conductivity, $\sigma$, vs. $T^{1/3}$, for a $GaAs_{0.987}N_{0.013}$:Si film. Illuminating the film induces persistent photoconductivity, thereby increasing $n$ of the film from 2.4 x $10^{17}$ to 3.3 x $10^{17}$ at saturation of the PPC effect. For each illumination, $\sigma_{min}$ is determined from the $y$-intercept in the plot of $\sigma$ vs. $T^{1/3}$.. ....................96

Figure 3.13 Carrier concentration, $n$, vs. residual conductivity, $\sigma_{min}$, for a $GaAs_{0.987}N_{0.013}$:Si film, where $n$ was varied using the persistent photoconductivity effect. To determine $n_c$, we take a linear interpolation of $n$ vs. $\sigma_{min}$ for all of the illuminations; then, $n = n_c$ when $\sigma_{min} = 0$. ....................97

Figure 4.1 Scanning electron microscopy, corresponding energy dispersive X-ray spectroscopy (EDX), and Atomic force microscopy (AFM) images for [(a),(e),(i)] Ga-rich growth using $As_2$, [(b),(f),(j)] As-rich growth using $As_2$, [(c),(g),(k)] Ga-rich growth using $As_4$, and [(d),(h),(l)] As-rich growth using $As_4$. In the EDX images, red, green, and blue correspond to Ga, As, and Bi, respectively. The gray-scale ranges displayed in the AFM images are (j) 60 nm, (k) 160 nm and (l) 10 nm. For the phase AFM image in (i), the gray-scale range corresponds to 20°. .................... 116

Figure 4.2 Bi incorporation into GaAs, as a function of growth rate and V/III BEP ratio, for various GaAs(Bi) films grown using either $As_2$ or $As_4$. The solid line separates films grown with $As_2$ and $As_4$, with films grown using $As_2$ in the lower-left-hand corner of the plot. All films were exposed to As, Ga and Bi flux. Films with Bi incorporation (no Bi incorporation) are shown as solid (open) symbols. For films grown using $As_2$, a dashed line separates films with Bi incorporation from films without Bi incorporation, with Bi incorporation for Group V/III BEP ratios $\leq$ 6. .................... 117

Figure 4.3 Bi incorporation mechanisms for growth using $As_2$ (left) and $As_4$ (right). We show the surface reconstruction and consider if the active As species can favorably replace Bi dimers on the growth surface. For growth using $As_2$, $As_2$ incorporates into GaAs, replacing surface $Bi_2$. For growth using $As_4$, two $As_4$ interact at the surface, each breaking into 2 $As_2$ and incorporating one pair while the other is released .................... 118

Figure 4.4 Reflection high-energy electron diffraction patterns collected along [110] and $[1\bar{1}0]$ axes during GaAs(Bi):(Si) film growth. [(a), (b)] (2 x 4) pattern during GaAs growth at 600 °C; [(c), (d)] streaky (2 x 3) pattern during GaAs(Si) growth at 280 °C; [(e), (f)] dim (2 x chevron) pattern during *p*-type GaAs(Bi):Si growth at 280 °C; [(g), (h)] streaky (1 x 3) pattern during *n*-type GaAs(Bi):Si growth at 280 °C. .......... 119

Figure 4.5 Carrier types and concentrations ($x10^{18}$ $cm^{-3}$) for GaAs(Bi):Si films: arsenic beam-equivalent pressure (BEP) vs. Ga BEP, with growth rate on the upper *x*-axis. We note that the growth rate *x*-axis applies to data in the As-rich growth regime. A dotted line indicates the regime where the Group V/III BEP ratio is equal to 10, "BEPratio10". All GaAsBi:Si films above (below) the BEPratio10 line are *n*-type (*p*-type). In addition, along the BEPratio10 line, there is a carrier-type conversion from *n*-type to *p*-type as the growth rate increases (from 0.25 to 2.0 μm/hr), consistent with the growth rate dependence of the stoichiometry threshold reported in Ref 31 .......... 120

Figure 4.6 Surface reconstructions for GaAsBi films grown under Ga-rich (left) and As-rich (right) conditions. Films grown under Ga-rich conditions have (2 x 1) reconstructed surfaces, and films grown under As-rich conditions have (*n* x 3) reconstructed surfaces. The (2 x 1) reconstructed surfaces have significantly more Group V sites per unit area than the (*n* x 3) reconstructed surfaces .......... 121

Figure 4.7 (a) In-plane, $a_{\parallel}$, and perpendicular, $a_{\perp}$, lattice parameters and (b) FWHM of the (004) GaAsBi diffraction peak, both as a function of Bi fraction, *y*. For $x < 0.04$, $a_{\perp}$ increases with increasing *y*, independent of doping type and concentration. For $y > 0.04$, $a_{\parallel}$ begins to increase while $a_{\perp}$ is nearly constant, suggesting that the film lattice has begun to relax to its intrinsic lattice parameter. For undoped GaAsBi and *n*-type GaAsBi:Si with $y < 0.04$, the FWHM of the GaAsBi peak is nearly constant; for $y > 0.04$, the FWHM increases with *y*. For *p*-type GaAsBi:Si, the FWHM of the GaAsBi peak increases monotonically with *y*. .......... 122

Figure 4.8 Symmetric (004) high-resolution X-ray rocking curves for GaAsBi films of various Bi fraction, *y*. The peak separation between the GaAs and GaAsBi diffraction peak increases as *y* increases. Furthermore, for $y < 0.04$, Pendellosung fringes are apparent, indicating smooth epilayer surfaces and interfaces .......... 123

Figure 4.9 Peak energy of photoluminescence data (10 K) as a function of Bi fraction, *y*, for films grown with $As_2$ and $As_4$. The inset shows a typical PL trace for a $GaAs_{0.969}Bi_{0.031}$:Si film. There is a similar energy decrease per percent Bi fraction, $\Delta E/y$, for films grown with $As_2$ vs. $As_4$.. .......... 124

Figure 4.10 Scanning electron microscopy, corresponding energy dispersive X-ray spectroscopy (EDX), and atomic force microscopy (AFM) images for [(a),

(d), (g)] *n*-type $GaAs_{0.992}Bi_{0.008}$:Si, as well as *p*-type $GaAs_{0.991}Bi_{0.009}$:Si [(b), (e), (h)] before and [(c), (f), (i)] after etching with HCl:$H_2$0 (1:3). Etching in HCl removes Ga droplets from GaAsBi:Si films. In the EDX images, red, green, and blue correspond to Ga, As, and Bi, respectively. The gray-scale ranges displayed in the AFM images are (c) 10 nm, (f) 160 nm, and (i) 100 nm. ... 125

Figure 4.11 Conductivity vs. carrier concentration for bulk $GaAs_{1-y}Bi_y$:Si films, in comparison with literature reports for GaAsBi films doped with various impurities. The dashed lines form an envelope corresponding to mobilities of ~2300 and ~45 $cm^2/(V\text{-}s)$ for *n*-type and *p*-type films, respectively. The *n*- vs. *p*-type doping of GaAsBi:Si is controlled by varying the Group V/III beam-equivalent pressure ratio and/or growth rate. We demonstrate *n*-type mobilities up to 2500 $cm^2/(V\text{-}s)$ ($n = 8 \times 10^{17}$ $cm^{-3}$), higher than previously reported electron mobilities for GaAsBi For our *n*-type films grown near the stoichiometry threshold, mobilities lie near the mid-range of the envelope. For our *p*-type films with bismuth fractions up to 0.05, free carrier concentrations in excess of $5 \times 10^{18}$ $cm^{-3}$ are achieved, a significant increase over literature reports of ~$2 \times 10^{18}$ $cm^{-3}$. ........ 126

Figure 4.12 Mobility vs. Bi fraction, *y*, for bulk $GaAs_{1-y}Bi_y$:Si films, in comparison with literature reports for GaAsBi films doped with various impurities. Our films of low and high doping levels are plotted as squares and circles, respectively. The *n*- vs. *p*-type doping of GaAsBi:Si is controlled by varying the Group V/III beam equivalent pressure ratio and/or growth rate. Our *n*-type films exhibit electron mobilities as high as 2500 $cm^2/(V\text{-}s)$ ($n = 8 \times 10^{17}$ $cm^{-3}$), higher than previously reported electron mobilities for GaAsBi. Our *p*-type films exhibit *x*-independent hole mobilities as high as 70 $cm^2/(V\text{-}s)$ ($p = 1.9$ to $4.0 \times 10^{17}$ $cm^{-3}$), in contrast to Be- and C-doped GaAsBi, where a decrease in hole mobility with increasing *x* has been reported. ........ 127

Figure 5.1 GaAsN heterostructure with a two-dimensional electron gas and a GaAsN layer, including a built-in back gate to control the Fermi level energy relative to the N-induced levels. The electron mobility is expected to decrease significantly when the Fermi level is resonant with the N-related states;[1] thus, the mobility measurements can be used as a spectroscopic probe of the N-induced levels... ........ 139

Figure 5.2 Carrier types and droplet surface coverage (percent) for GaAs(Bi):Si films: arsenic beam-equivalent pressure (BEP) vs. Ga BEP, with growth rate on the upper *x*-axis. We note that the growth rate *x*-axis applies to data in the As-rich growth regime. A dotted line indicates the regime where the Group V/III BEP ratio is equal to 10, "BEPratio10". The droplet surface coverage decreases as either the V/III BEP ratio or growth rate is increased. ........ 140

Figure B.1 Rutherford backscattering data from a thin 200-nm $GaAs_{0.979}Bi_{0.021}$ film: counts of backscattered particles as a function of energy of the backscattered particle. For thin films, counts from the Bi peak ($I_{Bi}$) does not merge into the Ga/As peak ($I_{Ga} + I_{As}$). ........ 154

Figure B.2 Rutherford backscattering data from a thick 300-nm $GaAs_{0.974}Bi_{0.026}$ film: counts of backscattered particles as a function of energy of the backscattered particle. For thick films, counts from the Bi peak ($I_{Bi}$) merge into the Ga/As peak ($I_{Ga} + I_{As}$). ........ 155

Figure B.3 Size analysis of a (a) $GaAs_{0.954}Bi_{0.046}$:Si film. (b) For a high threshold, 159, large particles are detected, and small particles are only partially detected. (b) For a low threshold, 86, small particles are detected, but background noise is amplified, especially around larger droplets........ 156

Figure E.1 Non-ideal Van der Pauw samples: (a) a contact is extended along the perimeter, (b) a contact is extended radially, and (c) a contact is not on the sample edge ........ 170

## List of Tables

Table 1.1 Properties of Group V elements, including the electronic configuration, atomic mass, covalent radius, and Pauling's electronegativity. ......................25

Table A.1 Growth parameters for GaAsBi:(Si) films grown using $As_4$, including growth rate, epilayer thickness, substrate temperature, As/Ga beam-equivalent pressure (BEP) ratio, Bi/Ga BEP ratio, V/III BEP ratio, and Si cell temperature for GaAsBi:(Si) films of various Bi fractions, $y$. .......................................... 145

Table A.2 Growth parameters for GaAsBi:(Si) films grown using $As_2$, including growth rate, epilayer thickness, substrate temperature, As/Ga beam-equivalent pressure (BEP) ratio, Bi/Ga BEP ratio, V/III BEP ratio, and Si cell temperature for GaAsBi:(Si) films of various Bi fractions, $y$. .......................................... 146

Table C.1 High-resolution X-ray rocking curve data, including (004) peak separation, (224) peak separation, in-plane lattice parameter, $a_{\parallel}$, out-of-plane lattice parameter, $a_{\perp}$, (004) GaAsBi peak width, and (224) GaAsBi peak width, for GaAsBi:Si films of various Bi fractions, $y$ .......................................... 159

Table C.2 Rutherford backscattering spectroscopy determination of the Bi fraction, $y$, for various GaAsBi:(Si) films. .......................................... 160

Table C.3 Droplet compositions of surface droplets on GaAsBi:Si films of various Bi fractions, $y$, as determined by X-ray spectroscopy (EDX) and/or Auger electron spectroscopy (AES). .......................................... 161

Table C.4 Droplet surface coverage for GaAsBi:Si films of various Bi fractions, $y$. .......................................... 162

Table C.5 Room-temperature dopant type, resistivity, $\rho$, free carrier concentration, $n$, and mobility, $\mu$, for GaAsBi:Si films of various Bi fractions, $y$. .................... 163

Table C.6 Photoluminescence data, including the peak position and full-width-at-half maximum (FWHM), for GaAsBi:Si films of various Bi fractions, $y$, grown using either $As_2$ or $As_4$. .......................................... 164

Table C.7 Activation energy, $E_a$, and electron-capture barrier, $E_c$, for GaAsN:Si films of various N fractions, $x$. .......................................... 165

Table C.8 Persistent photoconductivity magnitude (the increase in conductivity following the termination of illumination, normalized to the preillumination conductivity), for GaAsN:Si films of various N fractions, $x$. .............................. 166

## List of Appendices

Appendix A Growth Parameters for GaAsBi Films ............ 144

Appendix B Data Analysis ............ 147

Appendix C Tabulated Data ............ 158

Appendix D Hall Bar Photolithography Process ............ 167

Appendix E Contact Error in Van der Pauw Measurements ............ 168

## Abstract

**Growth and Electronic Properties of GaAsN and GaAsBi Alloys**

**by**

**Richard L. Field III**

**Chairs: Rachel S. Goldman and Cagliyan Kurdak**

Dilute nitride and dilute bismuthide semiconductor alloys are of significant interest since their bandgap energies can be tuned dramatically without a substantial change in lattice parameter, making them promising for a wide variety of optoelectronic applications.

We examine the role of N environment on persistent photoconductivity (PPC) in GaAsN films. For N fractions >0.006, significant PPC is observed at cryogenic temperatures, with the PPC magnitude increasing with increasing N fraction due to an increase in the density of N-induced levels. Interestingly, rapid-thermal annealing suppresses the PPC magnitude and reduces the N interstitial fraction; thus, the N-induced level is likely associated with N interstitials. PPC is attributed to the photogeneration of carriers from N-induced levels to the conduction-band edge, leading to a modified N molecular bond configuration. With the addition of thermal energy, the ground state configuration is restored; the N-induced level is then able to accept carriers and the conductivity decays to its preillumination value. Furthermore, we have used PPC to drive a metal-insulator transition in GaAsN, allowing us to extract the electron effective mass using the Mott criterion. Reports indicate

that the effective mass of GaAsN is dopant-dependent. We find that the effective mass for Si-doped GaAsN is consistent with predictions considering N clustering.

For molecular-beam epitaxy of GaAsBi, we show that Bi incorporation into GaAs is favorable over a wider range of growth conditions with $As_4$ in comparison with $As_2$, facilitating growth of smooth, droplet-free GaAsBi films. The preference for Bi incorporation with $As_4$ is associated with the differences in the likelihood for $As_2$ vs. $As_4$ to replace weakly bonded surface $Bi_2$. Then, we consider the role of the transition from Group-V-rich to Group-III-rich conditions (the stoichiometry threshold) on the negative or positive type conductivity induced by silicon incorporation. For As-rich GaAsBi growth, Si incorporation leads to *n*-type conductivity. For Ga-rich GaAsBi growth, GaAsBi:Si films are *p*-type, and free carrier concentrations in excess of $5x10^{18}$ $cm^{-3}$ are achieved for Bi fractions ~0.05, making Si a promising acceptor dopant. We propose a dopant incorporation mechanism based upon the growth-rate dependence of the stoichiometry threshold for GaAsBi.

# Chapter 1

# Introduction

## 1.1 Overview

Dilute nitride and dilute bismuthide semiconductor alloys are of significant interest due to the fact that their bandgap energy can be tuned dramatically without a substantial change in lattice parameter. For example, the bandgap of GaAs is reduced by approximately 150 meV or 90 meV for 1% N or 1% Bi incorporated into GaAs, respectively.[1,2] Thus, both GaAsN and GaAsBi retain near-lattice matching to common substrates, such as GaAs and InP, for a variety of bandgaps in the near-infrared regime. Therefore, GaAsN and GaAsBi alloys and heterostructures are promising for a wide variety of optoelectronic applications, such as long-wavelength light emitters[3-5] and detectors,[6-8] high-performance heterojunction bipolar transistors,[9-14] and high-efficiency photovoltaic devices.[15,16] While dilute nitrides have received considerable attention, dilute bismuthides are relatively new alloys that have emerged over the past few years.

In many respects, dilute nitrides and dilute bismuthides are analogous and complimentary semiconductor alloys. Both N and Bi are group V elements and are isoelectronic with As. However, N has a smaller bond radius than As while that of Bi is larger;[17] therefore, N and Bi introduce opposite strain into GaAs. Furthermore, both N and Bi form resonant states with GaAs. Specifically, N-induced levels create a perturbation to the conduction band

of GaAs,[18,19] while Bi-induced levels introduce a perturbation to the valence band.[20] Finally, for either alloy, N or Bi incorporation is associated with a bandgap reduction. These properties make the quaternary GaAsNBi unique in that the conduction and valence band offsets can be controlled independently over a variety of bandgaps, with the ability to maintain exact lattice matching to GaAs. Indeed, an understanding of the properties of both GaAsN and GaAsBi is fundamental for design and implementation of GaAsNBi alloys.

In this chapter, we examine the current experimental and theoretical understandings of GaAsN and GaAsBi alloys. First, we present methods of synthesizing GaAsN and GaAsBi alloys using molecular-beam epitaxy. Then, we discuss the anomalous bandgap bowing, and present the current theoretical understanding of the electronic structure of GaAsN and GaAsBi alloys. Finally, a review of device applications is presented.

## 1.2 Synthesis of GaAsN and GaAsBi alloys

### 1.2.1 Synthesis of GaAsN alloys

GaAsN alloys have been synthesized using several techniques, including ion implantation,[21,22] RF sputtering,[23-25] metal-organic chemical vapor deposition (MOCVD),[26] metal-organic molecular-beam epitaxy (MOMBE),[27] and solid-state molecular-beam epitaxy (MBE).[28-32] However, GaAsN films synthesized using ion implantation and RF sputtering are typically amorphous.[21-25] Furthermore, MOCVD and MOMBE often introduce higher levels of carbon and hydrogen contamination than MBE, due to the use of metal-organic precursors for Ga and/or As.[33] Typically, (In)GaAsN films have been grown using MOCVD due to its lower cost compared to MBE;[9,34] however, the highest performing lasers have been reported for films grown using MBE.[35-38]

During MBE of GaAsN alloys, it has been shown that both N incorporation and surface roughness are influenced by growth temperature, growth rate, and active As species.[39] In Fig. 1.1, we present surface reconstruction diagrams of GaAsN films, where growth rate is plotted vs. substrate temperatures, for fixed $As_2$/Ga and $As_4$/Ga beam-equivalent pressure (BEP) ratios.[39] For growth of high-quality GaAsN films, growth conditions must avoid a “forbidden window” (shaded in Fig. 1.1), which leads to increased surface roughness. The forbidden window is narrower for growth using $As_2$, allowing for growth of GaAsN films at higher growth temperatures. Furthermore, growth of GaAsN films with a (2 x 1) surface reconstruction leads to increased substitutional incorporation of N. This is presumably due to the higher number of group V sites per unit area available on the (2 x 1) reconstructed surface, in comparison with the (1 x 3) and (2 x 4) reconstructed surfaces.[40] Indeed, growth conditions must be carefully controlled to achieve high-quality GaAsN films.

### 1.2.2 The influence of stoichiometry imbalance on GaAsBi growth

For many highly-mismatched alloys, epitaxy occurs in the vicinity of the transition from anion-rich to cation-rich conditions (the stoichiometry threshold).[41-45] For example, epitaxy of CdTeO occurs only with precise control of the Cd to Te flux ratio.[41,42] Furthermore, deviations from the stoichiometry threshold during epitaxy can strongly influence the morphology and electronic properties of semiconductor alloys. For example, epitaxy of GaAsBi and InSbBi films near stoichiometry is necessary to prevent the formation of surface droplets with diameters ranging from 100's of nm to a few μm,[46-49] which enhance light scattering, resulting in reduced photoluminescence emission.[50-52] Similarly, for $Bi_2Se_3$ and $Bi_2Te_3$ films, stringent stoichiometry control is required for the Fermi energy to be located within the bandgap, thereby enabling surface states to dominate transport properties, as required for topological insulators.[45] It has been suggested that dopant incorporation during epitaxy is also sensitive to stoichiometry. For example, epitaxy of CdTe:As and GaAs:Si in cation-rich (anion-rich) conditions leads to *p*-type (*n*-type) conductivity.[53-55] Indeed, it has been shown that Si acts as an acceptor in GaAs prepared under Ga-stable conditions, often leading to the incorporation of excess arsenic and a reduced lattice parameter for $Ga_{1-\delta}As_{1+\delta}$.[55] For both GaAs and GaAsBi, we recently showed that the threshold for Ga-stable growth conditions, i.e. the stoichiometry threshold, is influenced by the growth rate.[46] To date, the influence of the stoichiometry threshold on the interplay between Bi incorporation, Si doping type, and any excess As incorporation, remain unknown.

### 1.2.3 Synthesis of GaAsNBi alloys

To date, few groups have grown GaAsNBi films, all using MBE with substrate temperatures in the range 350 – 400 °C, using either $As_2$ or $As_4$.[56-58] In this temperature range, a balance is found between growth of GaAsN films in the range 400 – 425 °C (to avoid the forbidden window, as described in Sec. 1.2.1), and increased Bi incorporation around 280 °C.[59] Reports indicate that most Bi atoms are located at substitutional sites, while 71 ± 6% of N are incorporated substitutionally,[58] similar to reports of N incorporation in GaAsN.[60] For GaAsNBi, a bandgap reduction of 130 meV or 62 meV for 1% N or 1% Bi incorporated has been reported.[56] Furthermore, strain-balanced $Ga(As_{0.33}Bi_{0.67})_wAs_{1-w}$ films, with a room-*T* photoluminescence peak down to 0.96 eV, have been reported.[56]

## 1.3 Properties of GaAsN and GaAsBi alloys

### 1.3.1 Bandgap bowing

In the simplest approximation for the dependence of bandgap energy, $E_g$, on alloy composition, a linear interpolation of binary endpoints is used (i.e. Vegard's Law).[61] In Fig. 1.2, points represent values of $E_g$ vs. bond length for various III-V compound and elemental semiconductor systems,[1,62-67] with the connecting lines representing values of $E_g$ and bond length for various alloys. Due to differences in the electronic structures of the binary compounds, deviations from the rule of mixtures are often observed. Thus, the bandgap values are often approximated with quadratic deviations from Vegard's Law. For pseudobinary alloys $GaAs_{1-x}N_x$ and $GaAs_{1-y}Bi_y$, the quadratic deviations can be expressed as

$$(E_g)_{\mathrm{GaAsN}}(x) = x\,(E_g)_{\mathrm{GaN}} + (1\text{-}x)\,(E_g)_{\mathrm{GaAs}} - x\,(1\text{-}x)\,b_{\mathrm{GaAsN}} \quad (1.1)$$

and

$$(E_g)_{GaAsBi}(y) = y\,(E_g)_{\mathrm{GaBi}} + (1\text{-}y)\,(E_g)_{\mathrm{GaAs}} - y\,(1\text{-}y)\,b_{\mathrm{GaAsBi}}\,, \quad (1.2)$$

where $x$ and $y$ are the N fraction and Bi fraction substituting for As, respectively. For most III-V alloys, the bowing parameter, $b$, is typically a fraction of an eV.[63] In contrast, GaAsN ($b_{\mathrm{GaAsN}} \approx$ 16-26 eV)[68] and GaAsBi alloys ($b_{\mathrm{GaAsBi}} \approx$ 2 eV)[69,70] exhibit a large bandgap bowing, such that there is a significant decrease in bandgap energy with only a small change in bond length. Furthermore, since N has a smaller bond length than As, the lattice parameter of GaAsN decreases with increasing N fraction, introducing tensile strain at the interface. In the case of GaAsBi, it is predicted that GaBi has a longer bond length than GaAs;[69] thus, GaAsBi is expected to introduce compressive strain at the interface. The opposite strain effects of GaAsN and GaAsBi makes the quaternary GaAsNBi promising because it can be latticed matched to GaAs for a variety of bandgap energies, as shown by the vertical line in Fig. 1.2. Indeed, GaAsNBi is predicted to be strain balanced using the relationship [Bi] ≈ 1.7[N],[71] and has been demonstrated experimentally, as described in Sec. 1.2.3.

### 1.3.2 Electronic structure

Conventional semiconductor alloys are formed by isovalent atomic substitution, creating a perturbation to the band structure of the host compound. Typically, the isovalent impurity creates an energetically shallow state, close to either the conduction or valence band edge, which negligibly influences the host band structure.[72] However, for highly mismatched alloys, the electronegativity of the isovalent impurity is significantly higher or lower than that of the host compound, causing the impurity to alter the carrier charge distribution. This

creates localized levels associated with the impurity and causes a perturbation to the host band structure. Impurities attracted to electrons and holes are referred to as pseudoacceptors and pseudodonors, respectively. The electronegativity and electron configuration for elements isovalent with As are listed in Table 1.1.[73] Since N has the largest electronegativity among Group V elements, pseudoacceptor N produces the strongest conduction band perturbation among III-V alloys. Indeed, N incorporation into GaAs and GaP is heavily studied among III-V isovalent impurities.[60,74] However, much less attention has been given to pseudodonor isovalent impurities. As shown in Table 1.1, Bi has the lowest electronegativity among Group V elements; therefore, Bi is expected to create the strongest valence band perturbation among pseudodonors isovalent to III-V alloys.

For pseudoacceptor isovalent impurities, the perturbation to the conduction band is often described by the band anti-crossing (BAC) model.[18,19] For GaAsN, N incorporation creates a N-induced level which interacts with the extended states of the host GaAs matrix, as shown in Fig. 1.3. According to the BAC model, band anti-crossing splits the conduction band into two sub-bands, referred to as $E_+$ and $E_-$. As N incorporation increases, the band splitting becomes more significant, driving $E_-$ down in energy and subsequently reducing the bandgap energy of the alloy.

Similarly, the valence band anti-crossing (VBAC) model is used to describe the interaction of pseudodonor isovalent impurity states with the valence band.[75] According to the VBAC model, the heavy-hole (HH), light-hole (LH), and spin-orbit (SO) sub-bands of the valence band are split into two groups, $E_+$ ($HH^+$, $LH^+$, $SO^+$) and $E_-$ ($HH^-$, $LH^-$, $SO^-$), as shown in Fig. 1.4. This causes both (a) an upward movement of the valence band edge, which decreases the bandgap energy, and (b) a splitting of the SO sub-band by energy $\Delta_{SO}$. Since the Bi 6*p* orbital interacts with the valence band minimum of GaAs,[76] GaAsBi alloys

are expected to follow the VBAC model. Interestingly, for $GaAs_{1-y}Bi_y$, there is a crossover of $E_g$ and $\Delta_{SO}$, as is shown in Fig. 1.5, such that $\Delta_{SO} > E_g$ at approximately $y = 0.105$.[77]

The BAC and VBAC models have successfully predicted several important properties of GaAsN and GaAsBi alloys, such as the reduction in bandgap energy with increasing N or Bi fraction, the nonlinear pressure dependence of the bandgap energy for GaAsN, and the SO splitting for GaAsBi.[18,19,75] However, the BAC and VBAC models only consider a single local atomic environment, and subsequently do not predict extraordinary physical phenomena. For example, the BAC model predicts a N-composition-dependent flattening of the $E_-$ band, and thus, fails to predict the observed non-monotonic increase of the GaAsN electron effective mass with increasing N fraction.[78-82] In addition, the BAC model does not predict persistent photoconductivity (PPC) in GaAsN, in which an illumination-induced increase in conductivity persists following the termination of illumination,[83-85] with relaxation timescales up to hours or days.[60] The limitations of the BAC model demonstrate the necessity to consider the influence of pair formation and clustering. For GaAsN, this is important outside the ultradilute [N] regime, as increasing [N] leads to the formation of N pairs and clusters, resulting eventually in the formation of an impurity band.[86-92] The linear combination of isolated N resonant states (LCINS) model includes hybridization between the conduction band edge and N cluster states,[82] as shown in Fig. 1.6, leading to a modified band diagram.[93] The LCINS model predicts a non-monotonic increase of the effective mass, which was recently observed by Dannecker *et al.*[81,94-96] Indeed, the concentration and local atomic environment of solute atoms determine the properties of semiconductor alloys.

### 1.3.3 Mobility

It is predicted that N-induced levels will influence the electronic properties of GaAsN alloys, due to electron scattering from levels resonant with the conduction band edge.[18,19] In Fig. 1.7, we plot the reduction in electron mobility, $\mu_e$, as a function of $x$, for various experimental and theoretical studies. The BAC model only considers isolated substitutional N and predicts a decrease in $\mu_e$ with increasing $x$.[97] The LCINS model includes contributions from randomly forming N clusters, in addition to isolated substitutional N, and therefore predicts a more substantial decrease in $\mu_e$ with increasing $x$ than is predicted by the BAC model.[88] However, experimental reports indicate that the $x$-dependence of $\mu_e$ is lower than predicted by either the BAC or LCINS models, implying that additional scattering sources may need to be taken into account, such as scattering from $(N\text{-}N)_{As}$ or $(N\text{-}As)_{As}$ split interstitials.

In the case of GaAsBi alloys, Bi incorporation introduces a Bi-induced level that is resonant with the valence band;[2] therefore, it is expected that the hole mobility, $\mu_h$, will decrease with increasing $y$, whereas $\mu_e$ should remain essentially unchanged. Because Bi has a larger bond radius than As, it is expected that Bi will incorporate substitutionally or as clusters, but not interstitially. Indeed, reports indicate that Bi preferentially replaces As, with formation of few $Bi_{Ga}$ heterosites.[98] Therefore, we expect fewer Bi-induced states to be introduced to GaAsBi than there are N-induced states introduced to GaAsN. Subsequently, the reduction in $\mu_h$ of GaAsBi, due to Bi incorporation, should be less than the reduction in $\mu_e$ of GaAsN due to N incorporation.[99]

### 1.3.4 Optical and thermoelectric properties

As discussed in Sec. 1.3.1, both N and Bi incorporation into GaAs leads to a reduction in $E_g$. Accordingly, there is a shift in the photoluminescence (PL) emission peak to lower energy with increasing N or Bi incorporation.[1,2] Furthermore, for both GaAsN and GaAsBi alloys, an *S*-shaped behavior for the *T*-dependence of the PL emission peak is observed and often attributed to carrier localization.[100,101] Indeed, N-induced levels (Bi-induced levels) may lead to carrier localization in GaAsN (GaAsBi) alloys.[18-20] Subsequently, the *T*-dependence of the PL emission peak does not follow the Varshni equation

$$E_g(T) = E_g(0) - \frac{\alpha T^2}{T + \beta} \ , \qquad (1.3)$$

where $\alpha$ and $\beta$ are material constants. Thus, the bandgap energy cannot be determined using the Varshni equation for alloys exhibiting *S*-shaped behavior.

We now consider the influence of N incorporation on the *T*-dependence of the Seebeck coefficient, *S*, for GaAsN alloys, as shown in Fig. 1.8.[94] The Seebeck coefficient is a measure of the induced thermoelectric voltage in response to a *T*-gradient. As shown in Fig. 1.8, N incorporation significantly enhances $|S|$ in the $T < 140$ K regime, which is attributed to increased electron-phonon coupling, often termed phonon drag. For the $T > 140$ K regime, *S* decreases monotonically with increasing *T*, due to electron diffusion driven by the *T*-gradient.

## 1.4 Device applications

### 1.4.1 Photovoltaic devices

For photovoltaic devices (PV), the band structure influences photon absorption and processes which limit conversion efficiencies. Photons with energy $h\upsilon < E_g$ are transmitted through a film; thus, the material is transparent at these energies. Photons with energy $h\upsilon \geq E_g$ are absorbed, but any energy above $E_g$ is lost due to thermalization as a phonon is either absorbed or emitted. Since the solar spectrum covers a broad range of energies, a single-junction PV device can only capture a small fraction of the available energy. Additional energy losses, such as losses from recombination of electron-hole pairs, further degrade efficiency. Currently, the highest efficiency for a single-junction PV device is 29.1% from a GaAs cell.[102]

In multi-junction PV devices, each cell preferentially absorbs different regions of the solar spectrum, thereby reducing the total thermalization loss and increasing the efficiency of the PV device. The various layers must be near-lattice matched in order to synthesize the multi-junction device. The optimal heterostructure is predicted to have bandgap energies of sequence 1.9 eV, 1.42 eV, 1.05 eV, and 0.67 eV.[103] For the first, second, and fourth cells, GaInP, GaAs, and Ge are sufficiently lattice matched and have the required bandgaps. However, until recently no material has existed with a bandgap near 1.05 eV that is latticed matched to GaAs. The discovery of the large bandgap bowing of GaAsN eventually led to the achievement of InGaAsN nearly lattice-matched to GaAs, which has been introduced as the 1.05-eV cell.[104] However, InGaAsN has a low electron mobility and experiences losses due to Auger recombination, as well as defect-related scattering and recombination.[105,106]

### 1.4.2 Light emitters

Since optical fibers are transparent at the 1.3-μm and 1.55-μm wavelengths (0.95 and 0.8 eV), it is beneficial to engineer lasers and light-emitting diodes to emit at these wavelengths. The subsequent reduction in glass fiber dispersion promotes the development of reliable, high bit-rates and longer transmission distances. At 1.5 μm, attention has been given to InGaAsP/InP lasers;[74] however, these devices suffer from losses due to Auger recombination and inter-valence band absorption.[107] Furthermore, 1.3 μm InAs/GaAs and 1.5 μm InAs/InP quantum-dot lasers similarly experience losses due to Auger recombination,[108,109] while also having strong temperature sensitivity unless doped *p*-type.[110] (In)GaAsN/GaAs lasers experience weaker temperature sensitivity, but experience losses due to Auger recombination as well as defect-related scattering and recombination.[111]

### 1.4.3 Advantages of GaAsN and GaAsBi

Alloys of GaAsN and GaAsBi are promising for PV and light-emitting applications because their bandgap energies can be tailored to <1 eV, while maintaining near-lattice matching to GaAs. However, unlike GaAsN, for GaAsBi alloys there is a crossover of $E_g$ and $\Delta_{SO}$, such that $\Delta_{SO} > E_g$ for $y > 0.105$.[77] In this regime, Auger recombination of holes from the SO band is forbidden by conservation of energy, as the energy from electron-hole recombination is less than the energy required to excite a hole from near the valence band maximum to the SO band.[112] The suppression of Auger recombination is highly beneficial for multijunction PV devices and the design of high-efficiency lasers operating at telecommunication wavelengths, making GaAsBi and GaAsNBi alloys particularly promising.

Additionally, GaAsN/GaAsBi superlattices have been proposed for PV applications. As shown in Fig. 1.9, alternating layers of GaAsBi and GaAsN induce a bandgap reduction due to a shift in the valence band ($\Delta E_v$) and conduction band ($\Delta E_c$) edges, respectively. GaAsN/GaAsBi superlattices can provide strain-balanced matching to GaAs substrates, due to alternating compression and tension introduced by GaAsBi and GaAsN layers, respectively. Though not realized experimentally, GaAsN/GaAsBi superlattices are expected to exhibit a Type-II band alignment.[113] The resultant absorption of sub-band photons, and the spatial separation of charge, is beneficial for intermediate-band solar cells.[76,113-115] Furthermore, it is predicted that the bandgap reduction can be controlled by varying both the alloy compositions and superlattice periods;[116] thus, GaAsN/GaAsBi superlattices may offer additional bandgap tunability compared with GaAsNBi alloys, which only offers bandgap tunability by varying the N and Bi fractions.

### 1.5 Dissertation objectives

As discussed in Section 1.3, the BAC model is often used to explain the anomalous bandgap bowing of GaAsN and GaAsBi alloys; however, the BAC model fails to predict extraordinary physical phenomena, such as PPC and the non-monotonic increase of $m_e$* with increasing $x$. Furthermore, in GaAsN, strong electron scattering hinders accurate measurements of the effective mass using traditional methods, such as cyclotron resonance. Therefore, the objective of the first part of this dissertation is to explore the origins of PPC in GaAsN, and to present a new method for extracting $m_e$* using PPC to drive the metal-insulator transition.

Due to the limited miscibility of Bi in GaAs, non-standard growth techniques are required to synthesize GaAsBi, often resulting in the formation of surface droplets. Furthermore, the influence of the stoichiometry threshold on the interplay between Bi incorporation, Si doping type, and any excess As incorporation remain unknown. Therefore, the objective of the second part of this dissertation is to consider the role of the stoichiometry threshold on the growth of GaAsBi films using $As_2$ vs. $As_4$, and also to consider the role of the stoichiometry threshold on the doping type of Si.

### 1.6 Outline of dissertation

This dissertation is organized as follows. Chapter 2 describes the experimental procedures used for this work, including molecular-beam epitaxy (MBE), reflection high-energy electron diffraction (RHEED), rapid-thermal annealing (RTA), high-resolution X-ray diffraction (HRXRD), atomic force microscopy (AFM), scanning electron microscopy (SEM), energy dispersive X-ray spectroscopy (EDX), Auger electron spectroscopy, Rutherford backscattering spectroscopy (RBS), Hall and magnetoresistance measurements, and photoluminescence (PL).

In chapter 3, we first examine the role of N environment on PPC in $GaAs_{1-x}N_x$ films. For $x > 0.006$, significant PPC is observed at cryogenic temperatures, with the PPC magnitude increasing with increasing $x$ due to an increase in the density of N-induced levels. Interestingly, rapid thermal annealing suppresses the PPC magnitude and reduces the N interstitial fraction; thus, the N-induced level is likely associated with N interstitials. PPC is attributed to the photogeneration of carriers from N-induced levels to the conduction-band edge, leading to a modified N molecular bond configuration. With the addition of thermal

energy, the ground state configuration is restored; the N-induced level is then able to accept carriers and the conductivity decays to its preillumination value. Then, we use PPC to drive a metal-insulator transition in GaAsN, and use the Mott criterion to extract the effective mass.

In chapter 4, we first consider the role of arsenic As on the growth of GaAsBi alloys. We show that growth with $As_4$ is favorable over $As_2$, facilitating growth of smooth, droplet-free GaAsBi films over a much larger window of V/III BEP ratios and growth rates. Next, we consider the role of the transition from Group-V-rich to Group-III-rich conditions (the stoichiometry threshold) on the doping type of Si, i.e. whether Si induces negative- or positive-type conductivity. For As-rich GaAsBi growth, Si incorporation leads to *n*-type conductivity. For Ga-rich GaAsBi growth, GaAsBi:Si films are *p*-type, and free carrier concentrations in excess of $5x10^{18}$ $cm^{-3}$ are achieved for Bi fractions ~0.05, making Si a promising alternative to C and Be. We propose a dopant incorporation mechanism based upon the growth-rate-dependence of the stoichiometry threshold for GaAsBi.

In chapter 5, we present a summary and offer suggestions for future work. First, we suggest using resonant electron scattering as a spectroscopic probe of N-induced levels. Second, we suggest exploring the influence of dopants on the properties of GaAsN/GaAsBi heterostructures. Next, we suggest building on our expertise in the growth of GaAsN and GaAsBi alloys, by examining their combination in alloys and heterostructures, with an eye towards engineering lattice-matched structures for optoelectronics, photovoltaics, and electronics. Then, we offer suggestions to reduce droplet surface coverage on GaAsBi films.

## 1.7 Figures

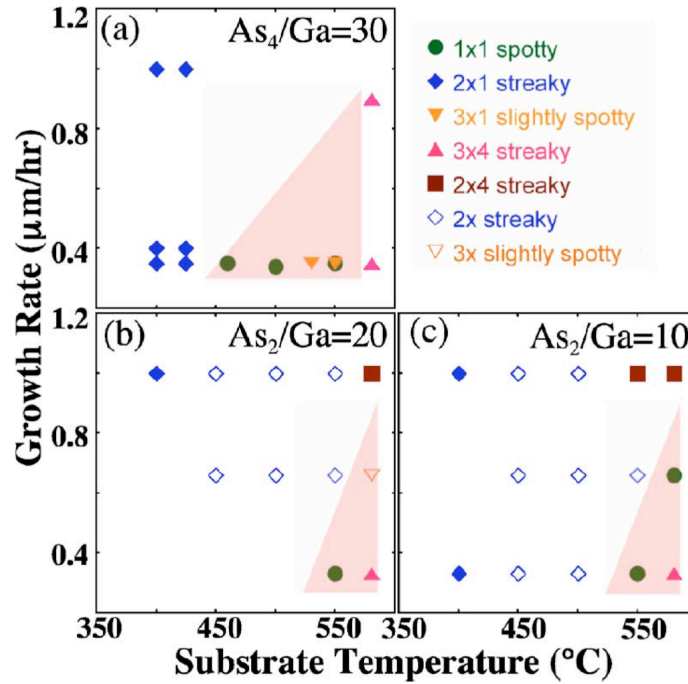


**Figure 1.1** Surface reconstructions observed during growth of GaAsN films: growth rate vs substrate temperature for (a) $As_4$/Ga BEP ratio ~30; (b) $As_2$/Ga BEP ratio ~20; and (c) $As_2$ /Ga BEP ratio ~10. Solid (open) symbols denote 500 nm (10–100 nm) thick GaAsN films. The shaded regions indicate the conditions which lead to significant surface roughness, referred to as the "forbidden window." Reprinted with permission from Ref. 39 (Copyright 2007, AIP Publishing LLC).

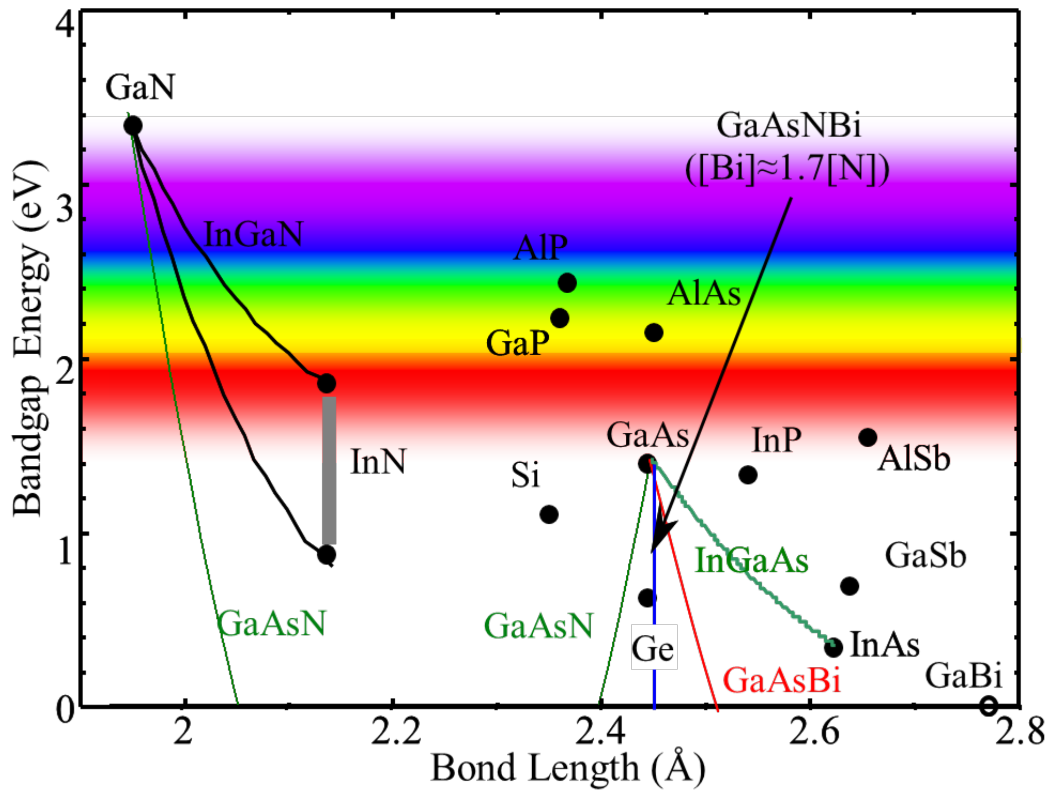


**Figure 1.2** Bandgap energy vs. bond length for various III-V compound and elemental semiconductors. The points correspond to the bandgap energy and bond length for each elemental and binary semiconductor, and connecting lines correspond to alloys. The quaternary GaAsNBi can maintain lattice matching to GaAs using a relationship [Bi] ≈ 1.7[N], over a variety of bandgap energies. Adapted and printed with permission from Ref. 117 (Copyright 2010, Yu Jin).

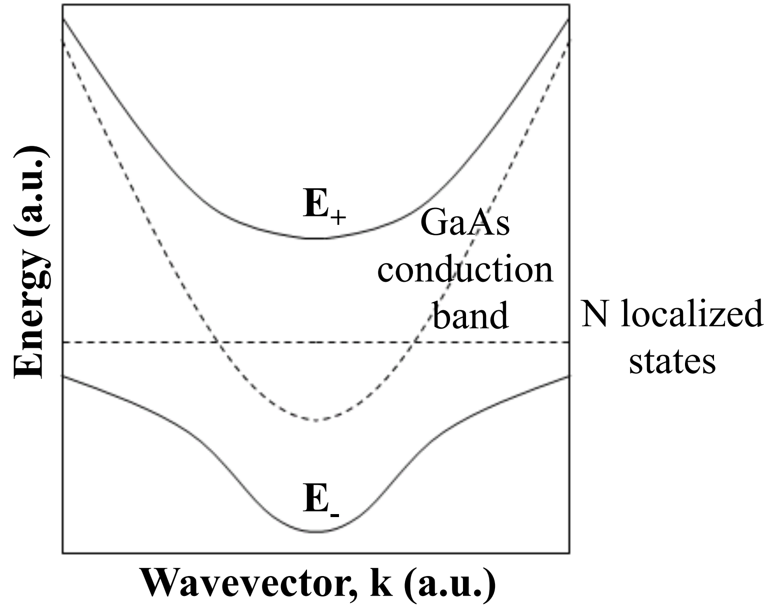


**Figure 1.3** Schematic of dispersion relationships for sub-bands (solid lines) of GaAsN using the band anti-crossing model. The dotted lines represent the unperturbed energies of the N-induced localized states and the GaAs conduction band; the solid lines represent the hybridized $E_+$ and $E_-$ sub-bands. Reprinted with permission from Ref. 117 (Copyright 2010, Yu Jin).

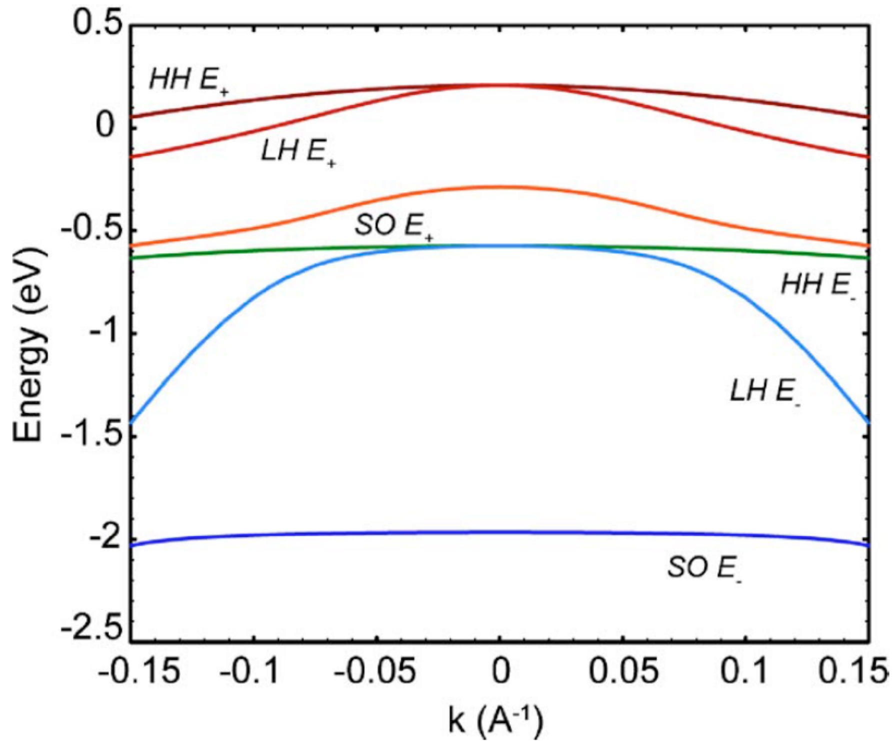


**Figure 1.4** Calculated dispersion relationships for sub-bands of GaAsBi using the valence band anti-crossing model. A Bi-induced localized state resonant with the valence band splits the heavy-hole (HH), light-hole (LH), and spin-orbit (SO) sub-bands of the valence band into two groups, $E_+$ ($HH^+$, $LH^+$, $SO^+$) and $E_-$ ($HH^-$, $LH^-$, $SO^-$). Reprinted with permission from Ref. 75 (Copyright 2007, AIP Publishing LLC).

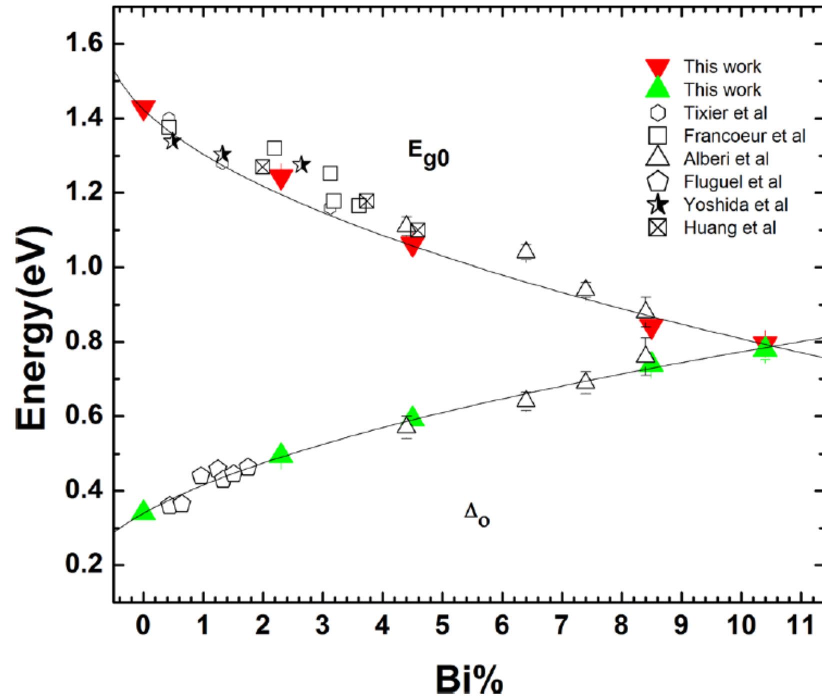


**Figure 1.5** Reduction of bandgap energy, $E_g$, and splitting of the spin-orbit sub-band, $\Delta_{SO}$, as a function of percent Bi fraction for GaAsBi alloys, as reported by Batool.[77] There is a crossover such that $\Delta_{SO} > E_g$ at a Bi fraction of 0.105. Reprinted with permission from Ref. 77 (Copyright 2012, AIP Publishing LLC).

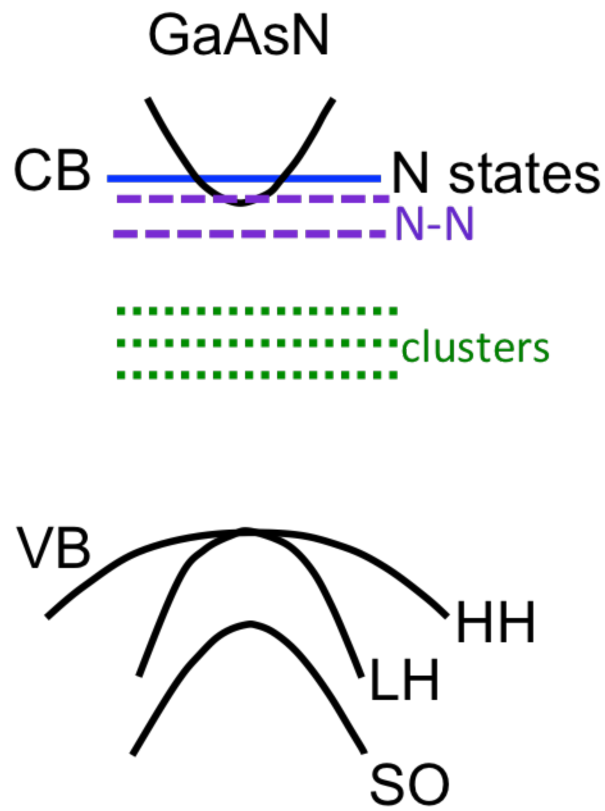


**Figure 1.6** GaAsN band structure, and N cluster states, considered by the linear combination of isolated N resonant states (LCINS) model.

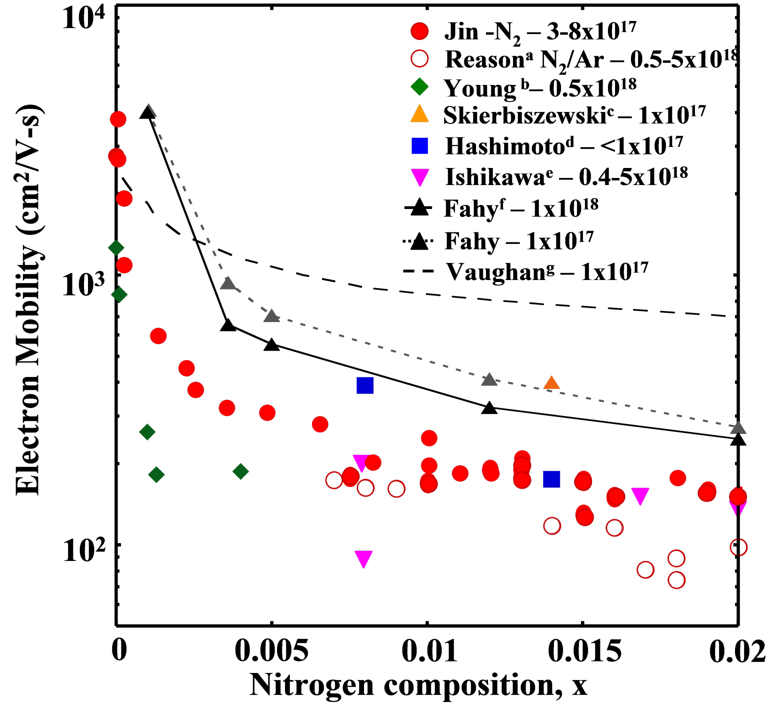


**Figure 1.7** Electron mobility, $\mu_e$, vs. N composition, $x$, for bulk $GaAs_{1-x}N_x$ films of various targeted free carrier concentrations, in units of $cm^{-3}$. The calculated $\mu_e$ by Fahy and Vaughan are included for comparison to experimental values. The measured $\mu_e$ decreases substantially with increasing $x$, and is lower than the prediction of all the theories. [a]see Ref. 39. [b]see Ref. 96. [c]see Ref. 118. [d]see Ref. 119. [e]see Ref. 120. [f]see Ref. 88. [g]see Ref. 97.

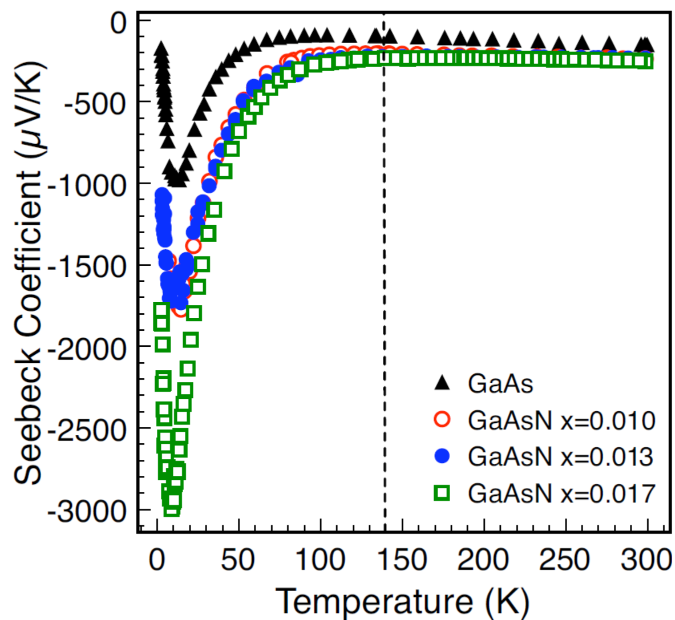


**Figure 1.8** Seebeck coefficient, $S$, as a function of temperature for various GaAsN alloys. N incorporation significantly enhances $|S|$ in the $T < 140$ K regime, due to increased electron-phonon coupling, often termed phonon drag. For the $T > 140$ K regime, $S$ decreases monotonically with $T$, due to electron diffusion driven by the $T$ gradient. Reprinted with permission from Ref. 94 (Copyright 2010, American Physical Society).

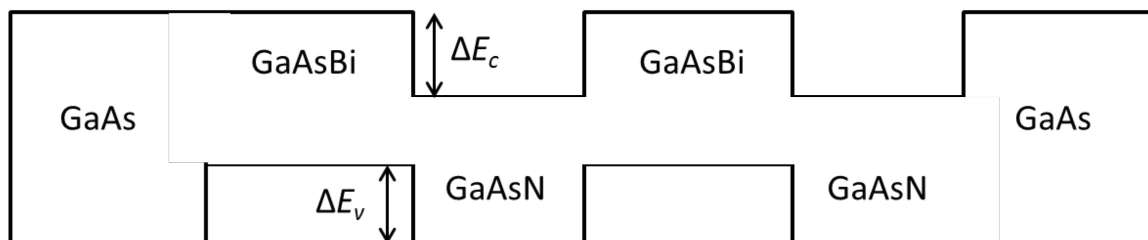


**Figure 1.9** A schematic of a GaAsN/GaAsBi superlattice. GaAsBi and GaAsN induce a bandgap reduction due to a shift in the valence band ($\Delta E_c$) and conduction band ($\Delta E_c$), respectively.

## 1.8 Tables

**Table 1.1:** Properties of Group V elements, including the electronic configuration, atomic mass, covalent radius, and Pauling's electronegativity.[73]

| Element | Electron Configuration | Atomic Mass | Covalent Radius (nm) | Electronegativity |
|---|---|---|---|---|
| N | (He) $2s^2 2p^3$ | 14.007 | 0.07 | 3.04 |
| P | (Ne) $3s^2 3p^3$ | 30.97 | 0.106 | 2.19 |
| As | (Ar) $3d^{10} 4s^2 4p^3$ | 74.92 | 0.118 | 2.18 |
| Sb | (Ke) $4d^{10} 5s^2 5p^3$ | 121.75 | 0.136 | 2.05 |
| Bi | (Xe) $4f^{14} 5d^{10} 6s^2 6p^3$ | 208.98 | 0.145 | 2.02 |

### 1.9 References

[1] W.G. Bi and C.W. Tu, Appl. Phys. Lett. 70, 1608 (1997).

[2] S. Francoeur, M.-J. Seong, A. Mascarenhas, S. Tixier, M. Adamcyk, and T. Tiedje, Appl. Phys. Lett. 82, 3874 (2003).

[3] J.S. Harris, Semicond. Sci. Technol. 17, 880 (2002).

[4] L.H. Li, V. Sallet, G. Patriarche, L. Largeau, S. Bouchoule, K. Merghem, L. Travers, and J.C. Harmand, Electron. Lett. 39, 519 (2003).

[5] H. Reichert, A. Ramakrishnan, and G. Steinle, Semicond. Sci. Technol. 17, 892 (2002).

[6] M.R. Gokhale, J. Wei, H. Wang, and S.R. Forrest, Appl. Phys. Lett. 74, 1287 (1999).

[7] B. Sciana, I. Zborowska-Lindert, D. Pucicki, B. Boratynski, D. Radziewicz, M. Tlaczala, J. Serafinczuk, P. Poloczek, G. Sek, and J. Misiewicz, Opto-Electronics Review 16, 1 (2008).

[8] J.-Y. Duboz, M. Hugues, B. Damilano, A. Nedelcu, P. Bois, N. Kheirodin, and F.H. Julien, Appl. Phys. Lett. 94, 022103 (2009).

[9] P.C. Chang, N.Y. Li, A.G. Baca, H.Q. Hou, C. Monier, J.R. Laroche, F. Ren, and S.J. Pearton, IEEE Electron Dev. Lett. 22, 113 (2001).

[10] C. Monier, A.G. Baca, P.C. Chang, N.Y. Li, H.Q. Hou, F. Ren, and S.J. Pearton, Electron. Lett. 37, 198 (2001).

[11] P.M. Asbeck, R.J. Welty, C.W. Tu, H.P. Xin, and R.E. Welser, Semicond. Sci. Techno. 17, 898 (2002).

[12] K.L. Lew, S.F. Yoon, H. Wang, W. Wicaksono, J.A. Gupta, S.P. McAlister, J. Vac. Sci. Technol. B 24, 1308 (2006).

[13] I. Hase, Heterojunction bipolar transistor with a base layer that contains bismuth, US Patent #7,009,225 (2006).

[14] Z.D. Marks, I.W. Haygood, and B. VanZeghbroeck, IEEE Trans. Electron Dev. 60, 200 (2012).

[15] J.F. Geisz and D.J. Friedman, Semicond. Sci. Technol. 17, 769 (2002).

[16] D.B. Jackrel, S.R. Bank, H.B. Yuen, M.A. Wistey, J.S. Harris, A.J. Ptak, S.W. Johnston, D.J. Friedman, and S.R. Kurtz, J. Appl. Phys. 101, 114916 (2007).

[17] J.J. Gersten and F.W. Smith, The physics and chemistry of materials (Wiley Interscience, New York, USA, 2001).

[18] W. Shan, W. Walukiewicz, J.W. Ager, E.E. Haller, J.F. Geisz, D.J. Friedman, J.M. Olson, and S.R. Kurtz, Phys. Rev. Lett. 82, 1221 (1991).

[19] W. Shan, W. Walukiewicz, J.W. Ager, E.E. Haller, J.F. Geisz, D.J. Friedman, J.M. Olson, and S.R. Kurtz, J. Appl. Phys. 86, 2349 (1999).

[20] K. Alberi, O.D. Dubon, W. Walukiewicz, K.M. Yu, K. Bertulis, and A. Krotkus, Appl. Phys. Lett. 91, 051909 (2007).

[21] X. Weng, W. Ye, S.J. Clarke, R.S. Goldman, V. Rotberg, A. Daniel, and R. Clarke, J. Appl. Phys. 97, 064301 (2005).

[22] X. Weng, R.S. Goldman, V. Rotberg, N. Bataiev and L.J. Brillson, Appl. Phys. Lett. 85, 2774 (2004).

[23] A.R. Zanatta, P. Hammer and F. Alvarez, Appl. Phys. Lett. 76, 2211 (2000).

[24] D. Lollman, K. Aguir, J. Bandet, B. Roumiguieres and H. Carchano, Mat. Sci. Eng. B 43, 283 (1997).

[25] J.A. Cardona-Bedoya, A. Cruz-Orea, S.A. Tomas-Velazquez, O. Zelaya-Angel and J.G. Medoza-Alvarez, Rev. Sci. Instr. 74, 854 (2003).

[26] N. Tansu and L.J. Mawst, IEEE Photon. Lett. 14, 444 (2002).

[27] S. Francoeur, G. Sivaraman, Y. Qiu, S. Mikishin, and H. Temkin, Appl. Phys. Lett. 72, 1857 (1998).

[28] M. Kondow, K. Uomi, A. Niwa, T. Kitatani, S. Wataiki, and Y. Yazama, Jpn. J. Appl. Phys., Part 1 35, 1273 (1996).

[29] S.G. Spruytte, M.C. Larson, W. Wampler, C.W. Coldren, and Y. Yazawa, Jap. J. Appl. Phys. 35, 1273 (1996).

[30] S. Shirakata, M. Kondow, and T. Kitatani, Appl. Phys. Lett. 80, 2087 (2002).

[31] E. Tournie, M.A. Pinault, and A. Guzman, Appl. Phys. Lett. 80, 4148 (2002).

[32] L. Grenouillet, C. Bru-Chevallier, G.Guillot, P. Gilet, P. Ballet, P. Duvaut, G. Rolland, and A. Million, J. Appl. Phys. 91, 5902 (2002).

[33] A.J. Ptak, S.W. Johnston, S. Kurtz, D.J. Friedman and W.K. Metzger, J. Cryst. Growth 251, 392 (2003).

[34] S. Kurtz, A.A. Allerman, E.D. Jones, J.M. Gee, J.J. Banas and B.E. Hammons, Appl. Phys. Lett. 74, 729 (1999).

[35] D.A. Livshits, A.Y. Egorov and H. Riechert, Electron. Lett. 36, 1381 (2000).

[36] W. Li, T. Jouhti, C.S. Peng, J. Konttinen, P. Laukkanen, E.M. Pavelescu, M. Dumitrescu and M. Pessa, Appl. Phys. Lett. 79, 3386 (2001).

[37] K.D. Choquette, J.F. Klem, A.J. Fischer, O. Blum, A.A. Allerman, I.J. Fritz, S.R. Kurtz, W.G. Breiland, R. Sieg, K.M. Geib, J.W. Scott and R.L. Naone, Electron. Lett. 36, 1388 (2000).

[38] G. Steinle, H. Riechert and A.Y. Egorov, Electron. Lett. 37, 93 (2001).

[39] M. Reason, N.G. Rudawki, H.A. McKay, X. Weng, W. Ye, and R.S. Goldman, J. Appl. Phys. 101, 083520 (2007).

[40] M. Reason, H.A. McKay, W. Ye, S. Hanson, and R.S. Goldman, Appl. Phys. Lett. 85, 1692 (2004).

[41] A. Barcz, G. Karczewski, T. Wojtowicz, M. Sadlo, and J. Kossut, Appl. Phys. Lett. 72, 206 (1998).

[42] Y. Krockenberger and H. Yamamoto, Physica C 471, 185 (2011).

[43] M.C. Wagener, J.R. Botha, and A.W.R. Leitch, J. Cryst. Growth 213, 51 (2000).

[44] Y. Kajikawa, H. Kubota, S. Asahina, and N. Kanayama, J. Cryst. Growth 237-239, 1498 (2002).

[45] J. J. Lee, F. T. Schmitt, R. G. Moore, I. M. Vishik, Y. Ma, and Z. X. Shen, Appl. Phys. Lett. 101, 013118 (2012).

[46] G. Vardar, S. W. Paleg, M. V. Warren, M. Kang, S. Jeon, and R. S. Goldman, Appl. Phys. Lett. 102, 042106 (2013).

[47] K. Forghani, A. Anand, L.J. Mawst, and T. F. Kuech, J. Cryst. Growth 380, 23 (2013).

[48] V. Pacebutas, R. Butkute, B. Cechavicius, J. Kavaliauskas, and A. Krotkus, Thin Solid Films 520, 6415 (2012).

[49] M.C. Wagener, R.E. Kroon, J.R. Botha, A.W.R. Leitch, Physica B 273, 919 (1999).

[50] M. Masnadi-Shirazi, R.B. Lewis, V. Bahrami-Yekta, T. Tiedje, M. Chicoine, and P. Servati, J. Appl. Phys, 116, 223506 (2014).

[51] G. Ciatto, M. Thomasset, F. Glas, X. Lu, and T. Tiedje, Phys. Rev. B 82, 201304 (2010).

[52] M. Kang, A. A. Al-Heji, J.-E. Lee, T. W. Saucer, S. Jeon, J. H. Wu, L. Zhao, A. L. Katzenstein, D. L. Sofferman, V. Sih, and R. S. Goldman, Appl. Phys. Lett. 103, 101903 (2013).

[53] H. R. Vydyanath, Semicond. Sci. Technol. 5, S213 (1990).

[54] R. L. Harper Jr., S. Hwang, N. C. Giles, J. F. Schetzina, D. L. Dreifus, and T. H. Myers, Appl. Phys. Lett. 54, 170 (1989).

[55] S. Fukushima, T. Obata, and N. Otsuka, J. Appl. Phys. 89, 380 (2001).

[56] W. Huang, K. Oe, G. Feng, and M. Yoshimoto, J. Appl. Phys. 98, 053505 (2005).

[57] S. Tixier, S.E. Webster, E.C. Young, T. Tiedje, S. Francoeur, A. Mascarenhas, P. Wei, and F. Schiettekatte, Appl. Phys. Lett. 86, 112113 (2005).

[58] P. Wei, S. Tixier, M. Chicoine, S. francoeur, A. Mascarenhas, T. Tiedje, and F. Schiettekatte, Nucl. Instr. and Meth. in Phys. Res. B 219, 671 (2004).

[59] X. Lu, D.A. Beaton, R.B. Lewis, T. Tiedje, and M.B. Whitwick, Appl. Phys. Lett. 92, 192110 (2008).

[60] R.L. Field III, Y. Jin, H. Cheng, T. Dannecker, R.M. Jock, Y.Q. Wang, C. Kurdak, and R.S. Goldman, Phys. Rev. B 87, 155303 (2013).

[61] L. Vegard, Z. Phys. 5, 17 (1921).

[62] K. Uesungi, N. Morooka, and I. Suemune, Appl. Phys. Lett. 74, 1254 (1999).

[63] I. Vurgaftman, J.R. Meyer and L.R. Ram-Mohan, J. Appl. Phys. 89, 5815 (2001).

[64] H.J. Hovel and J.J. Cuomo, Appl. Phys. Lett. 20, 71 (1972).

[65] T.L. Tansley and C.P. Foley, J. Appl. Phys. 59, 3241 (1986).

[66] P. Specht, J.C. Ho, X. Xu, R. Armitage, E.R. Weber, R. Erni and C. Kisielowski, Solid State Commun. 135, 340 (2005).

[67] B. Monemar, P.P. Paskov and A. Kasic, Superlattices Microstruct. 38, 38 (2005).

[68] U. Tisch, E. Finkman, and J. Salzman, Appl. Phys. Lett. 81, 463 (2002).

[69] A. Janotti, S.-H. Wei, and S.B. Zhang, Phys. Rev. B 65, 115203 (2002).

[70] A. Abdiche, H. Abid, R. Riane, and A. Bouaza, Physica B 405, 2311 (2010).

[71] S.J. Sweeney and S.R. Jin, J. Appl. Phys. 113, 043110 (2013).

[72] S.H. Wei and A. Zunger, Phys. Rev. Lett. 76, 664 (1996).

[73] J.J. Gersten and F.W. Smith, *The physics and chemistry of materials* (Wiley Interscience, New York, USA, 2001).

[74] I. A. Buyanova, W. M. Chen and B. Monemar, MRS Internet J. Nitride Semicond. Res. 6, 2 (2001).

[75] K. Alberi, J. Wu, W. Walukiewicz, K. M. Yu, O.D. Dubon, S.P. Watkins, C.X. Wang, X. Lie, Y.-J. Cho, and J. Furdyna, Phys. Rev. B 75, 045203 (2007).

[76] Y. Zhang, A. Mascarenhas and L. W. Wang, Phys. Rev. B 71, 155201 (2005).

[77] Z. Batool, K. Hild, T.J.C. Hosea, X. Lu, T. Tiedje, and S.J. Sweeney, J. Appl. Phys. 111, 113108 (2012).

[78] P.N. Hai, W.M. Chen, I.A. Buyanova, H.P. Xin and C.W. Yu, Appl. Phys. Lett. 77, 1843 (2000).

[79] G.B. von Hogersthal, A. Polimeni, F. Masia, M. Bissiri, M. Capizzi, D. Gollub, M. Fischer and A. Forchel, Phys. Rev. B 67, 233304 (2003).

[80] S. Kurtz, S. Johnston and H. M. Branz, Appl. Phys. Lett. 86, 113506 (2005).

[81] F. Masia, G. Pettinari, A. Polimeni, M. Felici, A. Miriametro, M. Capizzi, A. Lindsay, S.B. Healy, E.P. O'Reilly, A. Cristofoli, G. Bais, M. Piccin, S. Rubini, F. Martelli, A. Franciosi, P.J. Klar, K. Bolz and W. Stolz, Phys. Rev. B 73 073201 (2006).

[82] E.P. O'Reilly, A. Lindsay and S. Fahy, J. Phys-Condense Mat. 16, S3257 (2004).

[83] M.G. Craford, G.E. Stillman, J.A. Rossi, and N. Holonyak, Phys. Rev. B 168, 867 (1968).

[84] D.V. Lang and R.A. Logan, Phys. Rev. Lett. 39, 635 (1977).

[85] D.V. Lang, R.A. Logan, and M. Jaros, Phys. Rev. B 19, 1015 (1979).

[86] P.R.C. Kent and A. Zunger, Phys. Rev. B 64, 115208 (2001).

[87] P.R.C. Kent and A. Zunger, Appl. Phys. Lett. 82, 559 (2003).

[88] S. Fahy, A. Lindsay, H. Ouerdane, and E.P. O'Reilly, Phys. Rev. B 74, 035203 (2006).

[89] Y. Zhang, A. Mascarenhas, H.P. Xin, and C.W. Tu, Phys. Rev. B 61, 7479 (2000).

[90] P.J. Klar, H. Gruning, W. Heimbrodt, J. Koch, F. Hohnsdorf, W. Stolz, P.M.A. Vicente, and J. Camassel, Appl. Phys. Lett. 76, 3439 (2000).

[91] R. Kudrawiec, M. Latkowska, M. Welna, J. Misiewicz, M. Shafi, R.H. Mari, M. Henini, and W. Walukiewicz, Appl. Phys. Lett. 101, 082109 (2012).

[92] K. Alberi, B. Fluegel, D.A. Beaton, A.J. Ptak, and A. Mascarenhas, Phys. Rev. B 86, 041201 (2012).

[93] A. Lindsay and E.P.O'Reilly, Phys. Rev. Lett. 93, 196402 (2004).

[94] T. Dannecker, Y. Jin, H. Cheng, C.F. Gorman, J. Buckeridge, C. Uher, S. Fahy, C. Kurdak, and R.S. Goldman, Phys. Rev. B 82, 125203 (2010).

[95] J. Ibanez, R. Cusco, E. Alarcon-Llando, L. Artus, A. Patane, D. Fowler, L. Eaves, K. and I. Suemune, J. Appl. Phys. 103, 103528 (2008).

[96] D.L. Young, J.F. Geisz and T.J. Coutts, Appl. Phys. Lett. 82, 1236 (2003).

[97] M. P. Vaughan and B. K. Ridley, Phys. Rev. B 72, 075211 (2005).

[98] M. Kunzer, W. Jost, U. Kaufmann, J.M. Hobgood, and R.N. Thomas, Phys. Rev. B 48, 4437 (1993).

[99] R. N. Kini, A. J. Ptak, B. Fluegel, R. France, R. C. Reedy, and A. Mascarenhas, Phys. Rev. B 83, 075307 (2011).

[100] I.A. Buyanova, W.M. Chen, G. Pozina, J.P. Berman, B. Monemar, H.P. Xin, and C.W. Tu, Appl. Phys. Lett. 75, 501 (1999).

[101] R. Kudrawiec, M. Syperek, P. Poloczek, J. Mislewicz, R.H. Mari, M. Shafi, M. Henini, Y. Galvao Gobato, S.V. Novikov, J. Ibanez, M. Schmidbauer, and S.I. Molina, J. Appl. Phys. 106, 023518 (2009).

[102] http://www.nrel.gov/ncpv/images/efficiency_chart.jpg; Download 11:00pm (May 8, 2015).

[103] D.J. Friedman, J.F. Geisz, S.R. Kurtz and J.M. Olson, J. Crsyt. Growth 195, 409 (1998).

[104] M. Kondow, K. Uomi, A. Niwa, T. Kitatani, S. Wataiki, and Y. Yazama, Jpn. J. Appl. Phys., Part 1 35, 1273 (1996).

[105] S.G. Spruytte, C.W. Coldren, J.S. Harris, W. Wampler, P. Krispin, K. Ploog and M.C. Larson, J. Appl. Phys. 89, 4401 (2001).

[106] W. Li, M. Pessa and J. Likonen, J. Appl. Phys. 78, 2864 (2001).

[107] S.J. Sweeney, I.P. Marko, S.R. Jin, K. Hild, Z. Batool, N. Hossain, and T.J.C. Hosea, Bismuth-Containing Compounds (Springer, New York, USA, 2013) pp. 29-33.

[108] I.P Marko, A.R. Adams, S.J. Sweeney, D.F. Mowbray, M.S. Skolnick, H.Y. Liu, and K.M. Groom, IEEE J. Sel. Top. Quant. Electron. 11, 1041 (2005).

[109] S.A. Sayid, I.P. Marko, S.F. Sweeney, P. Barrios, P.J. Poole, Appl. Phys. Lett. 97, 161104 (2010).

[110] N.F Masse, S.J. Sweeney, I.P. Marko, A.R. Adams, N. Hatoir, M. Sugawara, Appl. Phys. Lett. 89, 191118 (2006).

[111] R. Fehse, S. Jin, S.J. Sweeney, A.R. Adams, E.P. O'Reilly, H. Riechert, S. Illek, and A.U. Egorov, Electron. Lett. 37, 1518 (2001).

[112] H. Li and Z.M. Wang, Bismuth-Containing Compounds (Springer, New York, USA 2013) pp. 56-59.

[113] M. Y. Levy, C. Honsberg, A. Marti and A. Luque, IEEE Phot. Spec. Conf. 90 (2005).

[114] Y. Zhang, A. Mascarenhas and L. W. Wang, Phys. Rev. B 71, 155201 (2005).

[115] M. Y. Levy, C. Honsberg, A. Marti and A. Luque, IEEE Phot. Spec. Conf. 90 (2005).

[116] J. Hwang and J.D. Phillips, Phys. Rev. B 83, 195327 (2011).

[117] Y. Jin, Ph.D. Thesis, Ch. 1, University of Michigan, Ann Arbor, 2010.

[118] C. Skierbiszewski, P. Perlin, P. Wisniewski, W. Knap, T. Suski, W. Walukiewicz, W. Shan, K. M. Yu, J. W. Ager, E. E. Haller, J. F. Geisz and J. M. Olson, Appl. Phys. Lett. 76, 2409 (2000).

[119] A. Hashimoto, T. Yamaguchi, T. Suzuki and A. Yamamoto, J. Cryst. Growth 278, 532 (2005).

[120] F. Ishikawa, G. Mussler, K. J. Friedland, H. Kostial, K. Hagenstein, L. Daweritz and K. H. Ploog, Appl. Phys. Lett. 87, 262112 (2005).

# Chapter 2

# Experimental Procedures

## 2.1 Overview

This chapter describes the experimental procedures used to synthesize and characterize the GaAsN and GaAsBi films used in this dissertation work. All films were grown by molecular-beam epitaxy (MBE) on semi-insulating GaAs (001) substrates. During epitaxy, the surface reconstruction was monitored using reflection high-energy electron diffraction (RHEED). Following growth, the N and Bi fractions were determined using high-resolution X-ray rocking curve (HRXRC) and/or Rutherford backscattering spectroscopy (RBS) measurements. In addition, the crystalline quality of films was examined using HRXRC. For GaAsN films, the total N concentration and N interstitial fraction were determined using RBS and nuclear reaction analysis (NRA), in [001] channeling and non-channeling conditions. The optical properties of GaAsBi films were studied from photoluminescence (PL) spectra. The surface morphology was examined *ex-situ* with atomic force microscopy (AFM), and the composition profiles across surface droplets were determined using energy dispersive X-ray spectroscopy (EDX) and/or Auger electron spectroscopy (AES), in respective scanning electron microscopes (SEM). The electrical properties of films were measured using room temperature and/or variable temperature resistivity and Hall measurements, with

the carrier concentration of select films increased using persistent photoconductivity (PPC). All procedures were carried out by the author except where noted.

## 2.2 Molecular-beam epitaxy

### 2.2.1 Overview

Molecular-beam epitaxy (MBE) is an ultra-high vacuum based vapor deposition method enabling growth of high-quality epitaxial films.[1-3] Molecular beams are formed by evaporation or sublimation from heated liquids and solids, which interact chemically with a heated substrate to form epitaxial films. Since the molecules are highly reactive, epitaxial growth can occur at conditions far from equilibrium. Significantly, slow deposition rates—i.e., growth rates—allow for growth one monolayer at a time, facilitating prodigious synthesis and repeatability of cornucopious structures. The GaAsN and GaAsBi films used in this dissertation were grown in a Modified Varian GenII and/or Riber Compact 21 MBE system. All the GaAsN films were grown in the GenII MBE system; for the GaAsBi films, those grown using $As_2$ were grown in the GenII MBE system, while those grown using $As_4$ were grown in the Compact 21 MBE system.

### 2.2.2 MBE systems details

The Modified Varian Gen II MBE system consists of separately-pumped load-lock, buffer, and growth chambers, which are connected by trolleys and magnetic transfer arms, as shown schematically in Fig. 2.1. In addition, an extension chamber and LS-STM chamber allow for *in-situ* LS-STM (not shown), but was not used in this dissertation work. The growth chamber source flange houses seven solid sources (Ga, In, Al, Si, Be, Bi, and As cracker), and a radio frequency (RF) plasma source for creating active N from a $N_2$ gas source. The

growth chamber is pumped by a Varian sputter-ion pump and a CTI Cryo-Torr 8 cryopump, and the pressure in the growth chamber is monitored by an ionization gauge on the chamber wall. During growth, liquid nitrogen ($LN_2$) flows through a cryopanel to reduce the base pressure to < 3 x $10^{-10}$ Torr.

Similarly, the Compact 21 MBE system consists of separately-pumped load-lock, buffer, and growth chambers, which are connected by trolleys and magnetic transfer arms, as shown schematically in Fig. 2.2. In addition, a Riber 32 MBE system is attached (not shown), but is currently not operational and was not used in this dissertation work. The growth chamber source flange houses 10 solid sources, of which we currently use 7 (Ga, In, Al, Si, Be, Bi, and As cracker), and is pumped by a Riber ion pump and a Riber titanium sublimation pump. The pressure in the growth chamber is monitored by an ionization gauge attached to the chamber wall. During growth, $LN_2$ flows through a cryopanel to reduce the base pressure to < 3 x $10^{-10}$ Torr.

For both MBE systems, the solid source materials are contained in pyrolytic boron nitride crucibles contained in Knudsen effusion cells. The flux of each molecular beam varies exponentially with the cell temperature, which is controlled with a PID (proportional-integral-derivative) controller and is monitored by a thermocouple in contact with the crucible. The exposure to each molecular beam is then controlled by pneumatic shutters, and the flux is measured with an ionization gauge located at the growth position. For As, the flux is controlled by a needle valve for a given bulk zone temperature. Furthermore, the As cracker is able to generate either $As_4$ or $As_2$, depending on the cracking-zone temperature. The As beam-equivalent pressure (BEP) begins to saturate at cracking-zone temperatures above 1000 °C (below 600 °C), suggesting that the As species is predominantly $As_2$ ($As_4$) for cracking-zone temperatures above 1000 °C (below 600 °C).[4] Samples are held in the growth

position by the manipulator referred to as the CAR (Continuous Azimuthal Rotation); during growth, the CAR is rotated at 10 rpm to promote film uniformity. Furthermore, both growth chambers contain facilities for *in-situ* reflection high-energy electron diffraction (RHEED), and a residual gas analyzer (RGA) for *in-situ* mass spectrometry.

### 2.2.3 Substrate preparation

All films were grown on "epi-ready" GaAs substrates, delivered in a dry $N_2$ sealed container and ready for immediate introduction into the load-lock chamber. All samples were mounted on heated molybdenum blocks using indium. In the GENII MBE system, lamps bake the load-lock chamber at 150 °C for 8 hours after every chamber opening, and all samples are outgassed in the buffer chamber at 180 °C for at least 30 minutes. Following transfer into the growth chamber for both the GENII and Compact 21 MBE systems, the substrate temperature was raised to 300 °C, at which point the As shutter and needle valve were opened, providing an As overpressure to prevent GaAs decomposition. Next, the substrate temperature was increased until the diffuse RHEED pattern changed to a streaky pattern, indicating that the surface oxide had been desorbed. For GaAs, it has been reported that oxide desorption occurs in the range of 580 to 610 °C.[5,6] For growths in the GENII and Compact 21 MBE systems (including those done by the author and other Goldman group members, past and present), the oxide desorption temperature is calibrated at 580 °C and 600 °C, respectively. Therefore, this calibration was used to maintain consistency in the growth logs for each MBE system. Subsequently, the temperature was raised an additional 30 °C above the oxide desorption temperature for 10 minutes to ensure complete desorption of the surface oxide.

### 2.2.4 Temperature calibration

For both MBE systems, the sample temperature is measured by a thermocouple in contact with the back of each molybdenum block. However, the measured temperature is typically higher than the actual substrate temperature, and is dependent on the substrate size, substrate thickness, mounting method, and thermal conductivity of the molybdenum block. Subsequently, a relationship needs to be established between the measured temperature and the actual substrate temperature. Thus, for each sample, the measured temperature at oxide desorption is calibrated as 580 °C (600 °C) for the GENII (Compact 21) MBE system, as described above. This provides a linear offset between the measured and actual substrate temperatures, which is used at conventional growth temperatures. At low-growth temperatures ($T$ < 300 °C), this offset is much less significant; therefore, at low-growth temperatures, the measured temperature was used as the substrate temperature.

### 2.2.5 Reflection high-energy electron diffraction

The growth rates, incorporation ratios, and surface reconstructions of films were monitored *in-situ* using STAIB RH 30 RHEED sources, operating at 18 keV and 12 keV in the GENII and Compact 21 MBE systems, respectively. During RHEED, an electron beam is accelerated towards the sample surface at a grazing angle of ~1° and the diffracted electrons impinge upon a phosphor screen, producing diffraction patterns, which are then captured by a charge coupled device (CCD) camera. The location of the RHEED gun and phosphor screen for the GENII and Compact 21 MBE systems are shown in the schematics in Figs. 2.1 and 2.2, respectively.

The growth rate was determined by monitoring the RHEED intensity during the growth of a RHEED calibration sample. During growth, the intensity of the RHEED streaks oscillates, as shown in Fig. 2.3. Assuming that one oscillation corresponds to growth of one monolayer, the growth rate can be adjusted by varying the Ga flux, provided that the growth surface is As-terminated due to a larger flux of As. In addition, RHEED was used to monitor the surface reconstruction before, during, and after growth. We use the standard notation to report surface reconstructions, (MxN), where (xM) is the reconstruction along the [110] direction, and (xN) is the reconstruction along the $[1\bar{1}0]$ direction.

RHEED can also monitor the amount of As required to maintain surface stoichiometry. This is accomplished by measuring the V/III incorporation rate ratio, which is a measure of how long it takes a surface to recover after being deprived of an As flux. For this measurement, we typically monitor the [110] direction of the (2x4) RHEED pattern (i.e., a 2x pattern). This measurement begins with GaAs growth exhibiting a (2x4) RHEED pattern, on an As-terminated surface. Then, the As shutter is closed, resulting in a Ga-terminated surface and transition of the 2x pattern to a 4x pattern. Next, the As shutter is reopened, and the time it takes for the RHEED signal to recover to a 2x pattern is monitored. A typical incorporation rate ratio measurement is shown in Fig. 2.4, where $t_1$ is the moment when the As shutter is closed, $t_2$ is the moment when the As shutter is reopened, and $t_3$ is when As-terminated growth is recovered. The incorporation rate ratio, $\left(\frac{\mathrm{As}}{\mathrm{Ga}}\right)$, is then the total time the Ga shutter is opened until the surface recovers (starting from when the As shutter is closed), divided by the time it takes the surface to recover after the As shutter is reopened:

$$\left(\frac{\mathrm{As}}{\mathrm{Ga}}\right) = \frac{t_3 - t_1}{t_3 - t_2} = \frac{t_{\mathrm{Ga}} - t_{\mathrm{open}}}{t_{\mathrm{As}} - t_{\mathrm{open}}} \quad . \tag{2.1}$$

For GaAs and AlAs growth, streaky RHEED patterns are typically observed using $\left(\frac{\text{As}}{\text{Ga}}\right)$ between 1.3 and 1.8.[7] In this work, we targeted $\left(\frac{\text{As}}{\text{Ga}}\right)$ in the range of 1.6-1.7. If $\left(\frac{\text{As}}{\text{Ga}}\right)$ was smaller or larger, the As flux was increased or decreased, respectively, until $\left(\frac{\text{As}}{\text{Ga}}\right)$ was in the targeted range.

### 2.2.6 Molecular-beam epitaxy of GaAsN

$GaAs_{1-x}N_x$ alloy films were grown on (001) semi-insulating GaAs substrates by MBE, using solid Ga, $As_2$ or $As_4$, Si or GaTe (for *n*-type doping), and an $N_2$ RF plasma source, in the GENII MBE system. To strike the plasma, the input power was gradually increased to 400-500 Watt while keeping the reflective power lower, with a high N flow rate (e.g. ~0.5 sccm). If the plasma did not strike, the $N_2$ air line was closed for a few seconds and then reopened; the resulting overpressure of $N_2$ would often strike the plasma (sometimes it would take a few seconds after reopening the $N_2$ air line for the plasma to strike).

The sample structure for GaAsN films is shown in Fig. 2.5. The free-carrier concentrations were 5 to 13 × $10^{17}$ $cm^{-3}$, as determined by Hall measurements in GaAs control films. The N fraction, $x$, in the $GaAs_{1-x}N_x$ layers was adjusted from $x = 0.0013$ to 0.032 by varying the gas flow rate, monitored by the partial pressure of active N, using an RGA.[8,9] For all films, a 250-nm-thick GaAs buffer layer was grown at 580 °C,[10] followed by the growth of a 500-nm GaAs(N):Te or GaAs(N):Si layer in the range 400 to 425 °C.[9] Samples used for the GaAsN studies in this dissertation work were grown by Dr. Yu Jin, Dr. Hugh McKay, Dr. Jia-Hung Wu, Dr.Weifeng Ye, and the author.

### 2.2.7 Molecular-beam epitaxy of GaAsBi

Due to the large size and tendency of Bi to surface segregate, MBE of GaAsBi alloys requires non-standard growth conditions in comparison to conventional III-V alloys, including low growth temperatures. This section provides details of MBE of GaAsBi grown using $As_4$, facilitating growth of high-quality, droplet-free films, as described in Sec. 4.4. GaAsBi samples used in this dissertation work were grown primarily by the author, with the assistance of Gulin Vardar, Tim Jen, and Jordan Occena.

$GaAs_{1-y}Bi_y$:(Si) alloy films were grown on semi-insulating (001) GaAs substrates by MBE using solid Ga, $As_4$, Bi, and Si sources in the Compact 21 MBE system. The sample structure for GaAsBi films is shown in Fig. 2.6. First, a 500-nm thick GaAs buffer was grown at 600 °C at 1.2 μm/hr with a (2 x 4) RHEED pattern. Next, the substrate temperature was lowered to 280 °C, and 250- to 550-nm thick GaAs was grown with a (2 x 3) surface reconstruction. Finally, 400-nm GaAs(Bi):(Si) layers were grown at various growth rates (0.25 to 2.0 μm/hr), Group V/III BEP ratios (6 to 20), and Bi:Ga BEP ratios (0 to 0.6). All of the undoped, and the majority of the *n*-type, GaAsBi films were grown using standard GaAs growth rates (1.2. μm/hr) and V/III BEP ratios (20). In Fig. 2.7 we plot Bi fraction, $y$, (as determined by Rutherford backscattering spectroscopy) vs. Bi:Ga BEP ratio, $\kappa$, for undoped and *n*-type films. A linear interpolation of the $y$ vs. $\kappa$ data yields

$$y = 9.28\kappa - 0.175 . \tag{2.2}$$

Thus, the target Bi fraction can be estimated from the Bi/Ga BEP ratio.

### 2.3 Rapid-thermal annealing

In post-growth rapid-thermal annealing (RTA), a semiconductor is rapidly heated to a high temperature, held there for a brief time, and then cooled back to room temperature. RTA promotes migration of atoms while heated, which may activate donors and/or reduce the concentration of defects.[11] Therefore, for select GaAsN films, RTA was performed using a JetFirst-150 Rapid Thermal Processor in the Lurie Nanofabrication Laboratory (LNF) at the University of Michigan. RTA was performed in the range of 650 to 800 °C for 60 s, in 1000 sccm of $N_2$ ambient gas at atmospheric pressure. Furthermore, As out-diffusion was prevented by capping each sample with a new GaAs substrate, polished side facing the film. All RTA was performed by Dr. Yu Jin.[13]

### 2.4 High-resolution X-ray diffraction

We performed double-axis high-resolution X-ray rocking curves (HRXRC) on a BEDE $D^1$ system, as shown schematically in Fig. 2.8. For the HRXRC measurements, each sample was “rocked” about the substrate Bragg angle, while the detector remained fixed at $2\theta_B$. The in-plane and out-of-plane strain and lattice parameters were determined from an analysis of symmetric (004) and glancing-incidence (224) HRXRCs, in both $\varphi = 0°$ and $\varphi = 180°$ configurations to average out any epilayer tilt. Epilayer and substrate peaks were fitted with Gaussian and Lorentzians to determine the epilayer peak position with respect to the substrate peak. The in-plane and out-of-plane strains were calculated using Bede software “Peak Split”, from which the N (Bi) fraction was calculated assuming a linear interpolation of the GaAs and GaN (GaBi) lattice parameters, along with a Poisson’s ratio of 0.33. It

should be noted that GaBi has not been synthesized; therefore, the GaBi lattice parameter is calculated,[12] and subsequently the GaAsBi analysis is an approximation. The author performed the majority of the HRXRC measurements, and the rest were performed by Dr. Yu Jin, Gulin Vardar, and Tim Jen.

### 2.5 Atomic force microscopy

The surface morphology was examined *ex-situ* with atomic force microscopy (AFM), performed on a Veeco Dimension Icon AFM in the Electron Microbeam Analysis Laboratory (EMAL) by Tim Jen and Davide Del Gaudio. The piezoelectric scanners typically move in a curved motion over the surface, resulting in a "bowing" of the outputted image. To correct for this, all images were "flattened" by subtracting a quadratic background from the image, using NanoScope Analysis Imaging software. Then, various analyses were performed on the images, including surface roughness and section (line-cut) analysis.

### 2.6 Scanning electron microscopy

The surface morphology of GaAsBi films were examined using scanning electron microscopy (SEM), allowing sub-micron imaging of surface features. SEM was performed on a FEI NOVA 200 workstation and Philips XL30 FEG. Subsequently, size analysis was performed on SEM images of GaAsBi films with surface droplets, which is described in Appendix B.3. The composition profiles across the surface droplets were determined using energy dispersive X-ray spectroscopy (EDX) in the FEI NOVA 200 and/or Auger electron spectroscopy (AES) in a Physical Electronics Auger Nanoprobe 680. The SEM, EDX, and

AES measurements were performed in part by the author, and in part by Gulin Vardar, Tim Jen, and Jordan Occena.

For EDX measurements, X-rays excite and eject inner-shell electrons. Subsequently, valence electrons relax and occupy the inner-shell holes, emitting photons of energy equal to the difference in energy between these energy levels. Similarly, in AES, an electron beam excites a sample's surface, exciting inner-shell electrons and creating inner-shell holes. Higher-energy electrons then relax to the empty energy levels via emission of Auger electrons. Furthermore, for EDX (AES) measurements, the energy of the emitted photon (Auger electron) is characteristic to the atomic structure of the element from which the photon (Auger electron) was emitted, and the number of photons (Auger electrons) emitted is related to the relative concentration of atoms. By measuring the energy and number of photons (Auger electrons) emitted, EDX (AES) is able to perform chemical surface mapping.

## 2.7 Ion beam analysis

The total N fraction and the interstitial N fraction, $f_{int}$, were determined using nuclear reaction analysis (NRA) and Rutherford backscattering spectroscopy (RBS) of GaAsN and GaAs films in both [001] nonchanneling and channeling conditions. NRA measurements were performed with the $^{14}N(d,\alpha_0)^{12}C$ and $^{14}N(d,\alpha_1)^{12}C$ reactions. A 1.2-MeV deuterium ion beam was incident on the GaAsN films, and the yields of the reaction-emitting particles ($\alpha_0$ and $\alpha_1$) were then detected by a silicon surface-barrier detector located at 150° with respect to the incident beam direction. A range foil of 12-μm-thick mylar was placed in front of the detector to filter out scattered deuterium particles. The NRA and RBS measurements on

GaAsN films were performed by Dr. Yu Jin at the Michigan Ion Beam Laboratory (MIBL) using a General Ionex 1.7-MV Tandetron accelerator, and are described in more detail in Section 2.7 of Dr. Yu Jin's Ph.D. dissertation.[13]

Similarly, the Bi fraction was measured using RBS in conjunction with simulation of nuclear reaction analysis code (SIMNRA). The samples were mounted onto the sample holder using double-sided Cu tape. Before each measurement, simulations were performed to determine the beam energy and scattering angle which maximizes the signal from the Bi peak. Typically, we performed RBS using 2.1-MeV He at 160°, or 1.3-MeV Deuterium at 160°. During each experimental run, RBS is performed on Au and Si to establish an energy calibration. Simulations were then performed to determine the Bi fraction, where the simulation is normalized to the Ga/As edge. Then, the Bi fraction in the simulation was varied until, under the Bi peak, the integrated simulated spectrum is equal to the integrated experimental spectrum (with the background subtracted). Additionally, this simulated determination of the Bi fraction was compared to an estimate of the Bi fraction that can be obtained from the relative intensity of elemental peaks, as described in Appendix B.2. The author performed the majority of the RBS measurements on GaAsBi films, and the remaining measurements were performed by Gulin Vardar, Tim Jen, and Jordan Ocenna.

## 2.8 Hall and magnetoresistance measurements

### 2.8.1 Overview

To measure the conductivity, mobility, and carrier concentration of GaAsN and GaAsBi films, transport measurements were performed both at room temperature and at

variable temperatures. Samples were fabricated into either Van der Pauw or Hall bar geometries. For Hall bars, photolithography was performed in the LNF at the University of Michigan. Room temperature resistivity and Hall measurements were performed in Prof. Goldman's laboratory in the Materials Science and Engineering Department, while variable-temperature Hall and magnetoresistance measurements were performed in Prof. Kurdak's laboratory in the Physics Department. The majority of sample preparation and measurements were carried out by the author, and the remaining was performed by Dr. Yu Jin. This section presents the Van der Pauw method, and then provides details of sample fabrication and measurement procedures.

### 2.8.2 Van der Pauw method

In 1958, L.J. Van der Pauw showed that the resistivity and Hall coefficient can be extracted from a sample of arbitrary shape (e.g. see Fig. 2.9). This is accomplished using four contacts, provided that (1) the contacts are small and on the edge of the sample, and (2) the sample is of uniform thickness and free of spatial holes.[14] Then, the resistivity, $\rho$, is given by

$$\rho = \frac{\pi d}{\ln 2}\frac{R_{MN,OP} - R_{NM,PM}}{2} f\,, \tag{2.3}$$

where $R_{MN,OP} = V_{OP}/I_{MN}$, and $f \leq 1$ depends on the degree of sample asymmetry ($f = 1$ for a square sample). Furthermore, Van der Pauw showed that $f$ is determined completely by the ratios of adjacent 4-terminal resistances;[14] for the example in Fig. 2.9, $f$ would be determined by the ratio $R_{MN,OP}/R_{NO,PM}$. Recently, $f$ has been more accurately calculated and tabulated.[15] Furthermore, error is introduced due to the finite size of the contacts, or due to contacts not being on the sample edge, as detailed in Appendix E.

### 2.8.3 Van der Pauw samples

Samples prepared in the Van der Pauw geometry (Fig. 2.10) were typically cleaved into 4 mm by 4 mm squares, aiming to achieve $f \approx 1$. Also, small contacts (<0.5 mm) were placed on the corners, in order to minimize error from contact size. For *n*-type (*p*-type) samples, InSn (InZn), obtained from Custom Thermoelectric in ~1:1 ratio, was used for the contacts to increase the likelihood that contacts will be Ohmic. Subsequently, contacts were annealed at 420 °C for 2 min in atmospheric pressure forming gas (90% $N_2$, 10% $H_2$), which reduces the likelihood that contacts will oxidize during annealing since oxides on the contacts can combine with $H_2$ to form $H_2O$. Each contact was manually wired to a 16-pin dip header using 25-μm Cu wires and In solder. The Van der Pauw geometry was used for all room temperature, and some low temperature, transport measurements.

### 2.8.4 Hall bar samples

Select samples were prepared into a Hall bar geometry, as is shown in Fig. 2.11. For Hall bars, the geometry is defined via photolithography and the contacts are removed from the active region; therefore, sources of contact error are essentially eliminated. The photolithography was performed on the MJB-3 in the LNF, as described in Appendix D. Following photolithography, InSn (InZn) was used for contacts on *n*-type (*p*-type) samples, which were annealed at 420 °C for 2 min in atmospheric pressure forming gas (90% $N_2$, 10% $H_2$), as described above. The contacts were manually wired to a 16-pin dip header using 25-μm Cu wires and In solder. Low-temperature transport measurements were performed predominantly on Hall bars.

### 2.8.5 Room-temperature Hall and resistivity measurements

The Ohmic nature of contacts was verified using a Hewlett Packard 4156B precision semiconductor parameter analyzer. Typical contact resistances were 100 Ω to 10 kΩ for the GaAsN and GaAsBi films used in this dissertation work.

For the room-temperature Hall and resistivity measurements, a DC current ranging from 5 μA to 6 mA was sent between two contacts, as described below, using a Keithley 224 programmable current source. Then, the voltage drop between the remaining two contacts was measured using a Hewlett Packard 34420A Nanovolt/microOhm meter. Resistivity measurements were conducted by measuring the voltage parallel to the current flow in the absence of an external magnetic field ($V_{xx}$), as shown in Fig. 2.10. For Hall measurements, the voltage was measured perpendicular to the current ($V_{xy}$), in an external magnetic field (perpendicular to the sample surface) of 0.124 Tesla. From these measurements, the electron mobility and free carrier concentration were determined using the procedures in the ASTM standard F76.[16]

### 2.8.6 Variable-temperature Hall and resistivity measurements

For the variable-temperature Hall and magnetoresistance measurements, samples were inserted into a liquid He (LHe) cryostat with a superconducting magnet, as shown in Fig. 2.12. In this dissertation work, the cryostat functioned in a heating mode, allowing for temperatures ranging from 4.2 K to room temperature. The cryostat has three shells: an outer shell under vacuum to minimize heat exchange between the LHe and room air, a middle shell filled with LHe, and an inner shell housing the sample space. An adjustable

needle valve separates the LHe from the sample space, which controls the flow of LHe over the sample. A PID-regulated heater at the bottom of the sample space heats the flow of LHe, thereby heating or cooling the temperature of the sample. A current is passed through a NbTi superconducting magnet (-72 to +72 A), producing magnetic fields from -8 to +8 Tesla. For samples prepared into Hall bars, two Stanford SR830 Lock-in amplifiers are used to simultaneously measure the longitudinal and transverse voltage (as shown in Fig. 2.11). For samples prepared in the Van der Pauw geometry, two separate measurements are needed to measure the transverse and longitudinal voltage (as shown in Fig. 2.10): one measurement with a magnetic field and one measurement without a magnetic field. In either sample geometry, Lock-in amplifiers permit AC measurements of both the in-phase (resistance) and out-of-phase (capacitance) components of the impedance. When the magnitude of the out-of-phase component is >1/10 the magnitude of the in-phase component, the measurement is considered to be faulty since measurement noise (such as parasitic capacitance in the wires) has become a significant proportion of the measured signal.

### 2.8.7 Low-temperature persistent photoconductivity measurements

For persistent photoconductivity (PPC) measurements, a light-emitting diode (LED) emitting at 945 ± 5 nm was mounted on the 16-pin dip header directly beside a Van der Pauw sample. PPC measurements were performed in both the variable-temperature cryostat from 4.2-60 K (Fig. 2.12), and in a $LN_2$ cryostat at 77 K (Fig. 2.13), which contains one $LN_2$-filled shell in which samples were directly inserted. For measurements in both cryostats, $V_{xx}$ vs. time was measured for each illumination duration.

## 2.9 Photoluminescence

In photoluminescence (PL) measurements, semiconductors are exposed to light of energy greater than the bandgap energy. Subsequently, electron-hole pairs are formed, which relax to the energy band minimum. Electron-hole pairs then recombine via the emission of photons. The resultant spectrum provides a probe of the electronic structure of the material, revealing information about the bandgap energy and defect states. Therefore, to consider the influence of Bi incorporation on the bandgap reduction of GaAsBi, low-temperature PL was collected with a 633-nm (1.96-eV) HeNe laser operating from 1 to 11 mW. The PL measurements were performed at 10 K by Marta Luengo-Kovac and Brennan Pursley in Prof. Sih's research group. Each PL measurement was normalized to the peak intensity of that spectrum.

## 2.10 Figures

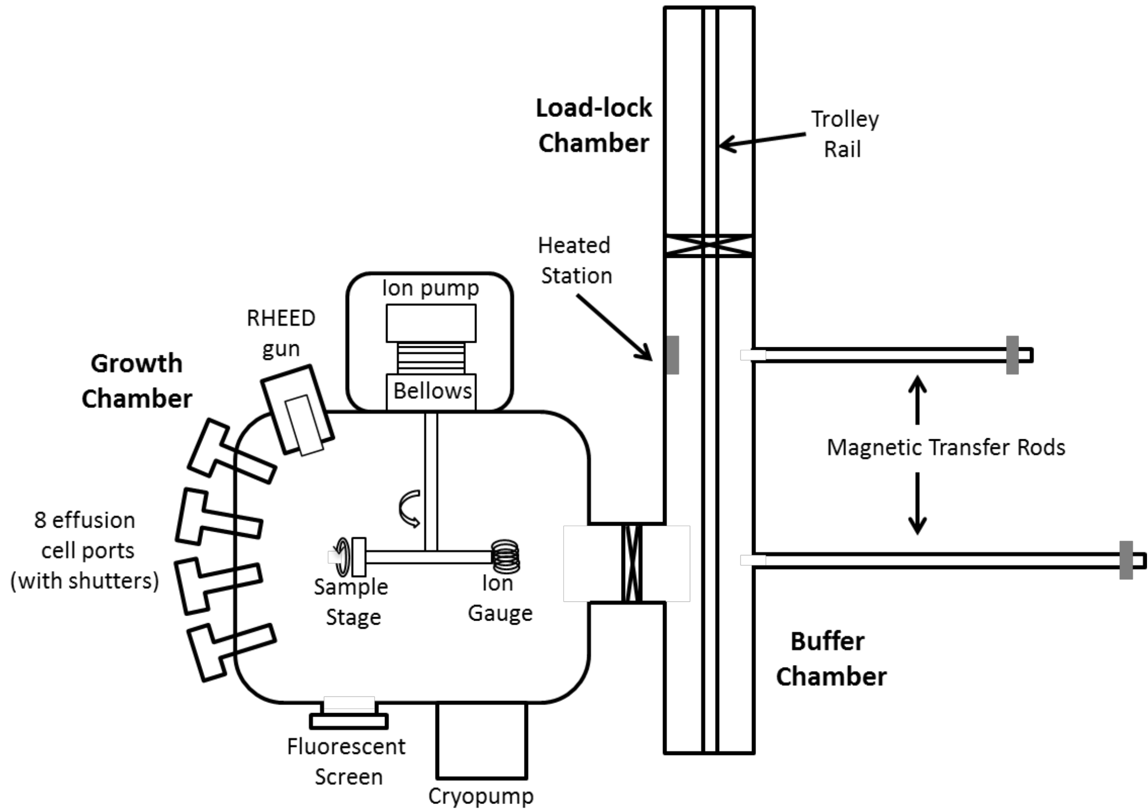


**Figure 2.1** Schematic of the Modified Varian Gen II molecular-beam epitaxy system. The radio frequency plasma source (separated from the main chamber by a gate valve) and seven solid sources (Ga, In, Al, Si, Be, Bi, and As cracker) are each located in one of the effusion cell ports.

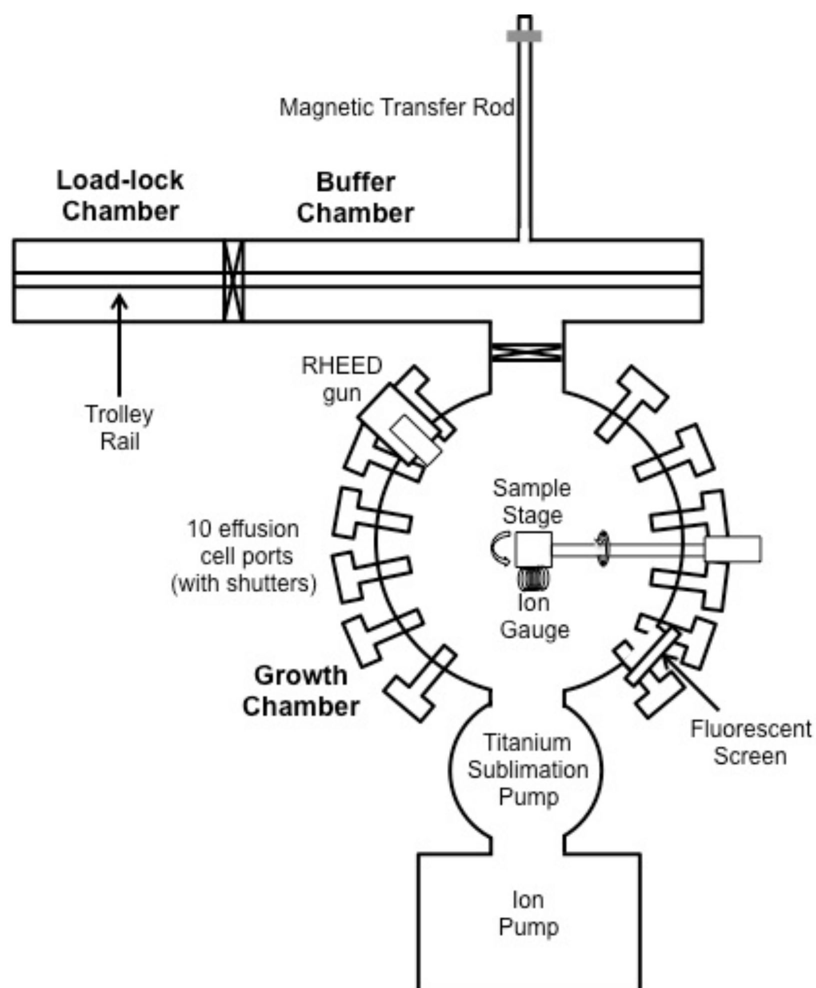


**Figure 2.2** Schematic of the Riber Compact 21 molecular-beam epitaxy system. Seven solid sources (Ga, In, Al, Si, Be, Bi, and As cracker) are each located in one of the effusion cell ports.

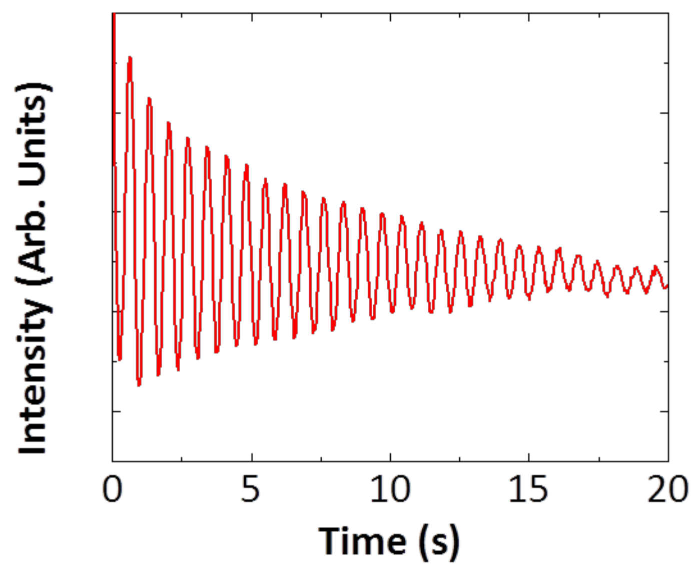


**Figure 2.3** Reflection high-energy electron diffraction intensity as a function of measurement time for a typical GaAs growth rate calibration, for which the Ga and As shutters are always open.

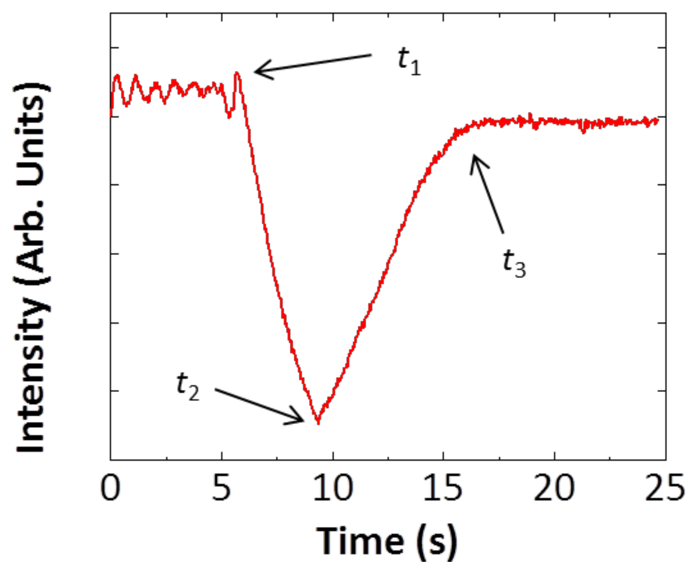


**Figure 2.4** Reflection high-energy electron diffraction intensity as a function of measurement time for an incorporation rate ratio measurement. Here, the Ga shutter is always open; the As shutter closing, reopening, and the surface reconstruction recovery are labeled as $t_1$, $t_2$, and $t_3$, respectively.

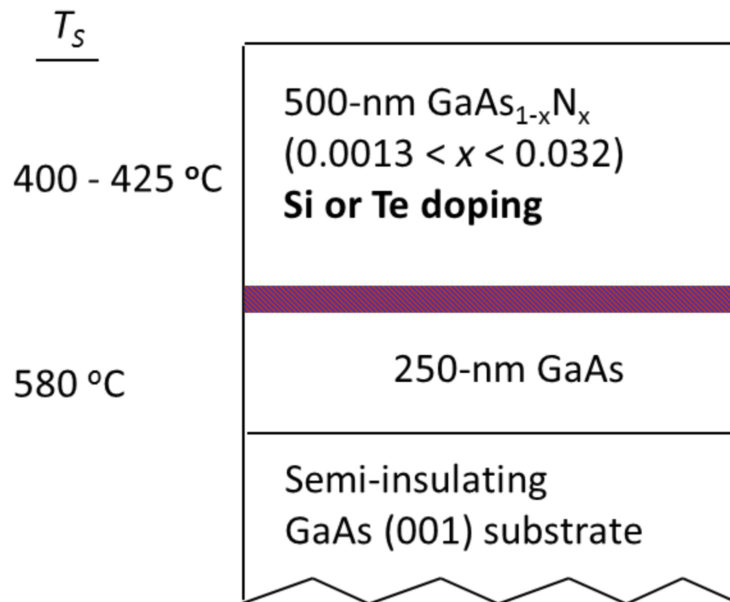


**Figure 2.5** Cross section of the $GaAs_{1-x}N_x$ film structure grown by molecular-beam epitaxy, including layer thickness and substrate temperature, $T_s$.

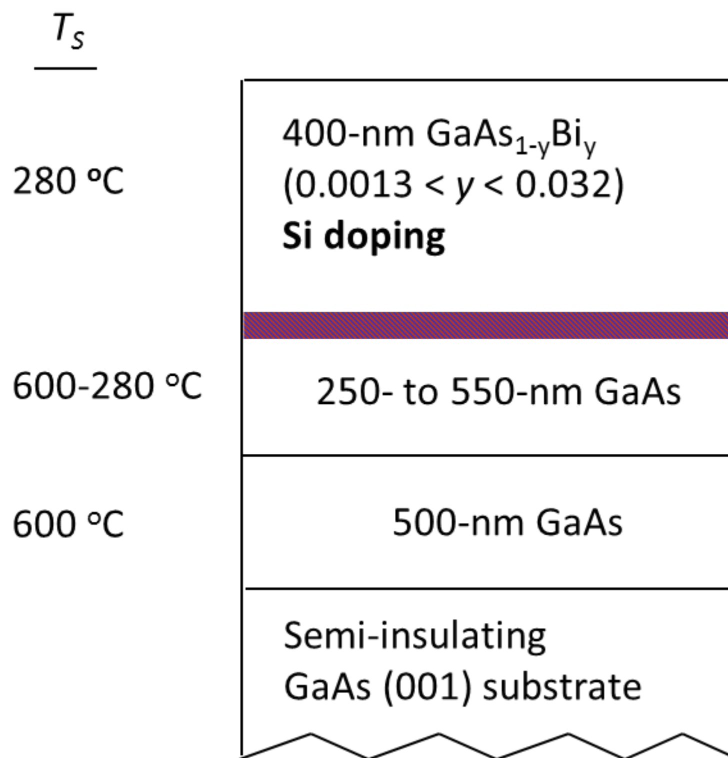


**Figure 2.6** Cross section of the $GaAs_{1-y}Bi_y$ film structure grown by molecular-beam epitaxy, including layer thickness and substrate temperature, $T_s$.

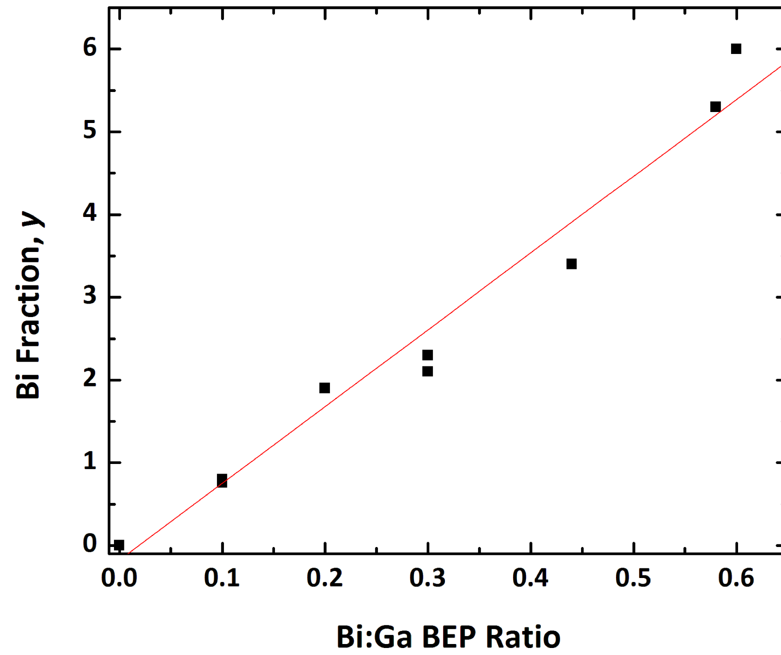


**Figure 2.7** Bi fraction, $y$, vs. Bi:Ga BEP Ratio, κ, for $GaAs_{1-y}Bi_y$:(Si) films. The target Bi fraction can be estimated from a linear interpolation of the $y$ vs. κ data.

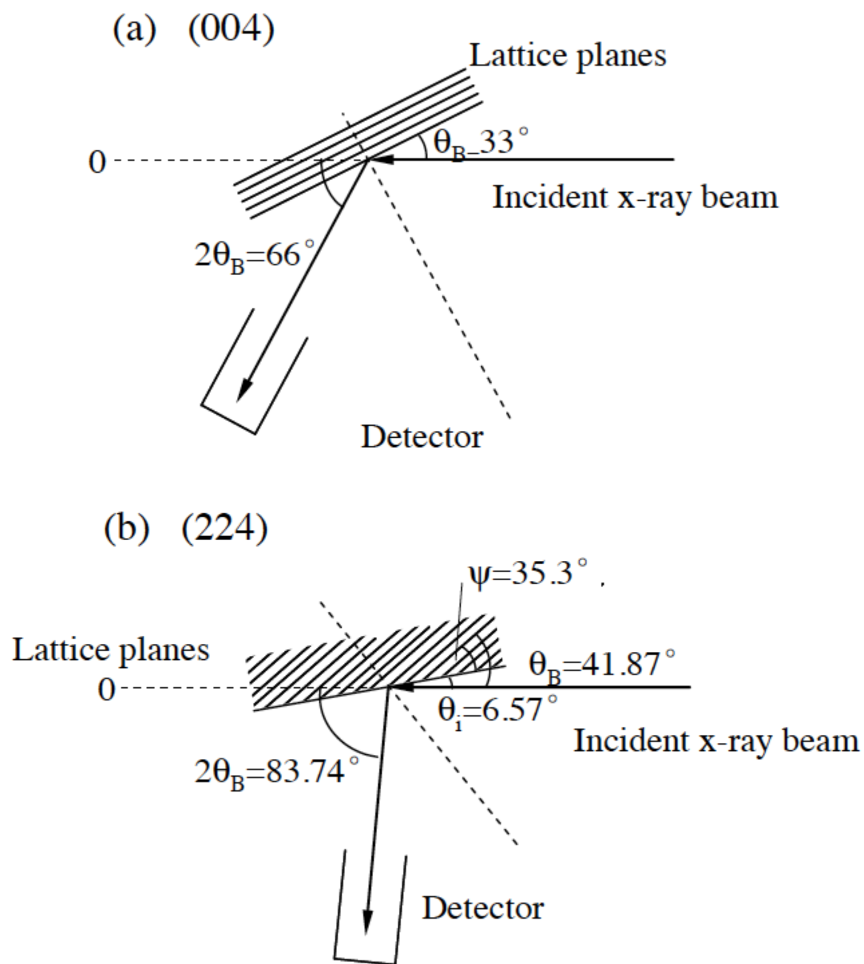


**Figure 2.8** Schematic of high-resolution X-ray rocking curve geometries: (a) symmetric (004) scan, and (b) asymmetric (224) scan. Reprinted with permission from Ref. 13 (Copyright 2010, Yu Jin).

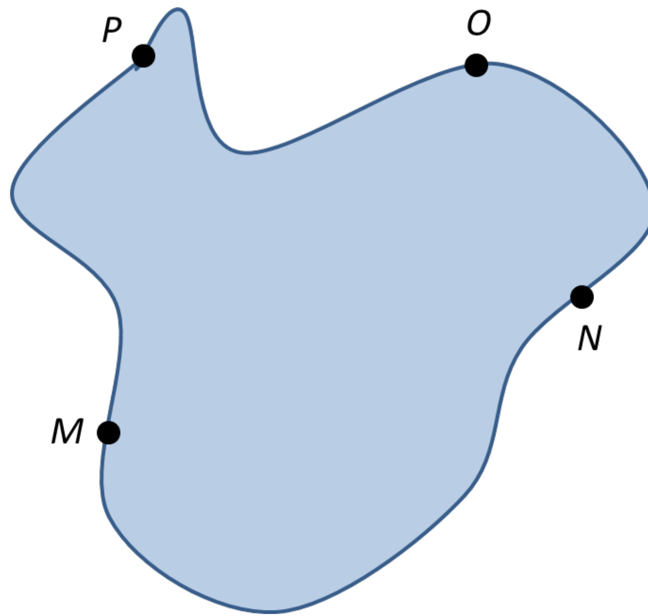


**Figure 2.9** Schematic of a 4-probe measurement from a sample of arbitrary shape, with contacts on the perimeter located at *M*, *N*, *O,* and *P*.

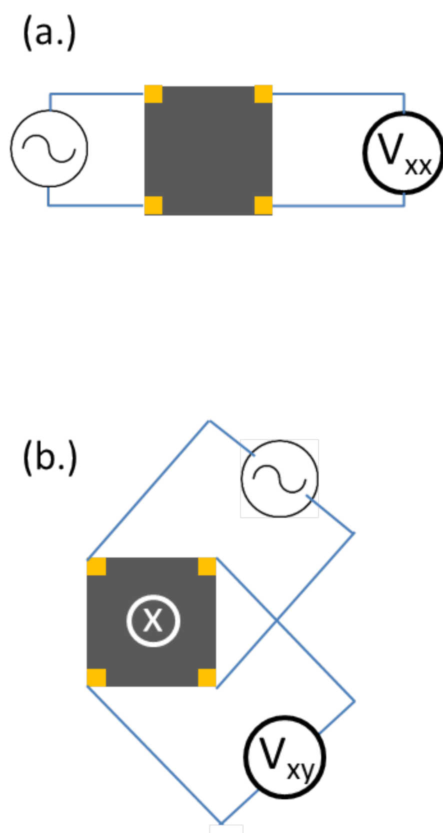


**Figure 2.10** Schematic of a typical symmetric Van der Pauw specimen wired for (a) longitudinal, $V_{xx}$, and (b) transverse, $V_{xy}$, transport measurements.

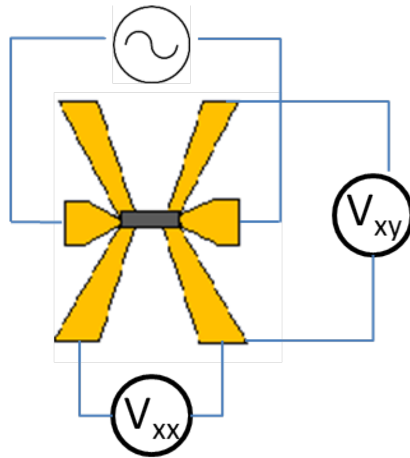


**Figure 2.11** Schematic of a photolithographically defined 6-arm Hall bar used for transport measurements. Hall bars enable simultaneous measurements of voltage in both the longitudinal, $V_{xx}$, and transverse, $V_{xy}$, directions.

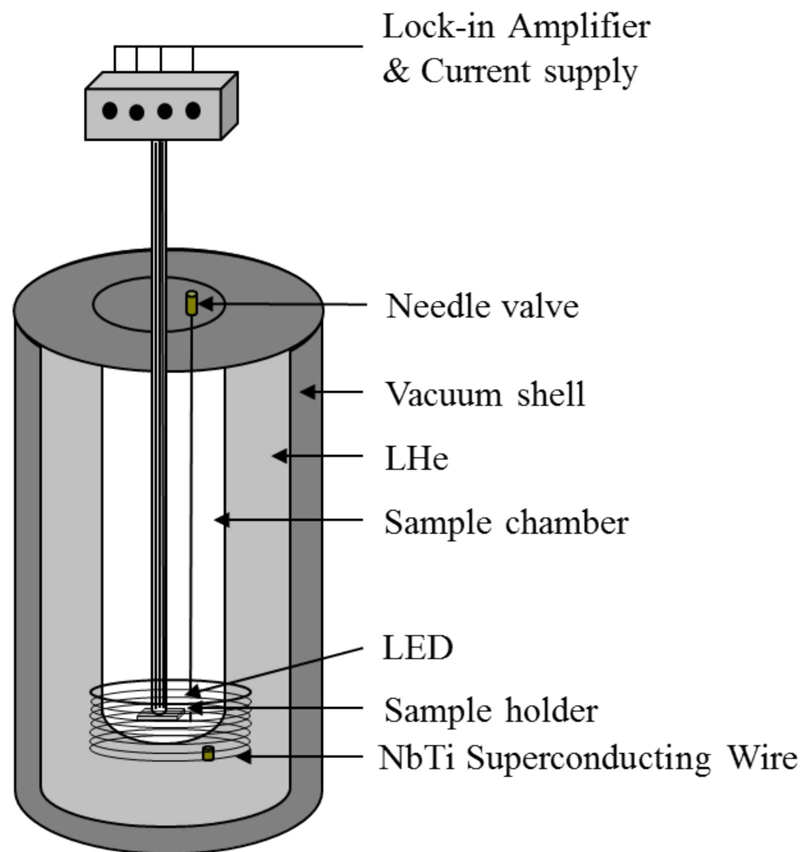


**Figure 2.12** Schematic of the cryostat used for variable-temperature transport measurements. The cryostat is equipped with a superconducting magnet ranging from –8 to +8 Tesla, and can reach temperatures from 1.5 to 300 K. For persistent photoconductivity studies, a light-emitting diode was mounted on the sample holder directly beside the sample. Reprinted with permission from Ref. 13 (Copyright 2010, Yu Jin).

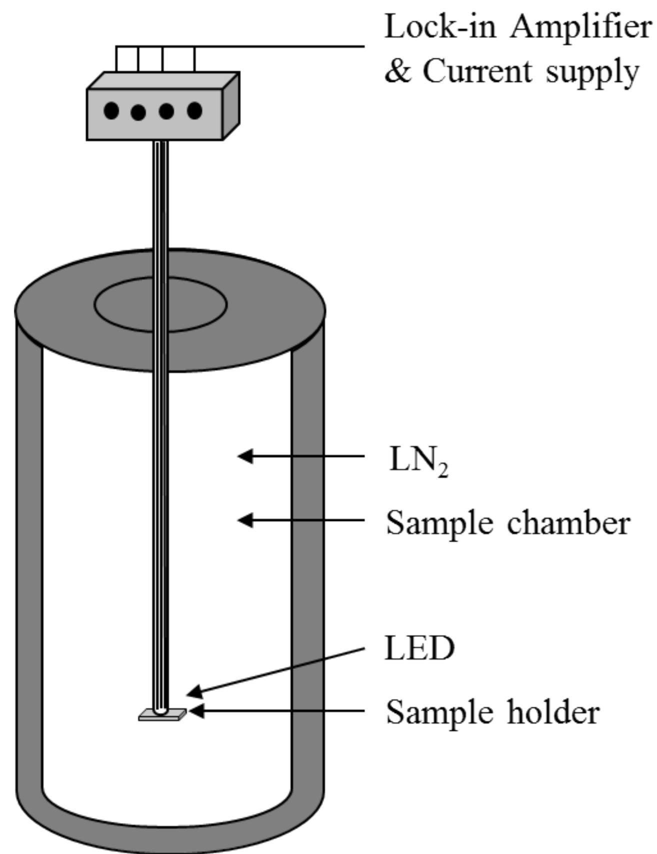


**Figure 2.13** Schematic of the liquid nitrogen cryostat used for 77-K resistivity measurements. For persistent photoconductivity studies, a light-emitting diode was mounted on the sample holder directly beside the sample. Adapted and printed with permission from Ref. 13 (Copyright 2010, Yu Jin).

## 2.11 Reference


[1] A.Y. Cho, J. Cryst. Growth 202, 1 (1999).

[2] A.Y. Cho and J.R. Arthur, Progr. Solid State Ch. 10, 157 (1975).

[3] R.F.C. Farrow, Molecular Beam Epitaxy (Noyes Publications, Park Ridge, NY, USA, 1995).

[4] S. Huang, Ph.D. Thesis 2015, Appendix C, University of Michigan, Ann Arbor, 2015.

[5]T. Vanbuuren, M.K. Weilmeier, I. Athwal, K.M Colbow, J.A. Mackenzie, T. Tiedje, P.C. Wong and K.A.R. Mitchell, Appl. Phys. Lett. 59, 464 (1991).

[6] A.J. Springthorpe, S.J. Ingrey, B. Emmerstorfer, P. Madeville and W.T. Moore, Appl. Phys. Lett. 50, 77 (1987).

[7] S. Banks, An Introduction to MBE, http://lase.ece.utexas.edu/mbe.php; Download 3:00pm (February, 19, 2015).

[8] M. Reason, H.A. McKay, W.Ye, S. Hanson, R.S. Goldman, and V. Rotberg, Appl. Phys. Lett. 85, 1692 (2004).

[9] M. Reason, N.G. Rudawski, H.A. McKay, X. Weng, W. Ye, and R.S. Goldman, J. Appl. Phys. 101, 083520 (2007).

[10] W. Ye, S. Hanson, M. Reason, X.Weng, and R.S. Goldman, J. Vac. Sci. Technol. B 23, 1736 (2005).

[11] E. F. Schubert, Doping in III-V Semiconductors (Cambridge University Press, Cambridge, UK, 1993) pp. 268.

[12] A. Janotti, S.-H. Wei, and S.B. Zhang, Phys. Rev. B 65, 115203 (2002).

[13] Y. Jin, Ph.D. Thesis, Ch. 2, University of Michigan, Ann Arbor, 2010.

[14] L.J. Van der Pauw, Philips Res. Repts. 26, 220 (1958).

[15] A.A. Ramadan, R.D. Gould, and A. Ashour, Thin Solid Films 239, 272 (1994).

[16] AFM Standards, Designation F 76, "Standard Test Methods for Measuring Resistivity and Hall Coefficient and Determining Hall Mobility in Single-Crystal Semiconductors".

# Chapter 3

# GaAsN: Electronic States

## 3.1 Overview

In this chapter, we examine electronic properties and states of GaAsN alloys. The objective of this chapter is to explore the origins of persistent photoconductivity (PPC) in GaAsN, and to present a new method for extracting the effective mass using PPC to drive the metal-insulator transition.

This chapter opens with background information, including a description of PPC, N-induced levels, GaAsN effective mass, and the metal-insulator transition. Next, the experimental details for these investigations are described. The bulk of this chapter is devoted to PPC in GaAsN. First, we present nuclear reaction analysis (NRA) data and both the time and temperature dependence of the GaAsN resistivity and carrier concentration. Then, a physical model for the origins of the PPC effect is proposed. Finally, we propose a new method for extracting effective mass, whereby PPC is used to drive the metal-insulator transition.

## 3.2 Background

### 3.2.1 Persistent photoconductivity

In semiconductors, illumination often leads to an increase in the free-carrier density, and consequently, the conductivity—a phenomenon termed photoconductivity. Following the termination of illumination, typical semiconductors experience conductivity decay on nanosecond timescales. However, some semiconductors exhibit PPC, in which an illumination-induced increase in conductivity persists after the termination of illumination,[1-3] up to hours or days.[4] PPC is often attributed to a large-lattice relaxation, as shown in Fig. 3.1, in which carriers are photoexcited from a ground state associated with a donor complex to the conduction-band edge (CBE). The subsequent return of carriers to the ground state is hindered by an energy barrier, $E_c$, associated with a lattice relaxation needed for the photoexcited state to accept carriers. In doped $Al_zGa_{1-z}As$ alloys with $z > 0.2$, PPC has been observed and attributed to the photoexcitation of free carriers from a $DX^-$ donor complex, consisting of threefold coordinated $Si_{Ga}$, to a shallow donor level.[5,6] In the case of InGaAsN alloys, PPC has been attributed to the photoexcitation of free carriers from N-related deep donor[7,8] or acceptor[9] complexes with unspecified atomic structures. Furthermore, in GaAsN alloys, an annealing-induced increase in carrier concentration and a transition from variable range hopping to extended band conduction has been explained by a corresponding decrease in the interstitial N concentration.[10,11] Indeed, the concentration and local atomic environment of solute atoms determine the properties of semiconductor alloys.

### 3.2.2 N-induced levels in GaAsN

In GaAsN alloys, a variety of electronic levels associated with N pairs and/or cluster states—i.e., N-induced levels—have been reported.[12-22] Furthermore, the CBE of GaAsN has been reported to vary with temperature;[23] thus, the positions of the N-induced levels with respect to the CBE may also vary with temperature. It has been reported that the number and positions of the N-induced levels are dependent on the N fraction, $x$.[12-16] In the ultra-dilute $x$ regime ($x < 0.0001$), single-impurity N levels form a resonant state above the CBE.[24-26] With increasing $x$, N pair and cluster states are apparent,[12-18] resulting eventually in the formation of an impurity band.[15,16]

### 3.2.3 GaAsN effective mass

Due to strong electron scattering from N-induced levels, accurate measurements of the GaAsN effective mass, $m_e$*, using traditional methods have proven difficult. Indeed, cyclotron resonance, Faraday rotation, and Faraday oscillation require uninhibited trajectories for electrons, and thus are not reliable measurements for a system exhibiting strong disorder. Subsequently, there are conflicting experimental[27-29] and theoretical[30,31] reports of the $x$-dependence of $m_e$* in GaAsN, as show in Fig. 3.2.[32] The band anti-crossing (BAC) model of Shan only considers single local atomic environments, and thereby predicts a monotonic increase in $m_e$*.[31] On the other hand, the linear combination of isolated N resonant states (LCINS) model of Lindsay includes hybridization between the conduction band edge and N cluster states, and predicts a non-monotonic increase of $m_e$* with increasing $x$, due to contributions from the cluster states of N-Ga-N and N-Ga-N-Ga-N chains.[33]

Experimentally, Dannecker reported a non-monotonic increase of $m_e$* in GaAsN:Te with increasing $x$ using a combination of Seebeck and Hall measurements, consistent with the LCINS model.[34] Similarly, Se-doped GaAsN exhibits a monotonic increase of $m_e$* with increasing $x$. On the other hand, a monotonic increases of $m_e$* has been reported in Si-doped GaAsN, consistent with the predictions of the BAC model, which has been explained by the amphoteric nature of Si: since Si can occupy both Ga and As sites, Si could replace Ga in the N-Ga-N and N-Ga-N-Ga-N chains.[32] This would suppress the predicted peaks of the LCINS model for $m_e$*, and produce a monotonic increase in agreement with the BAC model. This is in contrast to Te and Se doping, since these dopants would only occupy As sites, and hence would not deter the formation of N-Ga-N and N-Ga-N-Ga-N chains.

### 3.2.4 Metal-insulator transition

A material transitions from an insulator to a metal as electronic states evolve from localized to extended states. This "metal-insulator transition" occurs when the Fermi level is increased above the mobility edge, which occurs at a critical carrier concentration, $n_c$. When the Fermi level is below the mobility edge, charge carriers occupy localized states and do not contribute to the conductivity of the material; semiconductors with $n < n_c$ are referred to as non-degenerate. On the other hand, when the Fermi level is above the mobility edge, charge carriers are de-localized and occupy extended states, causing the material to behave as a metal; semiconductors with $n > n_c$ are referred to as degenerate. Remarkably, the empirical plot of the interdonor distance, $a$*, vs. $n_c$ shows that a variety of materials—semiconductors, metal-ammonia, metal-noble gases, and superconducting cuprates—follow a linear relationship, as shown in Fig. 3.3.[35] Subsequently, according to the Mott criterion, the de-localization

of electrons from localized states occurs when either the density of conducting electrons, or $a^*$, increases:[36]

$$n_c^{1/3} a^* = 0.26 \cdot \tag{3.1}$$

Thus, for a material system with a given $a^*$, the criterion $n > n_c$ must be satisfied for metallic conduction, where $a^*$ is dependent on the effective mass and the dielectric constant, $\epsilon$:

$$a^* = \frac{4\pi\epsilon\hbar^2}{e^2 m_e^*} . \tag{3.2}$$

Whence, by assuming the universality of the Mott criterion (Eq. 3.1), a measurement of $n_c$ will directly determine $m_e^*$. Furthermore, due to the power dependence of $n_c$ and $a^*$ in Eq. 3.1, any error in $n_c$ will lead to significantly less error in $a^*$ (and thus $m_e^*$), leading to an accurate determination of the effective mass.

The metal–insulator transition can be defined as a vanishing of residual conductivity, $\sigma_{min}$, at zero temperature. Therefore, since we perform experiments at finite $T$, we need a theoretical framework of the physics at the metal–insulator transition. Thus, we are not testing the universality of these theories, but are employing them to determine $\sigma_{min}$, from which we can extract $n_c$ when $\sigma_{min} = 0$.

At $T = 0$ K, Al'tshuler showed that there is a minimum conductivity for metallic systems:[37]

$$\sigma(T) = \sigma_{min} + T^m \quad , \tag{3.3}$$

where $\alpha$ is a material parameter, and $m$ is the critical exponent for conduction. It has been reported that $m$ has a value of 1/3 near the metal–insulator transition, and a value of 1/2 for metallic behavior.[37-40] A value of $m = 1/3$ near the metal–insulator transition has been reported for various systems, including GaAs,[41] CdSb,[42,43] $InO_w$,[44] and Ge.[45] Therefore, we assume $m = 1/3$ for the GaAsN films studied in this dissertation work.

### 3.3 Experimental details

$GaAs_{1-x}N_x$ alloy films were grown on (001) semi-insulating GaAs substrates by molecular-beam epitaxy (MBE), using solid Ga, $As_2$ or $As_4$, Si or GaTe (for *n*-type doping), and an $N_2$ RF plasma source. The free-carrier concentrations were 5 to 13 × $10^{17}$ $cm^{-3}$, as determined by Hall measurements in GaAs control films. The N fraction, $x$, in the $GaAs_{1-x}N_x$ layers was adjusted from $x = 0.0013$ to 0.032 by varying the gas flow rate, monitored by the partial pressure of active N, using a residual gas analyzer.[10,11,46,47] For all films, a 250-nm-thick GaAs buffer layer was grown at 580 °C,[48] followed by the growth of a 500-nm GaAs(N):Te or GaAs(N):Si layer in the range 400 to 425 °C.[47] For select films, postgrowth rapid-thermal annealing (RTA) was performed from 650 to 780 °C for 60 s in an $N_2$ atmosphere, with a GaAs proximity cap to prevent As outdiffusion.

The N composition and the interstitial N fraction, $f_{int}$, were determined using NRA and RBS of GaAsN and GaAs films in both [001] nonchanneling and channeling conditions. NRA measurements were performed with the $^{14}N(d,\alpha_0)^{12}C$ and $^{14}N(d,\alpha_1)^{12}C$ reactions.[49] A 1.2-MeV deuterium ion beam was incident on the GaAsN films, and the yields of the reaction-emitting particles ($\alpha_0$ and $\alpha_1$) were then detected by a silicon surface-barrier detector located at 150° with respect to the incident beam direction. A range foil of 12-μm-thick mylar was placed in front of the detector to filter out scattered deuterium particles.

Using both van der Pauw and Hall bar geometries, as described in Sec. 2.8.3 and Sec. 2.8.4, variable-$T$ resistivity and Hall measurements were performed from 1.6 K to room temperature. For the PPC effect study, each film was illuminated using a light-emitting diode (LED) emitting at 945 ± 5 nm. To achieve thermal equilibrium prior to illumination, the GaAsN films were cooled to and held at the measurement $T$ for more than 10 min. The

films were then continuously illuminated until the resistivity, $\rho$, decreased to saturation. After the LED was switched off, $\rho$ was recorded as a function of time. To ensure that each set of relaxation data was obtained with the same initial conditions, the films were subsequently reheated (without illumination) to at least 200 K for more than 10 min prior to cooling to the next measurement *T*. To extract the electron effective mass, the carrier density of GaAsN films was varied using PPC, and then the temperature dependence was measured over the range 4.2-60 K. At 60 K the films were illuminated, and then Hall and resistivity measurements were taken. Subsequently, the temperature was swept down to 4.2 K (via cooling by a flow of LHe at 4.2 K) and back up 60 K (via heating by a flow of heated LHe), over a span of 3-13 hrs. The temperature was kept low to minimize thermal relaxation of photogenerated carriers.

### 3.4 Origins of persistent photoconductivity

#### 3.4.1 PPC magnitude and electron-capture barrier

In Fig. 3.4, we plot the magnitude of the PPC effect, $\sigma_{PPC}^{N}$, as a function of $x$, measured at 77 K for various $GaAs_{1-x}N_x$:Si films. We define $\sigma_{PPC}^{N}$, the increase in conductivity following the termination of illumination, normalized to the preillumination conductivity, as follows:

$$\sigma_{PPC}^{N} = \frac{\sigma_s - \sigma_d}{\sigma_d} \quad , \tag{3.4}$$

where $\sigma_d$ is the conductivity prior to illumination and $\sigma_s$ is the sustained conductivity obtained 1600 s following the termination of illumination. The inset to Fig. 3.4 shows a typical 77-K PPC trace, whereby a $GaAs_{0.985}N_{0.015}$ film, initially in the dark, is illuminated until the conductivity increases to saturation. Following the termination of illumination, the photocurrent persists for more than 1 h. It is interesting to note that PPC becomes significant for $x > 0.006$, due to either an increase in the density of N-induced levels or a change in the relative energy positions of the N-induced level and the CBE, with the N-induced level energy entering the band gap.

To extract the energy barrier hindering the relaxation of photogenerated carriers from the CBE to the ground state of the N-induced level—i.e., the electron-capture barrier, $E_c$ —the photocurrent was monitored in 10 K increments from 120 to 160 K; in this measurement $T$ range, the decay timescales were short enough to be measurable. Figure 3.5(a) shows a typical set of time-dependent normalized photoconductivity data, $\sigma_t^N$, for a $GaAs_{0.987}N_{0.013}$:Te film, with $t = 0$ defined as the instant of illumination termination. The contribution from photogenerated free carriers, normalized to unity at $t = 0$, becomes

$$\sigma_t^N = \frac{\sigma_t - \sigma_d}{\sigma_0 - \sigma_d} , \tag{3.5}$$

where $\sigma_0$ is the conductivity at $t = 0$ and $\sigma_t$ is the conductivity at time $t$.

We consider the photocurrent relaxation process in terms of a stretched-exponential expression:

$$\sigma_t^N \propto \exp\left[-\left(\frac{t}{\tau}\right)^{\beta}\right] , \tag{3.6}$$

where $\tau$ is the characteristic decay time and $\beta$ is the decay exponent. For this approach, the normalized conductivity is plotted in the form of $\ln[\ln(1/\sigma_t^N)]$ vs. $\ln(t)$, as shown in Fig. 3.5(b), with $\beta$ ranging from 0.15 to 0.38. At each measurement $T$, the available $x$-intercepts at $y = 0$ are identified as $\tau$. To minimize extrapolation errors, this analysis only includes data sets that intersect the $x$-axis in the plot of $\ln[\ln(1/\sigma_t^N)]$ vs. $\ln(t)$. The electron-capture barrier is then extracted by plotting the $T$ dependence of $\tau$ as

$$\tau = \tau_0 \exp\left(\frac{E_c}{k_B T}\right), \tag{3.7}$$

where $k_B$ is the Boltzmann constant and $\tau_0$ is the high-$T$ limit of $\tau$. As shown in the inset of Fig. 3.5(b), a linear least-squares fit to $\ln(\tau)$ as a function of $1000/T$ was employed to determine $E_c$. Similar analyses reveal an $E_c$ value of 280 ± 20 meV for $GaAs_{1-x}N_x$ films with $x$ ranging from 0.0075 to 0.019, apparently independent of $x$. We note that the reported variation in CBE over our measurement $T$ range (~10 meV)[23] is negligible compared with $E_c$; thus, any changes in the alignment of the density of N-induced levels with respect to the CBE is insignificant. The $E_c$ values for our GaAsN films are comparable to those of GaAsP films (120 ± 30 meV for Te doping)[50] and AlGaAs films (180 ± 20 meV for Te doping and 330 ± 50 meV for Si doping)[5,51] but are lower than reported values for unintentionally doped (In)GaAsN alloys (664 meV for $x$ = 0.008, 570 meV for $x$ = 0.013, and 349 meV for $x$ = 0.018).[7,8,9] Hence, In may increase the electron-capture barrier in InGaAsN films; the lattice relaxation needed for the N-induced complex to accept carriers might be inhibited by the localization of N at In-rich regions.[52,53]

### 3.4.2 Activation energy

Typically, the energy to thermally activate carriers from donor states to the CBE is termed $E_a$. Therefore, to determine $E_a$, we consider the temperature dependence of the carrier concentration for GaAsN films. In addition to N-induced levels, the doped GaAsN:Te (GaAsN:Si) films have a Te- (Si-) induced shallow donor level associated with $Si_{Ga}$ ($Te_{As}$). Figure 3.6 shows $n$ vs. 1000/$T$ for various GaAsN films in comparison with that of GaAs:Te. Although $n$ is independent of measurement $T$ for GaAs:Te,[54,55] two distinct measurement $T$ regimes of $n$ are apparent for the GaAsN films. For low measurement $T$, $n$ is independent of $T$, presumably due to the low activation energy for the shallow donor levels in GaAsN.[55] For high measurement $T$, $n$ increases exponentially with increasing measurement $T$, suggesting the thermal activation of electrons from N-induced levels to the GaAsN CBE.

To extract $E_a$, we assume the coexistence of a shallow donor level and a N-induced level in the context of a two-level system formalism, assuming that the N-induced level follows the CBE:[5]

$$\sqrt{n(n-n_S)} \propto \exp\left(-\frac{E_a}{2k_B T}\right), \tag{3.8}$$

where $n_s$ is the shallow donor concentration, obtained from an analysis of $n_s$ vs $T$ data in the low measurement $T$ regime. In Fig. 3.6, we plot $n$ vs 1000/$T$ and overlay this with $\sqrt{n(n-n_S)}$ vs. 1000/$T$ (in open circles) for $n > n_s$. $E_a$ values are then extracted from the slopes of linear least-squares fits of $\sqrt{n(n-n_S)}$ vs. 1000/$T$ for $n > n_s$. For $GaAs_{1-x}N_x$ alloys with $x$ increasing from 0.0075 to 0.019, $E_a$ decreases from 105 to 60 meV, as shown in

Fig. 3.7. Hence, as $x$ increases, the N-induced level presumably remains in the band gap and approaches the CBE. We note that this activation energy is similar to that of Te donors in GaAsP films (70 meV)[50] and also Te and Si donors in AlGaAs films (100 ± 50 meV)[5,51] but is significantly greater than the activation energy of shallow Te donors (30 meV) and Si donors (4–6 meV) in GaAs.[55,56] In contrast, for $Al_zGa_{1-z}As$ alloys, the donor state attributed to PPC enters the band gap for $z > 0.20$;[5] thus, a new PPC mechanism for GaAsN needs to be identified.

Now, we consider the possible composition and temperature dependence of the N-induced level energy. For the composition range $x$ = 0.0075 to 0.019, the observed N composition dependent decrease in $E_a$ (~45 meV) is less than the reported decrease in the CBE (~130 meV),[16] implying that the $x$ dependence of the N-induced level may not follow that of the CBE. For our measurement $T$ range, ~150 to 300 K, the CBE has been reported to be linearly dependent on temperature.[23] Thus, we consider the extreme when the N-induced level remains fixed, while the CBE is linearly dependent on $T$. We note that the Arrhenius analysis is insensitive to linear corrections to the energy term; thus, we conclude that $E_a$ would not be influenced by any $T$ dependence of the N-induced level energy with respect to the CBE.

### 3.4.3 Influence of RTA

To elucidate the origins of the PPC effect in GaAsN, we compare $E_a$, $\sigma_{PPC}^{N}$, and $f_{int}$ before and after RTA. In Fig. 3.8, we plot $n$ vs. $1000/T$ for GaAsN films annealed at various temperatures, including Si-doped $GaAs_{0.985}N_{0.015}$ films [Fig. 3.8(a)] and Te-doped $GaAs_{0.984}N_{0.016}$ films [Fig. 3.8(b)]. After RTA, $n_s$ increases, suggesting that the concentration

of N-induced donors has been reduced by annealing. Extraction of $E_a$ using the 2-level formalism, as described in Sec. 3.4.2, reveals that $E_a$ = 72 ± 5 meV and remains unchanged after RTA for films of both dopant species (Si vs Te). On the other hand, an RTA-induced reduction of $\sigma_{PPC}^{N}$ for a GaAsN film is shown in Fig. 3.4. Hence, $\sigma_{PPC}^{N}$ is likely influenced by RTA-induced changes in N incorporation mechanisms.

We now consider the influence of RTA on N incorporation mechanisms. In Fig. 3.9, the measured interstitial [N] is plotted as a function of total [N] for $GaAs_{1-x}N_x$ films with $x$ ranging from 0.01 to 0.032. The solid blue and hollow red symbols connected with dashed lines represent GaAsN films before and after RTA, respectively. For the as-grown GaAsN films, a linear least-squares fit of the interstitial [N] as a function of total [N] suggests that approximately 20% of N is incorporated interstitially, similar to earlier reports.[46] Following RTA, the total [N] remains constant to within experimental error, while the interstitial [N] is reduced to approximately 10%, possibly due to the diffusion of interstitial N atoms to nearby As vacancies.[57]

### 3.4.4 Model for electronic states in GaAsN

In many doped semiconductor alloys, PPC has been observed and attributed to the photoexcitation of free carriers from a dopant-induced complex to a shallow donor or acceptor level. In GaAsN, since the RTA-induced suppression of $\sigma_{PPC}^{N}$ is accompanied by a reduction in $f_{int}$, the N-induced level leading to PPC is likely associated with N interstitials. Furthermore, Fig. 3.7 shows that $E_a$ decreases with increasing $x$, indicating that the N-induced level energy remains in the band gap and approaches the CBE as $x$ increases. Thus,

the increase in $\sigma_{PPC}^{N}$ for $x > 0.006$, shown in Fig. 3.4, is due to an increase in the density of N-induced levels.

We now propose a mechanism for the PPC effect in GaAsN. As shown in Fig. 3.10, the Si- or Te-induced donor level, d, remains near the CBE in both the "ground" (left) and "photoexcited" (right) states of GaAsN. On the other hand, the energy of the N induced level in the ground (photoexcited) state of GaAsN is below (above) the GaAsN CBE.[58] Photoexcitation of carriers from the ground state of the N-induced level to the GaAsN CBE leads to an enhanced conductivity, and also induces modifications to the N molecular bond configuration. The photoexcited state of the N-induced level has a higher energy than its ground state, namely, it is above the CBE. When illumination is terminated, carriers in the photoexcited state of the N-induced level are unable to immediately return to the ground state. With the addition of thermal energy, $E_c$ is overcome and the ground state configuration of the N-induced level is restored. The N-induced level is once again able to accept carriers, and the conductivity decays to its preillumination value. The molecular bond configurational change may be a bond reorientation or a shift in the molecular center of mass. Similarly, two bistable configurations have been reported for C pairs in Si due to a bond reorientation and rotation of the C pair.[59]

### 3.5 Using PPC to probe the metal-insulator transition in GaAsN

The PPC effect permits the study of transport properties as a function of carrier concentration. Therefore, we have explored transport properties of bulk dilute nitride films at cryogenic temperatures. At low carrier densities, the samples exhibit insulating behavior where the resistivity diverges as the temperature approaches zero, consistent with the Mott

criterion for variable-range hopping mechanism. At high carrier densities, the sample resistivities are weakly dependent on temperature. We used PPC to drive the metal-insulator transition in GaAsN, going from insulating to conducting behavior.

To extract effective mass, $n$ must be slightly less than $n_c$, such that the increase in $n$ due to PPC will induce a metal–insulator transition. If a film is too insulating, the film will remain insulating when the increase in $n$ due to PPC saturates. Since the effective mass (and subsequently $n_c$) for GaAsN varies with $x$, the initial $n$ a sample must have is specific for a given $x$. However, this limitation is expected to be less restrictive at larger $x$, since the PPC magnitude increases with increasing $x$ (Fig. 3.4). Thus, the increase in $n$ due to PPC is more significant as $x$ increases, and $n$ can be further below $n_c$ while still being able to drive the metal–insulator transition. However, the ability to tune $n$ using PPC is advantageous since the metal–insulator transition can be crossed using a single sample, rather than requiring multiple samples on both sides of the metal–insulator transition.

In Fig. 3.11, we plot resistivity, $\rho$, as a function of $T$ for a $GaAs_{0.987}N_{0.013}$:Si film. Illuminating the film induces PPC, thereby increasing $n$ of the film from $2.4 \times 10^{17}$ to $3.3 \times 10^{17}$ at saturation of the PPC effect. The temperature dependence of $\rho$ is due to N incorporation into GaAs, becoming more significant as $x$ increases.[34,60] In Fig. 3.12, we replot this data in the form of conductivity, $\sigma$, vs. $T^{1/3}$, in order to linearize the metallic conduction (Eq. 3.3). For each illumination, $\sigma_{min}$ is determined from the $y$-intercept in the plot of $\sigma$ vs. $T^{1/3}$. To determine $n_c$, we take a linear interpolation of $n$ vs. $\sigma_{min}$ for all of the illuminations (Fig. 3.13); then, $n = n_c$ when $\sigma_{min} = 0$. For the $GaAs_{0.987}N_{0.013}$:Si film, we find that $n_c = 3.0 \times 10^{17}$ cm$^{-3}$. For GaAsN, the dielectric constant has been measured as $\epsilon = 10.6$ for a film with $x = 0.01$;[61] we use an interpolation of this value, along with a dielectric

constant of $\epsilon = 12.9$ for GaAs, to obtain a dielectric constant of $\epsilon = 9.9$ for $x = 0.013$. Then, the Mott Criterion yields $m_e^* = 0.13m_e$ for our $GaAs_{0.987}N_{0.013}$:Si film.

Additionally, we attempted to induce metal-insulator transitions in $GaAs_{0.985}N_{0.015}$:Si and $GaAs_{0.981}N_{0.019}$:Si films; however; these films remained insulating at the saturation of the PPC effect. We can obtain lower-bounds of $m_e^*$ for these insulating films from the measured value of $n$ at the saturation of the PPC effect. In Fig. 3.2, we plot our measured value of $m_e^*$ (the star symbol) and lower-bounds of $m_e^*$ (the upward-pointing arrows), along with literature reports of $m_e^*$. Our value, and lower-bounds, of $m_e^*$ are consistent with the predictions of the LCINS model, and also are larger than the predictions of the BAC model, suggesting that N cluster states may influence $m_e^*$ in GaAsN:Si. This is in contrast to the data for GaAsN:Si reported by Pichanusakorn, which is consistent with the BAC model.[32]

### 3.6 Conclusions

In summary, we have investigated the influence of N environment on the PPC effect in $GaAs_{1-x}N_x$. For $x > 0.006$, significant PPC is observed at cryogenic temperatures with the PPC magnitude increasing with increasing $x$, due to an increase in the density of N-induced levels. Since RTA suppresses $\sigma_{PPC}^{N}$ and reduces $f_{int}$, the N-induced level is likely associated with N interstitials. PPC in GaAsN is attributed to the photoexcitation of carriers from a N-induced level to the CBE, leading to a modified molecular bond configuration of the N-induced level. With sufficient thermal energy, the original N-induced level configuration is restored, and the N-induced level is able to accept carriers once again. The change in molecular bond configuration is likely a bond reorientation or a shift in the center of mass.

In addition, we have used PPC to drive a metal-insulator transition in GaAsN, allowing us to extract $m_e$* using the Mott criterion. This is substantial for GaAsN, since strong electron scattering hinders accurate measurements of $m_e$* using tradition methods, such as cyclotron resonance which requires uninhibited trajectories for electrons. We find that $m_e$* for Si-doped GaAsN is consistent with predictions of the LCINS model, which considers N clustering. This new method for extracting $m_e$* is likely to be applicable to a wide variety of systems, especially to those exhibiting strong disorder.

### 3.7 Figures

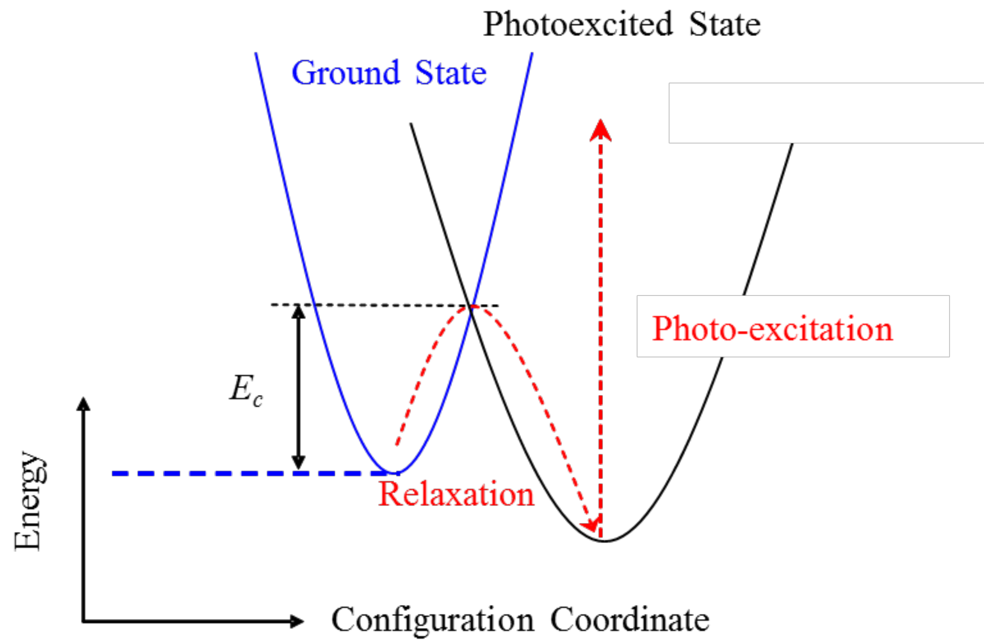


**Figure 3.1** Large-lattice relaxation model for persistent photoconductivity. An energy barrier, $E_c$, hinders the relaxation of the photoexcited state to the ground state.

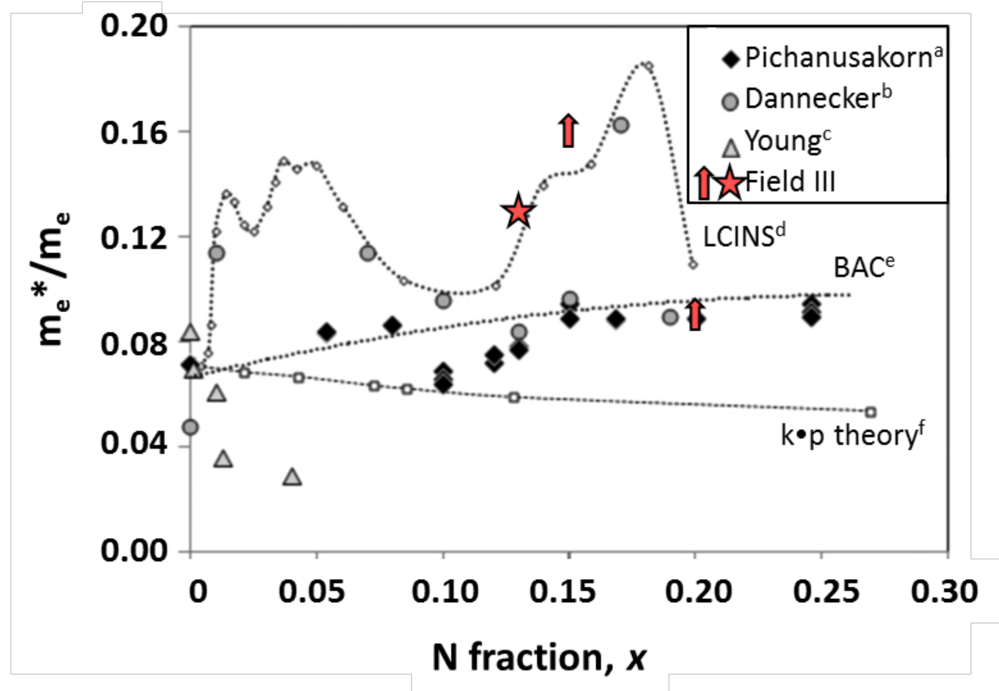


**Figure 3.2** Electron effective mass, $m_e$*, as a function of N fraction, $x$, for GaAsN, determined by various experimental methods and calculations for (a) Si doping, (b) Te doping, and (c) Se doping. Our measured value of $m_e$* (the star symbol) and lower-bounds of $m_e$* (the upward-pointing arrows) for Si-doped GaAsN is consistent with predictions of the LCINS model, which considers N clustering. Reprinted with permission from [a]Ref. 32 (Copyright 2012, American Physical Society). [b]See Ref. 34. [c]See Ref. 29. [d]See Ref. 27. [e]See Ref. 31. [f]See Ref. 62.

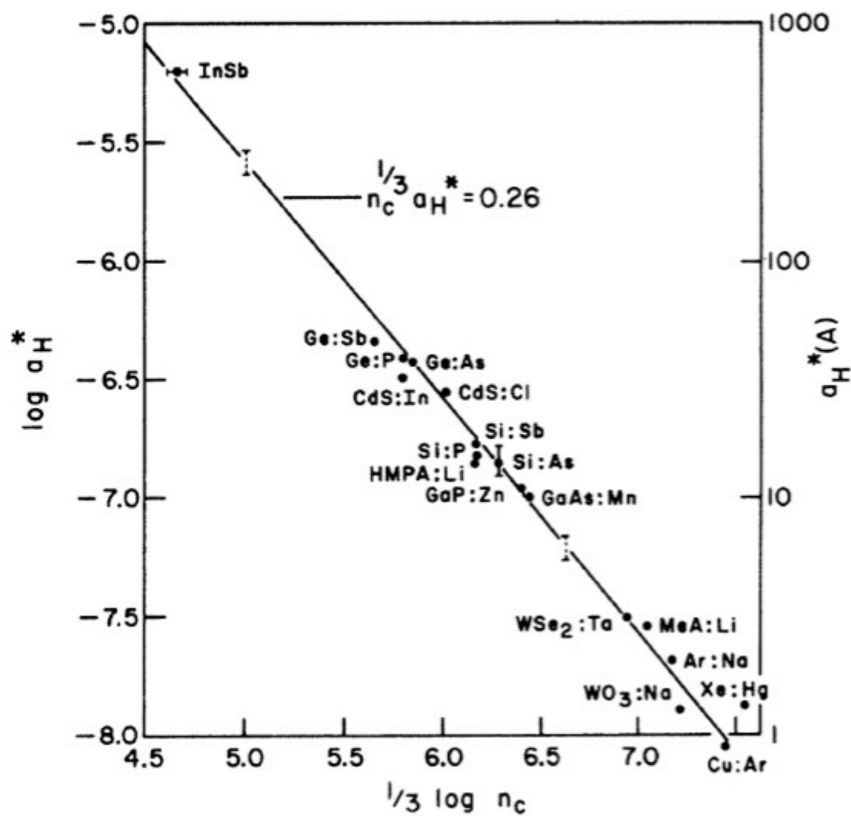


**Figure 3.3** Interdonor distance, $a^*$, vs. critical carrier concentration, $n_c$, for a variety of materials. An interpolation of the data reveals the universality of the Mott criterion, corresponding to the metal-insulator transition. Reprinted with permission from Ref. 35 (Copyright 1978 by the American Physical Society).

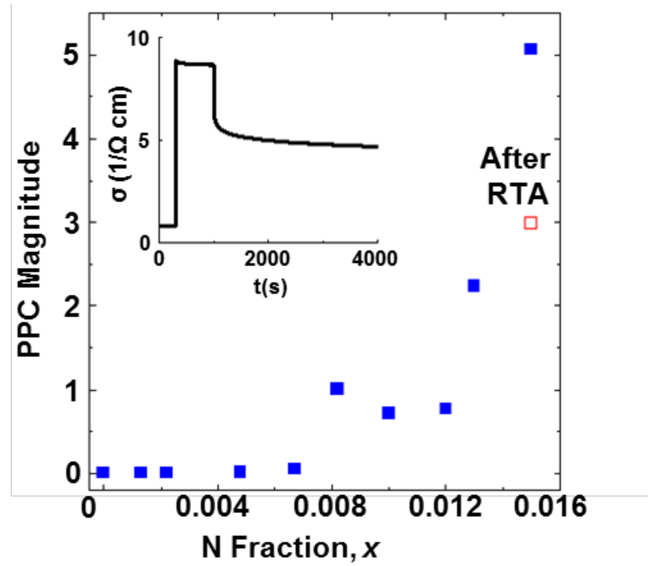


**Figure 3.4** Persistent photoconductivity (PPC) magnitude plotted as a function of N fraction for $GaAs_{1-x}N_x$ films measured at 77 K. Although the PPC effect is negligible for $x < 0.006$, it increases with $x$ for $x > 0.006$. The open square shows the suppression of the PPC magnitude due to rapid-thermal annealing (RTA) at 763 °C on a $GaAs_{0.985}N_{0.015}$ film. The inset shows a typical PPC trace for a $GaAs_{0.985}N_{0.015}$ film, with an illumination duration from $t$ = 300 to 1000 s.

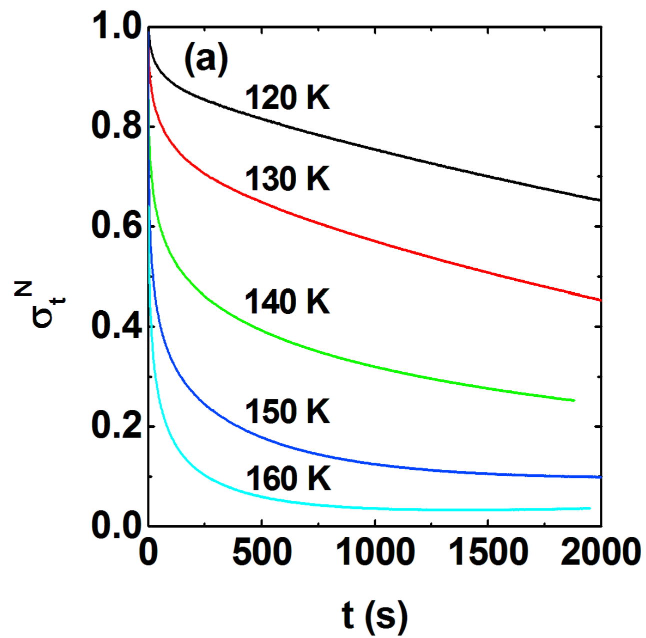


**Figure 3.5a** Examples of persistent photoconductivity data and analysis for a $GaAs_{0.987}N_{0.013}$:Te film. The normalized conductivity, $\sigma_t^N$, with $t$ = 0 defined as the instant of illumination termination, plotted as a function of time and measured at various $T$.

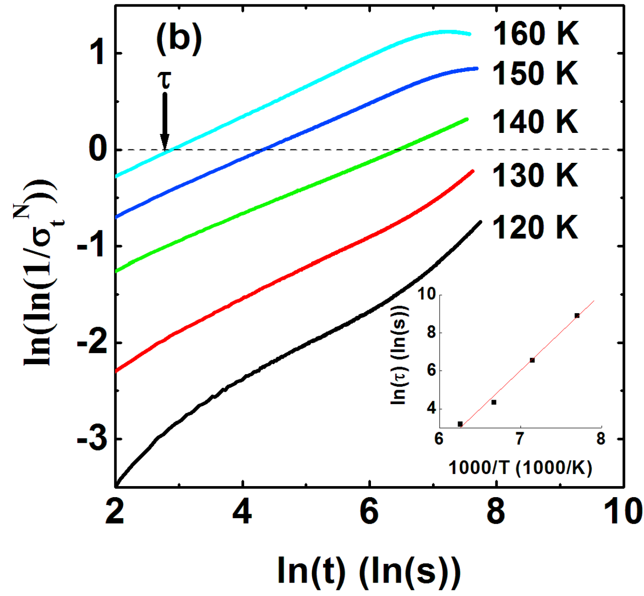


**Figure 3.5b** Examples of persistent photoconductivity data and analysis for a $GaAs_{0.987}N_{0.013}$:Te film. Plot of $\sigma_t^N$ in the form of a stretched-exponential, $\sigma_t^N \propto \exp\left[-\left(\frac{t}{\tau}\right)^{\beta}\right]$, where the *x*-intercept at *y* = 0 is identified as the characteristic decay time, *τ*. The inset shows a plot of ln(*τ*) vs. 1000/*T*, from which the electron-capture energy, $E_c$, is determined.

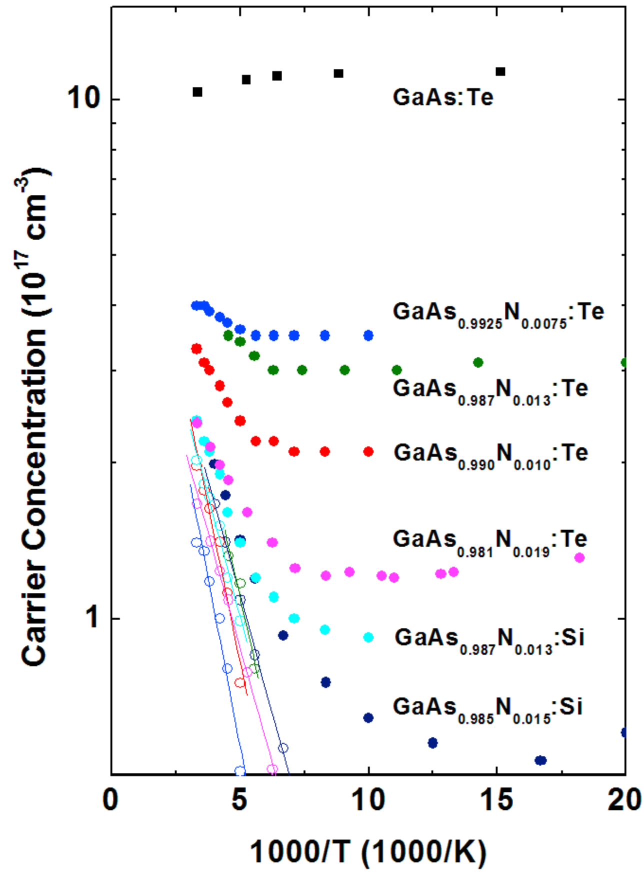


**Figure 3.6** Free carrier concentration, $n$, as a function of $1000/T$ for various GaAsN films in comparison with that of GaAs. For GaAs $n$ is $T$ independent, while for GaAsN two distinct regimes of $n$ are apparent: for high measurement $T$, $n$ increases exponentially with increasing $T$; for low measurement $T$, $n$ is $T$-independent. For $n > n_s$, is also plotted vs. $1000/T$ in open circles. A two-level system formalism is then used to extract the activation energy of N-induced deep donor states, $E_a$.

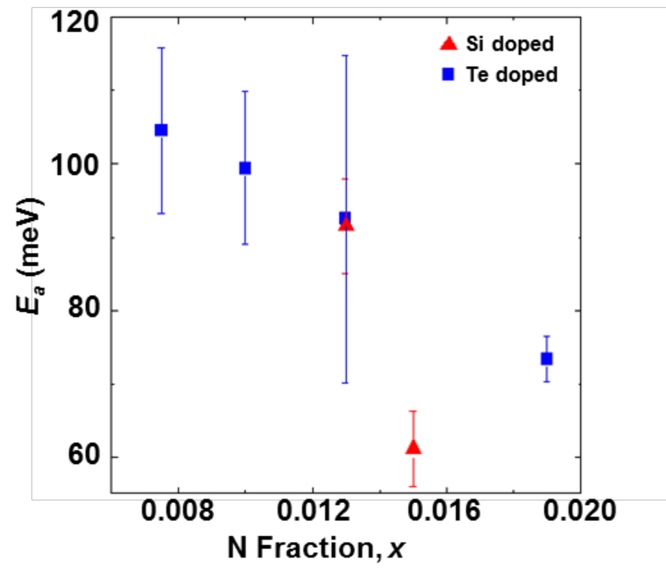


**Figure 3.7** Activation energy, $E_a$, plotted as a function of N fraction, $x$, for $GaAs_{1-x}N_x$ films. The activation energy decreases with increasing $x$, signifying that the N-related deep donor state moves toward the conduction band edge as $x$ increases.

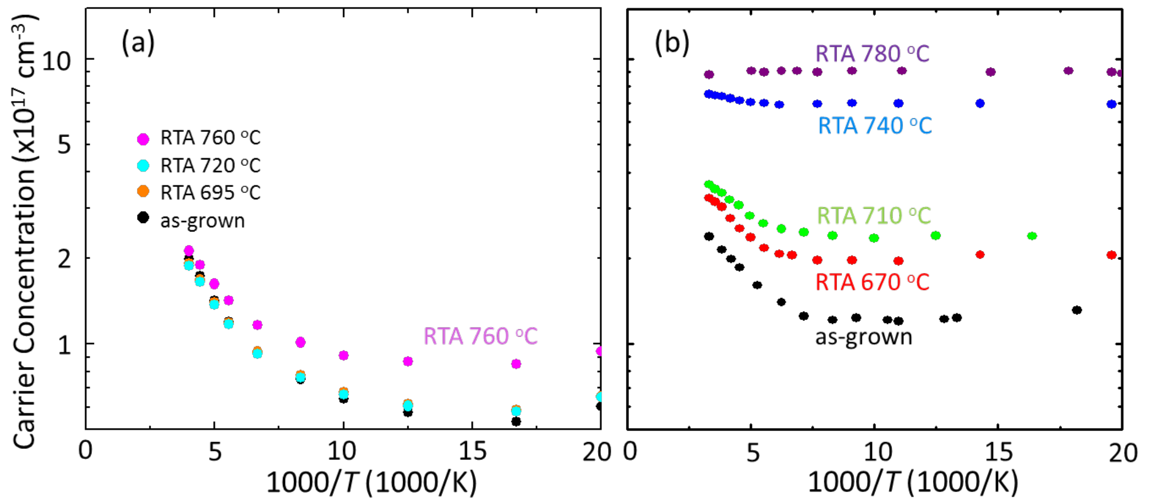


**Figure 3.8** Free carrier concentration, *n*, as a function of $1000/T$, for GaAsN films annealed at various temperatures via rapid-thermal annealing (RTA): (a) a $GaAs_{0.985}N_{0.015}$:Si film, and (b) a $GaAs_{0.984}N_{0.016}$:Te film.

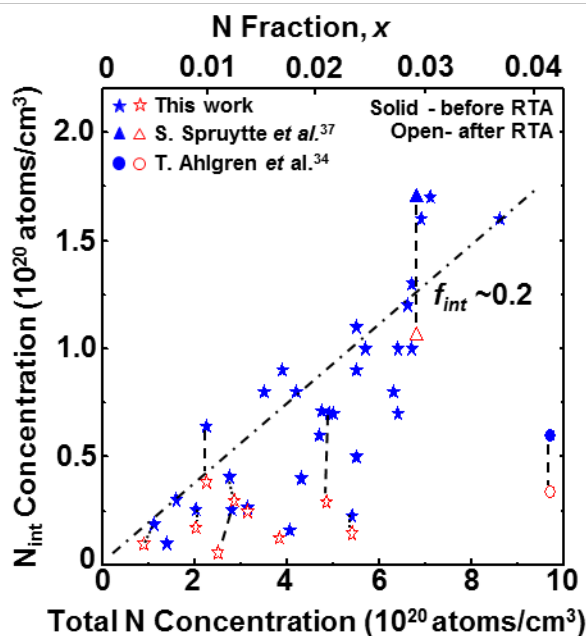


**Figure 3.9** Interstitial N concentration vs. total N concentration for $GaAs_{1-x}N_x$ films with various N fractions, $x$. Linear interpolation of the interstitial N concentration for as-grown films suggests that approximately 20% of N are incorporated interstitially, as indicated in the plot. Following rapid-thermal annealing (RTA), the interstitial N concentration decreases to ~10%, while the total N concentration remains constant to within experimental error. [a]See Ref. 63. [b]See Ref. 57.

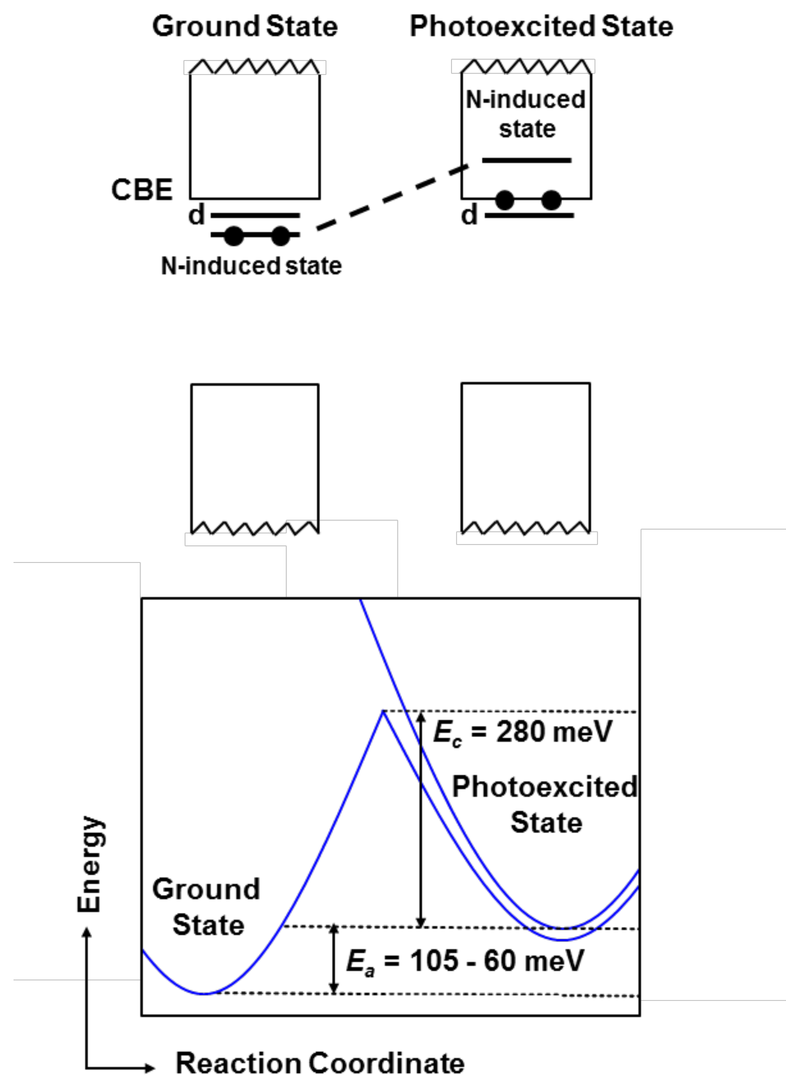


**Figure 3.10** Schematic energy diagram of "ground" (left) and "photoexcited" (right) configurations of GaAsN. Prior to illumination, carriers reside in the ground N-pair [either $(N\text{-}N)_{As}$ or $(N\text{-}As)_{As}$] state. Upon illumination, the carriers are excited from the N-pair state to the conduction-band edge (CBE), leading to enhanced conductivity. Carrier photoexcitation leads to a re-arrangement of the N-pair molecular bonds, with the photoexcited N-pair state at a higher energy than that of the ground N-pair state, namely above the CBE. In order for carriers to return to the ground N-pair state (resulting in a decay of the conductivity with respect to its pre-illumination value), the ground N-pair state configuration must be restored by overcoming the electron-capture barrier, $E_c$.

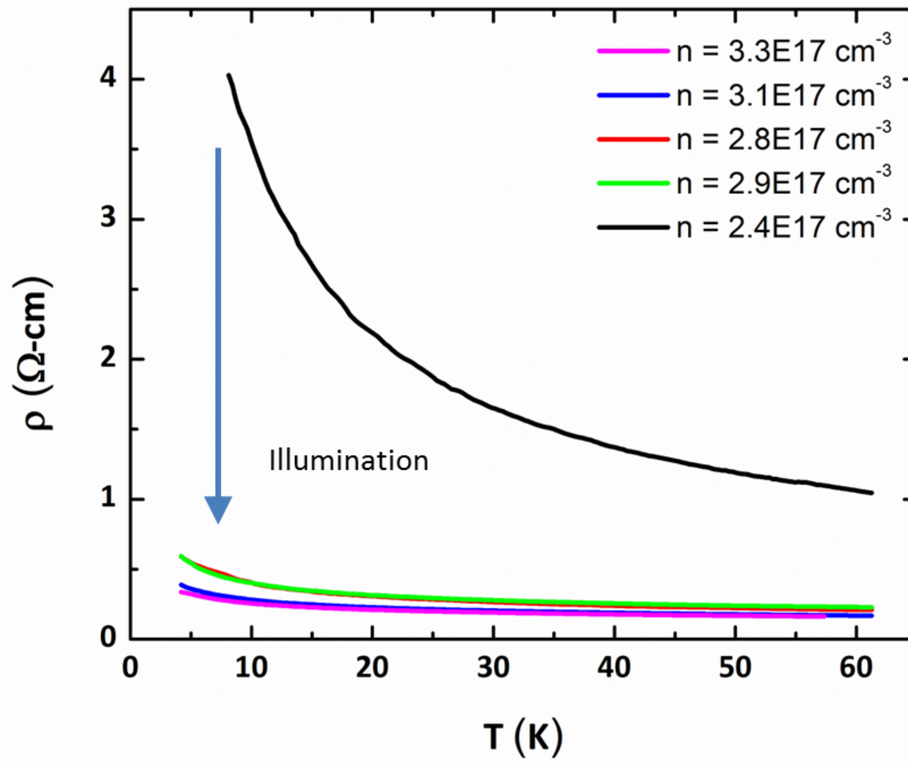


**Figure 3.11** Resistivity, $\rho$, as a function of temperature, $T$, for a $GaAs_{0.987}N_{0.013}$:Si film. Illuminating the film induces persistent photoconductivity, thereby increasing $n$ of the film from 2.4 x $10^{17}$ to 3.3 x $10^{17}$ at saturation of the PPC effect.

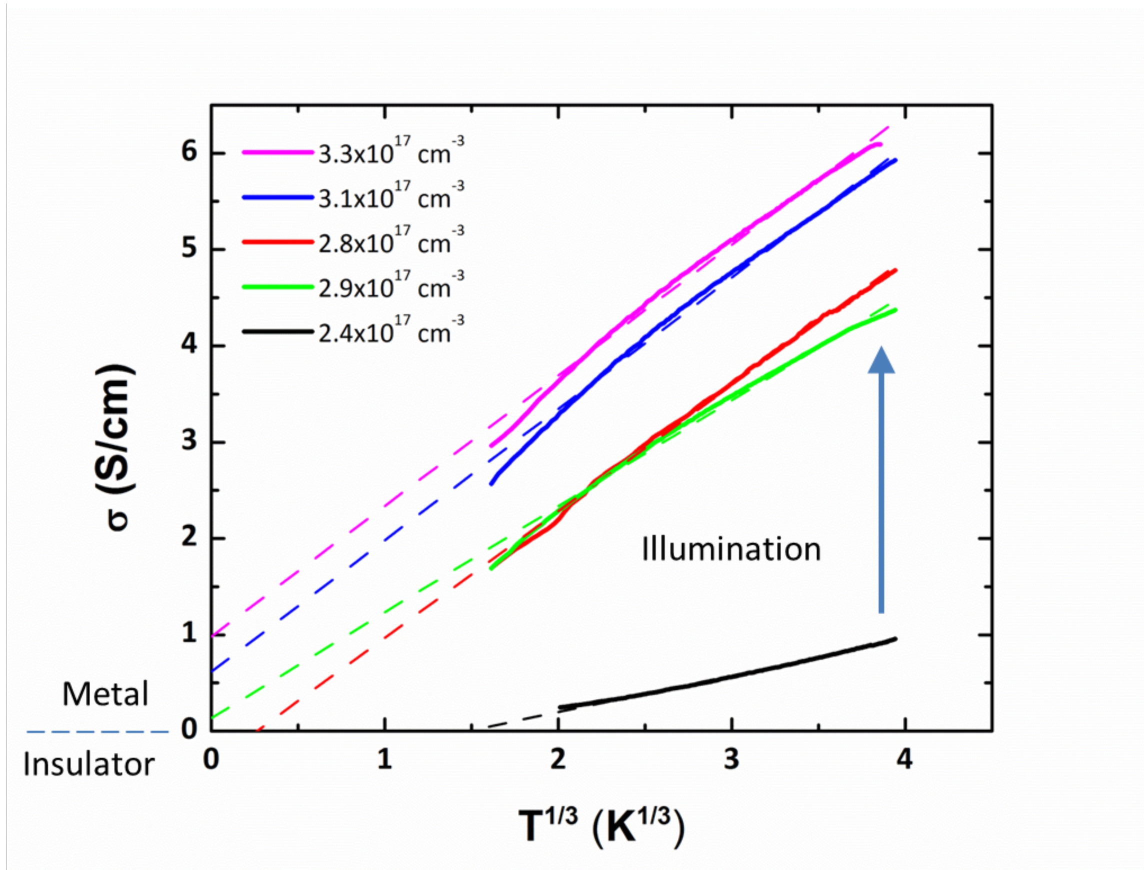


**Figure 3.12** Conductivity, σ, vs. $T^{1/3}$, for a $GaAs_{0.987}N_{0.013}$:Si film. Illuminating the film induces persistent photoconductivity, thereby increasing *n* of the film from 2.4 x $10^{17}$ to 3.3 x $10^{17}$ at saturation of the PPC effect. For each illumination, $\sigma_{min}$ is determined from the *y*-intercept in the plot of σ vs. $T^{1/3}$.

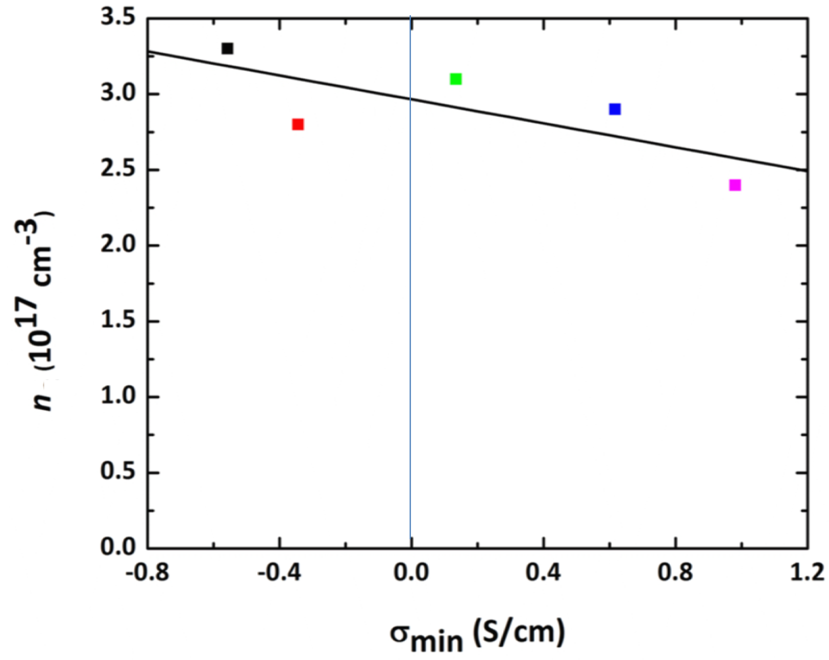


**Figure 3.13** Carrier concentration, $n$, vs. residual conductivity, $\sigma_{min}$, for a $GaAs_{0.987}N_{0.013}$:Si film, where $n$ was varied using the persistent photoconductivity effect. To determine $n_c$, we take a linear interpolation of $n$ vs. $\sigma_{min}$ for all of the illuminations; then, $n = n_c$ when $\sigma_{min} = 0$.

### 3.8 Reference

[1] M. G. Craford, G. E. Stillman, J. A. Rossi, and N. Holonyak, Phys. Rev. B 168, 867 (1968).

[2] D. V. Lang and R. A. Logan, Phys. Rev. Lett. 39, 635 (1977).

[3] D. V. Lang, R. A. Logan, and M. Jaros, Phys. Rev. B 19, 1015 (1979).

[4] J. C. Phillips, Rep. Prog. Phys. 59, 1133 (1996).

[5] E. F. Schubert and K. Ploog, Phys. Rev. B 30, 7021 (1984).

[6] D. J. Chadi and K. J. Chang, Phys. Rev. B 39, 10063 (1989).

[7] S. H. Hsu, Y. K. Su, R. W. Chuang, S. J. Chang, W. C. Chen, and W. R. Chen, Jpn. J. Appl. Phys., Part 1 44, 2454 (2005).

[8] S. H. Hsu, W. R. Chen, Y. K. Su, R. W. Chuang, S. J. Chang, and W. C. Chen, J. Cryst. Growth 290, 87 (2006).

[9] J. Z. Li, J. Y. Lin, H. X. Jiang, J. F. Geisz, and S. R. Kurtz, Appl. Phys. Lett. 75, 1899 (1999).

[10] Y. Jin, Y. He, H. Cheng, R. M. Jock, T. Dannecker, M. Reason, A. M. Mintairov, C. Kurdak, J. L. Merz, and R. S. Goldman, Appl. Phys. Lett. 95, 092109 (2009).

[11] Y. Jin, R. M. Jock, H. Cheng, Y. He, A. M. Mintarov, Y. Wang, C. Kurdak, J. L. Merz, and R. S. Goldman, Appl. Phys. Lett. 95, 062109 (2009).

[12] P. R. C. Kent and Alex Zunger, Phys. Rev. B 64, 115208 (2001).

[13] P. R. C. Kent and Alex Zunger, Appl. Phys. Lett. 82, 559 (2003).

[14] S. Fahy, A. Lindsay, H. Ouerdane, and E. P. O'Reilly, Phys. Rev. B 74, 035203 (2006).

[15] Yong Zhang, A. Mascarenhas, H. P. Xin, and C. W. Tu, Phys. Rev. B 61, 7479 (2000).

[16] P. J. Klar, H. Gruning, W. Heimbrodt, J. Koch, F. Hohnsdorf, W. Stolz, P. M. A. Vicente, and J. Camassel, Appl. Phys. Lett. 76, 3439 (2000).

[17] R. Kudrawiec, M. Latkowska, M. Welna, J. Misiewicz, M. Shafi, R. H. Mari,M. Henini, and W.Walukiewicz, Appl. Phys. Lett. 101, 082109 (2012).

[18] K. Alberi, B. Fluegel, D.A. Beaton, A. J. Ptak, and A. Mascarenhas, Phys. Rev. B 86, 041201 (2012).

[19] Clas Persson and Alex Zunger, Phys. Rev. B 68, 035212 (2003).

[20] L. Ivanova, H. Eisele, M. P. Vaughan, Ph. Ebert, A. Lenz, R. Timm, O. Schumann, L. Geelhaar, M. Dahne, S. Fahy, H. Riechert, and E. P. O'Reilly, Phys. Rev. B 82, 161201 (2010).

[21] Yong Zhang, A. Mascarenhas, J. F. Geisz, H. P. Xin, and C. W. Tu, Phys. Rev. B 63, 085205 (2001).

[22] A. Patane, J. Endicott, J. Ibanez, P. N. Brunkov, L. Eaves, S. B. Healy, A. Lindsay, E. P. O'Reilly, and M. Hopkinson, Phys. Rev. B 71, 195307 (2005).

[23] A. Grau, T. Passow, and M. Hetterich, Appl. Phys. Lett. 89, 202105 (2006).

[24] J. D. Perkins, A. Mascarenhas, Yong Zhang, J. F. Geisz, D. J. Friedman, J. M. Olson, and S. R. Kurtz, Phys. Rev. Lett. 82, 3312 (1999).

[25] X. Liu, M.-E. Pistol, and L. Samuelson, Phys. Rev. B 42, 7504 (1990).

[26] Xiao Liu, M.-E. Pistol, L. Samuelson, S. Schwetlick, and W. Seifert, Appl. Phys. Lett. 56, 1451 (1990).

[27] F. Masia, G. Pettinari, A. Polimeni, M. Felici, A. Miriametro, M. Capizzi, A. Lindsay, S.B. Healy, E.P. O'Reilly, A. Cristofoli, G. Bais, M. Piccin, S. Rubini, F. Marelli, A. Franciosi, PlJ. Klar, K. Volz, and W. Stolz, Phys. Rev. B 73, 073201 (2006).

[28] J. Ibanez, R. Cusco, E. Alarcon-Llado, L. Artus, A. Patane, D. Fowler, L. Eaves, K. Uesugi, and I. Suemune, J. Appl. Phys. 103, 103528 (2008).

[29] D.L. Young, J.F. Geisz, and T.J. Coutts, Appl. Phys. Lett. 82, 1236 (2003).

[30] A. Lindsay and E.P. O'Reilly, Phys. Rev. Lett. 93, 196402 (2004).

[31] W. Shan, W. Walukiewicz, J.W. Ager, E.E. Haller, J.F. Geisz, D.J. Friedman, J.M. Olson, and S.R. Kurtz, Phys. Rev. Lett. 82, 1221 (1999).

[32] P. Pichanusakorn, Y. J. Kuang, C. Patel, C. W. Tu, and P. R. Bandaru, Phys. Rev. B 86, 085314 (2012).

[33] A. Lindsay and E. P. O'Reilly, Phys. Rev. Lett. 93, 196402 (2004).

[34] T. Dannecker, Y. Jin, H. Cheng, C.F. Gorman, J. Beckeridge, C. Uher, S. Fahy, C. Kurdak, and R.S. Goldman, Phys. Rev. B 82, 125203 (2010).

[35] P.P. Edwards and M.J. Sienko, Phys. Rev. B, 2375 (1978).

[36] N.F. Mott, Philos. Mag. 26, 1015 (1972).

[37] B.L. Al'tshuler and A.G. Aronov, JETP Lett. 37, 411 (1983).

[38] T. Ohtsuki and T. Kawarabayash, J. Phys. Soc. Japan 66, 314 (1997).

[39] M. Watanabe, Y. Ootuka, K.M. Itoh, and EE. Haller, Phys. Rev. B 58, 9851 (1998).

[40] T. Tshepe, C. Kasl, J.F. Prins, and M.J.R. Hoch, Phys. Rev. B 70, 245107 (2004).

[41] M.C. Maliepard, M. Pepper, R. Newbury, and G. Hill, Phys. Rev. Lett. 61, 369 (1988).

[42] V.M. Teplinski, V.F. Gantmakher, and O.I. Barkalov, Sov. Phys. JETP 74, 905 (1992).

[43] V.F. Gantmakher, V.N. Zverev, V.M. Teplinski, and O.I. Barkaliov, JETP 76, 714 (1993).

[44] Y. Imry and Z. Ovadyahu, Phys. Rev. Lett. 49, 841 (1982).

[45] I. Shlimak, phys. stat. sol. (b) 205, 287 (1998).

[46] M. Reason, H. A. McKay, W. Ye, S. Hanson, R. S. Goldman, and V. Rotberg, Appl. Phys. Lett. 85, 1692 (2004).

[47] M. Reason, N. G. Rudawski, H. A. McKay, X. Weng, W. Ye, and R. S. Goldman, J. Appl. Phys. 101, 083520 (2007).

[48] W. Ye, S. Hanson, M. Reason, X.Weng, and R. S. Goldman, J. Vac. Sci. Technol. B 23, 1736 (2005).

[49] Y. Jin, Ph.D. Thesis, Ch. 2, University of Michigan, Ann Arbor, 2010.

[50] D. Henning and H. Thomas, Solid-State Electron. 25, 325 (1982).

[51] D. V. Lang and R. A. Logan, in Physics of Semiconductors 1978 (Inst. Physics, London, UK, 1979), pp. 433–436.

[52] H. P. Xin, K. L. Kavanagh, Z. Q. Zhu, and C. W. Tu, Appl. Phys. Lett. 74, 2337 (1999).

[53] H. P. Xin, K. L. Kavanagh, Z. Q. Zhu, and C. W. Tu, J. Vac. Sci. Technol. B 17, 1649 (1999).

[54] H. Ikoma, J. Phys. Soc. Jpn 28, 1474 (1970).

[55] E. F. Schubert, Doping in III-V Semiconductors (Cambridge University Press, Cambridge, UK, 1993) pp. 193–207.

[56] C. M.Wolfe, D. M. Korn, and G. E. Stillman, Appl. Phys. Lett. 24, 78 (1974).

[57] T. Ahlgren, E. Vainonen-Ahlgren, J. Likonen, W. Li, and M. Pessa, Appl. Phys. Lett. 80, 2314 (2002).

[58] S. B. Zhang and S.-H. Wei, Phys. Rev. Lett. 86, 1789 (2001).

[59] L. W. Song, X. D. Zhan, B. W. Benson, and G. D. Watkins, Phys. Rev. Lett. 60, 460 (1988).

[60] T. Dannecker, Ph.D. Thesis, Ch. 4, National University of Ireland, Cork, 2011.

[61] M. Kondow, M. Uchiyama, M. Morifuji, S. Wu, H. Momose, S.Fukushima, A. Fukuyama, and T, Ikari, Appl. Phys. Express 2, 041003 (2009).

[62] U. Katsuhiro, M. Nobuki, and S. Ikuo, Appl. Phys. Lett. 74, 1254 (1999).

[63] S. G. Spruytte, C.W. Coldren, J. S. Harris, W. Wampler, P. Krispin, K. Ploog, and M. C. Larson, J. Appl. Phys. 89, 4401 (2001).

# Chapter 4

# GaAsBi: Growth and Properties

## 4.1 Overview

This chapter describes investigations of the growth mechanisms and electrical properties of GaAsBi alloys. The objective of this work is to gain an understanding of the influence of As species on GaAsBi growth and properties, and also the influence of stoichiometry on the doping type of Si in GaAsBi.

This chapter opens with background information, including a description of the challenges of synthesizing high-quality GaAsBi and a review of Si doping in GaAs. Next, the experimental details for these investigations are described. The bulk of this chapter is devoted to a comparison of $As_2$ and $As_4$ on GaAsBi growth. The influence of As species on the surface morphology will be presented. Then, the influence of the stoichiometry threshold on dopant carrier type will be discussed. Finally, we report on the electrical properties of GaAsBi, including photoluminescence and mobility measurements. We explore the growth-rate dependence of the stoichiometry threshold on the dopant type of Si-doped GaAsBi, and propose a dopant incorporation mechanism based upon the growth-rate dependence of the stoichiometry threshold for GaAsBi.

## 4.2 Background

### 4.2.1 Growth of GaAsBi alloys

GaAsBi alloys were first grown by metal-organic vapor phase epitaxy (MOVPE) in 1998,[1] and then by molecular-beam epitaxy (MBE) in 2003.[2] MOVPE introduces higher levels of carbon and hydrogen contamination than MBE, due to the use of metal-organic precursors for Ga and/or As.[3] Furthermore, MBE has yielded higher-performing devices than MOVPE, such as (In)GaAsN lasers,[4-7] making MBE a promising method of synthesizing GaAsBi alloys.

Due to the large size of Bi and its tendency to surface segregate, MBE of GaAsBi alloys requires non-standard growth conditions in comparison to conventional MBE of III-V alloys.[2,8] Firstly, low-temperature growth is necessary to avoid desorption of Bi due to the limited miscibility of Bi in GaAs.[9] Subsequently, growth temperatures from 280-400 °C are used, with Bi incorporation increasing as growth temperature decreases.[10] In addition, GaAsBi alloys are typically grown using $As_2$, for which Group V/III beam-equivalent pressure (BEP) ratios at or below stoichiometry—i.e., the transition from Group-V-rich to Group-III-rich conditions—are necessary for Bi to incorporate. This implies that either As outcompetes Bi for Group V sites at conventional Group V/III BEP ratios, or that As incorporation is energetically favorable. Furthermore, a growth-rate dependence of the stoichiometry threshold has been reported.[11] In addition, Ga-rich growth produces Ga-based surface droplets, due to excess Ga at low Group V/III BEP ratios. At high Bi fluxes, Bi may collect on droplets to form Ga-Bi composite droplets,[11] due to the immiscibility of Ga and

Bi.[9] Indeed, precise control of growth conditions is necessary to synthesize high-quality GaAsBi films without surface droplets.

### 4.2.2 Si doping type in GaAs

Silicon has been reported to act as both a donor and acceptor in GaAs and related alloys.[12] During MBE of (001) GaAs, silicon typically occupies a Ga lattice site, $Si_{Ga}$, resulting in *n*-type doping.[12] It is hypothesized that Si occupation of As sites, i.e. $Si_{As}$, enables *p*-type doping of GaAs:Si. Indeed, $Si_{As}$ formation is favored when the competition for As site occupancy is reduced by the use of low As fluxes or high substrate temperatures (which enhance As desorption).[12,14] For example, *p*-type doping of GaAs:Si has been obtained with MBE on (110) or (*n*11)A ($n \leq 3$) GaAs surfaces using low Group V/III flux ratios and/or high substrate temperatures.[12-22] For (001) GaAs, *p*-type doping with Si has been obtained using a shuttered deposition sequence where Si and Ga are alternated with As,[23,24] or using low Group V/III flux ratios with low growth temperatures.[25]

## 4.3 Experimental details

$GaAs_{1-y}Bi_y$:(Si) alloy films were grown on semi-insulating (001) GaAs substrates by MBE, using solid Ga, $As_2$ or $As_4$, Bi, and Si sources. GaAsBi:(Si) films grown using $As_2$ were grown in the GENII MBE system, and the surface reconstructions were monitored *in-situ* with a reflection high-energy electron diffraction (RHEED) source operating at 18 keV. For all films, the substrate temperature was measured by a thermocouple in contact with the back of each molybdenum block, calibrated by setting the oxide temperature equal to 580 °C.

Subsequently, a 520-nm thick GaAs buffer was grown at 580 °C at 1 μm/hr with a (2 x 4) RHEED pattern. Next, the growth was interrupted and the substrate temperature was lowered to the growth temperature (315 to 350 °C). Subsequently, 30-300 nm GaAs(Bi):(Si) layers were grown at various growth rates (0.1 to 0.85 μm/hr), Group V/III BEP ratios (2.5 to 10), and Bi:Ga BEP ratios (0 to 0.1).

GaAsBi:(Si) films grown using $As_4$ were grown in the Compact 21 MBE system, and the surface reconstructions were monitored *in-situ* with a RHEED source operating at 12 keV. For all films, the substrate temperature was measured by a thermocouple in contact with the back of each molybdenum block, calibrated by setting the oxide desorption temperature equal to 600 °C. Subsequently, a 500-nm thick GaAs buffer was grown at 600 °C at 1.2 μm/hr with a (2 x 4) RHEED pattern. Next, the substrate temperature was lowered to 280 °C and 250- to 550-nm thick GaAs was grown with a (2 x 3) surface reconstruction. Finally, 400-nm GaAs(Bi):(Si) layers were grown at various growth rates (0.25 to 2.0 μm/hr), Group V/III BEP ratios (6 to 20), and Bi:Ga BEP ratios (0 to 0.6).

For the GaAs(Bi):(Si) alloys, the surface morphology was examined *ex-situ* with atomic force microscopy (AFM). The in-plane and out-of-plane strain and lattice parameters were determined from an analysis of (004) and (224) high-resolution X-ray rocking curves (HRXRC), in both $\varphi = 0°$ and $\varphi = 180°$ configurations. We note that the HRXRCs were performed in a Bede $D^1$ system, with a monochromator which contains two Si channel cut crystals, consisting of (220) reflections in the duMond-Hart-Bartels (+,-,-,+) configuration, which select the $CuK\alpha_1$ line with a beam divergence of 12 arcseconds.[26,27] To determine the Bi fraction, *y*, we use a linear interpolation of the measured GaAs (5.6533 Å) and calculated GaBi (6.33 Å) lattice parameters,[28] along with a Poisson's ratio of 0.33. In many cases, *y* was also determined using Rutherford backscattering spectroscopy (RBS) measurements in

conjunction with simulation of nuclear reaction analysis code (SIMNRA); the HRXRC and RBS determinations of $y$ agree to within 16%. For all the GaAs(Bi):Si films, resistivity and Hall measurements were performed at room temperature using the van der Pauw method. The composition profiles across the surface droplets were determined using energy dispersive X-ray spectroscopy (EDX) and/or Auger electron spectroscopy, in respective scanning electron microscopes (SEM). Finally, for select films, surface Ga droplets were removed via surface etching with HCl:$H_2O$ (1:3),[29,30] followed by subsequent AFM, EDX, and resistivity and Hall measurements.

### 4.4 Growth of GaAsBi

#### 4.4.1 Influence of arsenic species on the growth of GaAsBi alloys

We now consider the surface morphology of the GaAs(Bi):(Si) films grown with $As_2$ and $As_4$, captured in the SEM, EDX, and AFM images in Fig. 4.1. As shown in the SEM images in Figs. 4.1(a) and 4.1(b) [Figs. 4.1(c) and 4.1(d)] for films grown with $As_2$ [$As_4$], films grown in As-rich conditions are smooth and droplet free, while Ga-rich growth leads to surface droplets. The corresponding EDX images, with red, green, and blue representing Ga, As, and Bi, respectively, are shown in Figs. 4.1(e) and 4.1(f) [Figs. 4.1(g) and 4.1(h)] for GaAsBi films grown with $As_2$ [$As_4$]. For growth using either $As_2$ or $As_4$, the speckled green-red color for As-rich growth suggests the formation of a uniform GaAsBi film. On the other hand, for Ga-rich growth, red or red-blue spots are observed on top of the speckled green-red color, indicating the presence of Ga-rich surface droplets, which often contain segregated patches of Bi. Similarly, for growth using $As_2$ [Figs. 4.1(i) and 4.1(j)] or $As_4$ [Figs. 4.1(k)

and 4.1(l)], AFM reveals the presence of droplets for Ga-rich growth, and smooth films for As-rich growth. Indeed, As-rich growth is favorable for creating smooth, droplet-free films.

In Fig. 4.2, we consider Bi incorporation into GaAs, as a function of growth rate and Group V/III BEP ratio, for various GaAs(Bi) films grown using either $As_2$ or $As_4$. The solid line separates films grown with $As_2$ and $As_4$, with films grown using $As_2$ in the lower-left-hand corner of the plot. All films were exposed to As, Ga and Bi flux; thus, the plot indicates if Bi was successfully incorporated into GaAs to form GaAsBi (solid symbols), or if Bi failed to incorporate into GaAs (open symbols). For films grown using $As_2$, a dashed line separates films with Bi incorporation from films without Bi incorporation, with Bi incorporation for Group V/III BEP ratios $\leq 6$. This dashed line corresponds to the stoichiometry threshold separating Ga-rich growth from As-rich growth, as identified by a transition from a spotty (1x1) to streaky (2x1) RHEED pattern.[31] Thus, for growth using $As_2$, Ga-rich (As-rich) growth causes Bi to incorporate (not incorporate), producing GaAsBi (GaAs) films. In the case of growth using $As_4$, Bi incorporation is much more successful, over a wide range of Group V/III BEP ratios (6 to 20) and growth rates (0.25 to 2.0 μm/hr). Thus, growth using $As_4$ is favorable due to the ability to incorporate Bi into GaAs in As-rich conditions, which yields smooth, droplet-free GaAsBi films.

To understand why growth of GaAsBi is favorable when using $As_4$, we now consider Bi incorporation mechanisms for films grown with $As_2$ and $As_4$, as shown in Fig. 4.3. Here, we show the surface reconstruction and consider if the active As species can favorably replace Bi dimers on the growth surface. During growth using $As_2$, surface $Bi_2$ can be replaced by $As_2$.[32] This swapping mechanism is enhanced at high Group V/III BEP ratios due to an increased As BEP; thus, low Group V/III BEP ratios are necessary for Bi to incorporate. In contrast, during growth using $As_4$, two $As_4$ interact at the surface, each

breaking into 2 $As_2$ and incorporating one $As_2$ pair while releasing the other $As_2$ pair. Thus, not every $As_4$ that interacts with the growth surface will be incorporated, reducing the amount of As contributing to swapping at high As BEP. Furthermore, it has been reported that for $As_4$ to replace $Bi_2$, two adjacent $Bi_2$ must be dislodged by two $As_4$, further increasing the likelihood of Bi incorporation.[33]

### 4.4.2 Influence of stoichiometry threshold on carrier type

We now consider GaAsBi growth using $As_4$. To monitor the stoichiometry threshold, RHEED patterns were collected along the [110] and $[1\bar{1}0]$ directions, as shown in Figure 4.4. During GaAs growth at 600 °C, a streaky (2 x 4) RHEED pattern is observed, indicating Group V termination of the surface [Figs. 4.4 (a) and 4.4(b)]. As the substrate temperature is lowered to 280 °C, the RHEED pattern transforms to a streaky (2 x 3) pattern [Figs. 4.4(c) and 4.4(d)], independent of the presence of Si. In the Ga-rich regime, GaAs(Bi):(Si) growth results in the emergence of spotty (2 x chevron) RHEED patterns [Figs. 4.4(e) and 4.4(f)], indicating a (2 x 1) surface reconstruction. For the As-rich regime, within 10 s of GaAs(Bi):(Si) growth, streaky ($n$ x 3) patterns [Figs. 4.4(g) and 4.4(h)] appear ($n \leq 2$), with (2 x chevron) patterns often emerging following at least 45 s of growth. A similar transition to a spotty (2 x 1) surface reconstruction at the stoichiometry threshold has been reported for GaAsBi growth using $As_2$.[34]

The carrier types and concentrations (x$10^{18}$ $cm^{-3}$) for GaAs(Bi):Si films are summarized in Fig. 4.5, in the plot of As BEP vs. Ga BEP, with growth rate shown on the upper $x$-axis. We note that the growth rate $x$-axis applies to data in the As-rich growth regime. Carrier densities are listed for films grown with a Si effusion cell temperature of 1250 °C. A

dotted line indicates the regime where the Group V/III BEP ratio is equal to 10, "BEPratio10", essentially separating the As-rich and Ga-rich growth regimes. All GaAs(Bi):Si films above (below) the BEPratio10 line are *n*-type (*p*-type). In addition, along the BEPratio10 line, there is a carrier-type conversion from *n*-type to *p*-type as the growth rate increases (from 0.25 to 2.0 μm/hr), consistent with the growth rate dependence of the stoichiometry threshold reported in Ref. 31. Interestingly, the *p*-type (*n*-type) films were grown in the Ga-rich [As-rich] growth regimes, where (2x1) [(*n* x 3)] surface reconstructions were observed. As shown in Fig. 4.6, the (2 x 1) reconstructed surfaces have significantly more Group V sites per unit area than the (*n* x 3) reconstructed surfaces;[35-37] thus, Si atoms may more effectively incorporate into Group V sites, yielding *p*-type behavior. Furthermore, for growth at low Group V/III BEP ratios, Si has less competition with As and Bi for Group V site occupancy, resulting in *p*-type GaAs(Bi):Si films. However, at low growth rates, Si atoms may have time to migrate to Ga sites prior to their incorporation,[38] thereby yielding *n*-type GaAs(Bi):Si films. This is consistent with previous reports showing a conversion from *n*-type to *p*-type behavior for GaAs:Si grown under Ga-stable conditions.[39] Although the carrier concentrations of the *n*-type films decrease as the Ga-stable growth conditions are approached, further investigations of the growth-rate dependence of the carrier density and type along additional lines of constant V/III BEP ratio are suggested.

### 4.4.3 Carrier type-microstructure correlations

In Fig. 4.7(a), the in-plane ($a_{//}$) and perpendicular ($a_{\perp}$) lattice parameters, as a function of $y$, are shown for GaAsBi films with and without Si doping. For $y < 0.04$, $a_{//}$ remains

constant, while $a_\perp$ increases linearly with $y$. Presumably Bi incorporation into GaAs increases $a_\perp$ of the film, while the unit cell volume remains nearly constant (i.e. the film is pseudomorphically strained). For $y > 0.04$, $a_{/\!/}$ begins to increase while $a_\perp$ remains nearly constant, suggesting that the film lattice has begun to relax to its intrinsic lattice parameter. Furthermore, both $a_{/\!/}$ and $a_\perp$ are independent of Si doping type and concentration; thus, there is no apparent correlation between Si doping type and any excess As incorporation.

To further consider the influence of Si on the structure of GaAsBi:Si films, we plot the FWHM of the GaAsBi peak from (004) HRXRCs as a function of $y$ for undoped GaAsBi, as well as for *n*-type and *p*-type GaAsBi:Si films [Fig. 4.7(b)]. Furthermore, the HRXRCs for undoped GaAsBi films are shown in Fig. 4.8. For undoped GaAsBi and *n*-type GaAsBi:Si with $y < 0.04$, the FWHM of the GaAsBi peak is typically 40 to 55 arcseconds, and Pendellosung fringes are apparent, indicating smooth epilayer surfaces and interfaces. However, for $y > 0.04$, Pendellosung fringes are not apparent, presumably due to roughening of the surfaces and interfaces due to misfit strain relaxation. Furthermore, the FWHM of the GaAsBi peak increases to 400 – 600 arcseconds, due to the relaxation of misfit strain, as mentioned above, and/or due to inhomogeneous Bi incorporation.[40] Assuming a Gaussian distribution of misoriented blocks,[41] the FWHM would correspond to dislocation densities increasing from $\sim 10^7$ to $\sim 10^9$ cm$^{-2}$. For *p*-type GaAsBi:Si films, Pendellosung fringes are not apparent, and the FWHM of the GaAsBi peak increases with $y$, similarly suggesting roughening of the epilayer surfaces and interfaces due to misfit strain relaxation and/or inhomogeneous Bi incorporation.

## 4.5 Optical and electrical properties of GaAsBi alloys

### 4.5.1 Photoluminescence of GaAsBi films

GaAsBi alloys are promising due to the significant bandgap reduction with increasing Bi fraction. Therefore, we performed low-$T$ photoluminescence (PL) on GaAsBi to consider the influence of arsenic species on the bandgap reduction. Often, the bandgap, $E_g$, is extracted from the $T$-dependence of the PL peak emission, using the Varshni equation:

$$E_g(T) = E_g(0) - \frac{\alpha T^2}{T + \beta} \ , \qquad (4.1)$$

where $\alpha$ and $\beta$ are material constants. However, the $T$-dependences of many of the measured GaAsBi films do not follow the Varshni equation; thus, the true bandgap cannot be directly extracted. Therefore, we consider the reduction of the PL peak energy at 10 K, since the PL peak energy is approximately equal to the bandgap at low-$T$. In Fig. 4.9, we plot the 10-K PL peak energy as a function of $y$ for films grown with $As_2$ and $As_4$. The inset shows a typical PL trace for a $GaAs_{0.969}Bi_{0.031}$:Si film. The uncertainty of the PL peak energy is taken as one standard deviation, giving a 68% confidence interval. Interestingly, there is a similar energy decrease per percent Bi fraction, $\Delta E/y$, for films grown with $As_2$ vs. $As_4$. Therefore, we take a weighted fit of the PL peak energies for all our GaAsBi films (grown with $As_2$ and $As_4$), revealing that $\Delta E/y$ = 60 meV. This is similar to, but slightly lower than, the literature value of $\Delta E/y$ = 88 meV reported by Francoeur.[42]

### 4.5.2 Influence of droplets on electrical properties

We now consider the influence of droplets on the electrical properties of GaAsBi:Si films, captured in the SEM, EDX, and AFM images in Fig. 4.10. As shown in the SEM and AFM images in Figs. 4.10(a) and 4.10(b), the *n*-type GaAsBi films are smooth and droplet free, while the *p*-type films contain sub-micron-diameter surface droplets. The corresponding EDX images, with red, green, and blue representing Ga, As, and Bi, respectively, are shown in Figs. 4.10(d) and 4.10(e) for *n*-type and *p*-type GaAsBi films. For the *n*-type film, the speckled green-red color in Fig. 4.10(d) suggests the formation of a uniform GaAsBi film. On the other hand, for the *p*-type film, red spots are observed on top of the speckled green-red color, indicating the presence of Ga-rich surface droplets, often containing segregated patches of Bi, consistent with similar 2D EDX mapping of GaAsBi films.[31] Droplets presumably begin to form at the start of GaAsBi:Si growth and gradually develop, leading to both the appearance of chevrons and a dimming of the RHEED pattern, similar to earlier reports of island growth.[43,44] AFM reveals that droplets are displaced from 20 ± 10 nm deep craters [circled in Fig. 4.10(h)], similar to earlier reports of Ga droplets deposited at 350 °C.[45] Following droplet removal, the *p*-type GaAsBi surface contains craters, as shown in Fig. 4.10(c). The absence of red spots in the corresponding EDX image in Fig. 4.10(f) confirms the absence of Ga-rich regions within the craters. We note that the craters are observed both before and after etching, as shown in the AFM images in Figs. 4.10(h) and 4.10(i). Cuts of the tip height (line-cuts) across the AFM images reveal 20 ± 10 nm craters in both cases. Furthermore, for the *p*-type GaAsBi:Si films shown in Fig. 4.10, the carrier concentration is $2.1 \pm 0.2 \times 10^{18}$ $cm^{-3}$, the hole mobility is $29.5 \pm 1.5$ $cm^2/(V\text{-}s)$, and the conductivity is 9.8 ± 0.6 S/cm, both before and after etching. The apparent lack of influence

of the Ga surface droplets on the GaAsBi:Si film transport properties suggests that our 20 ± 2% droplet surface coverage is below the percolation threshold for conduction, typically >50%.[46,47]

### 4.5.3 Electrical properties

In Fig. 4.11, we plot conductivity, $\sigma$, as a function of carrier concentration, $n$, for our GaAsBi:Si films, in comparison with Hall data reported in the literature for GaAsBi films with various $n$-type and $p$-type dopants.[48-52] In the plot of $\sigma$ vs. $n$, dashed lines form an envelope corresponding to mobilities of ~2300 and ~45 cm$^2$/(V-s) for $n$-type and $p$-type films, respectively. We demonstrate $n$-type mobilities up to 2500 cm$^2$/(V-s) ($n$ = 8 x 10$^{17}$ cm$^{-3}$), higher than previously reported electron mobilities for GaAsBi.[48,49] For our $n$-type films grown near the stoichiometry threshold, mobilities lie near the mid-range of the envelope. For our $p$-type films with Bi fractions up to 0.05, free carrier concentrations in excess of 5 x 10$^{18}$ cm$^{-3}$ are achieved, a significant increase over literature reports of ~2 x 10$^{18}$ cm$^{-3}$.[50,52] Thus, Si is a promising alternative to C and Be for $p$-type doping of GaAsBi.

In Fig. 4.12, we plot mobility as a function of Bi fraction for our GaAsBi:Si films, in comparison with Hall data reported in the literature for GaAsBi films with various $n$-type and $p$-type dopants.[48-54] The electron mobility is independent of $y$ up to at least $y$ ~0.01. For $n$-type GaAsBi:Si films with high doping levels ($n$ = 0.97 to 4.0 x 10$^{18}$ cm$^{-3}$), the mobilities are < 600 cm$^2$/(V-s), due to higher carrier concentrations and/or increased carrier compensation due to epitaxial growth near the stoichiometry threshold. For $p$-type GaAsBi:Si films of low doping levels ($p$ = 1.9 to 3.0 x 10$^{17}$ cm$^{-3}$), hole mobilities as high as 70 cm$^2$/(V-s) are apparent. We now compare the Bi-dependence of the hole mobility for our films of high

doping ($p$ = 1.9 to 5.6 x $10^{18}$ $cm^{-3}$) to $p$-type literature reports for films of similar carrier concentrations. At $y$ ~0.04, our films have mobility ~43 $cm^2/(V\text{-}s)$, which is higher than that reported by Beaton[50] (~13 $cm^2/V\text{-}s$ for 0.5 to 2 x $10^{18}$ $cm^{-3}$) but lower than that reported by Kado[52] (~80 $cm^2/V\text{-}s$ for 2x$10^{18}$ $cm^{-3}$). Furthermore, for $p$-type GaAsBi:Si films of high doping levels, the hole mobility is essentially independent of $y$ up to $y$ = 0.043. In contrast, $p$-type doping of GaAsBi with C and Be results in hole mobilities which reportedly decrease monotonically with increasing Bi fraction.[49,50] Thus, Si is a promising alternative to C and Be for $p$-type doping of GaAsBi, especially at large Bi fractions where C and Be doping may lead to a more substantial reduction in mobility than Si doping.

## 4.6 Conclusions

In summary, we have shown that Bi incorporation into GaAsBi is favorable using $As_4$ in lieu of $As_2$, facilitating growth of smooth, droplet-free films, and leading to a similar decrease in the PL bandgap energy due to Bi incorporation. Additionally, we have explored the influence of the stoichiometry threshold on the doping type of silicon in GaAs(Bi) alloys. Growing GaAs(Bi):Si films at low (high) $As_4$/Ga BEP ratios and/or high (low) growth rates leads to growth in the Ga-rich (As-rich) regime. In the Ga-rich regime, growth on (2 x 1) surface reconstructions leads to $p$-type behavior, presumably due to the high areal density of Group V sites available for Si incorporation. Furthermore, free carrier concentrations in excess of 5 x $10^{18}$ $cm^{-3}$ are achieved for $y$ ~0.05, making Si a promising $p$-type dopant for GaAsBi and related bismuthide alloys. The growth-rate dependence of dopant incorporation is likely to be applicable to a wide range of alloys for which epitaxy occurs in the vicinity of the stoichiometry threshold.

## 4.7 Figures

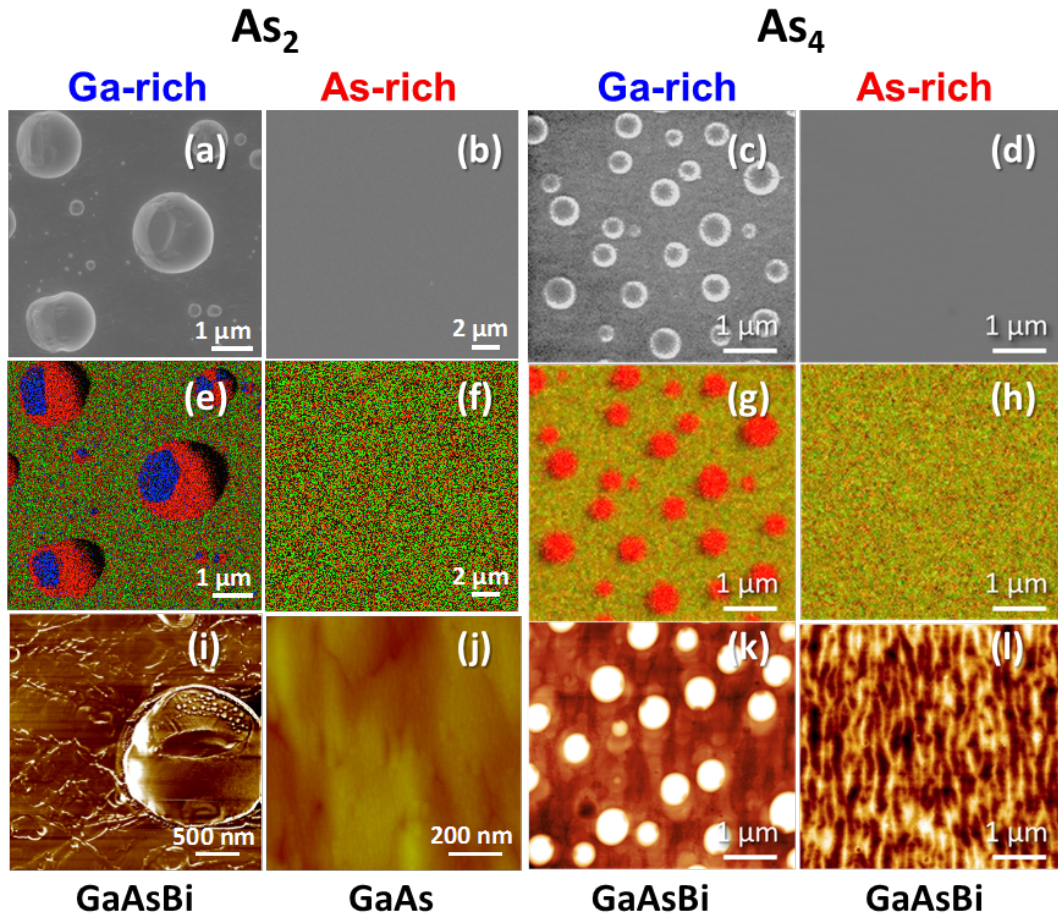


**Figure 4.1** Scanning electron microscopy, corresponding energy dispersive X-ray spectroscopy (EDX), and atomic force microscopy (AFM) images for [(a),(e),(i)] Ga-rich growth using $As_2$, [(b),(f),(j)] As-rich growth using $As_2$, [(c),(g),(k)] Ga-rich growth using $As_4$, and [(d),(h),(l)] As-rich growth using $As_4$. In the EDX images, red, green, and blue correspond to Ga, As, and Bi, respectively. The gray-scale ranges displayed in the AFM images are (j) 60 nm, (k) 160 nm and (l) 10 nm. For the phase AFM image in (i), the gray-scale range corresponds to 20°.

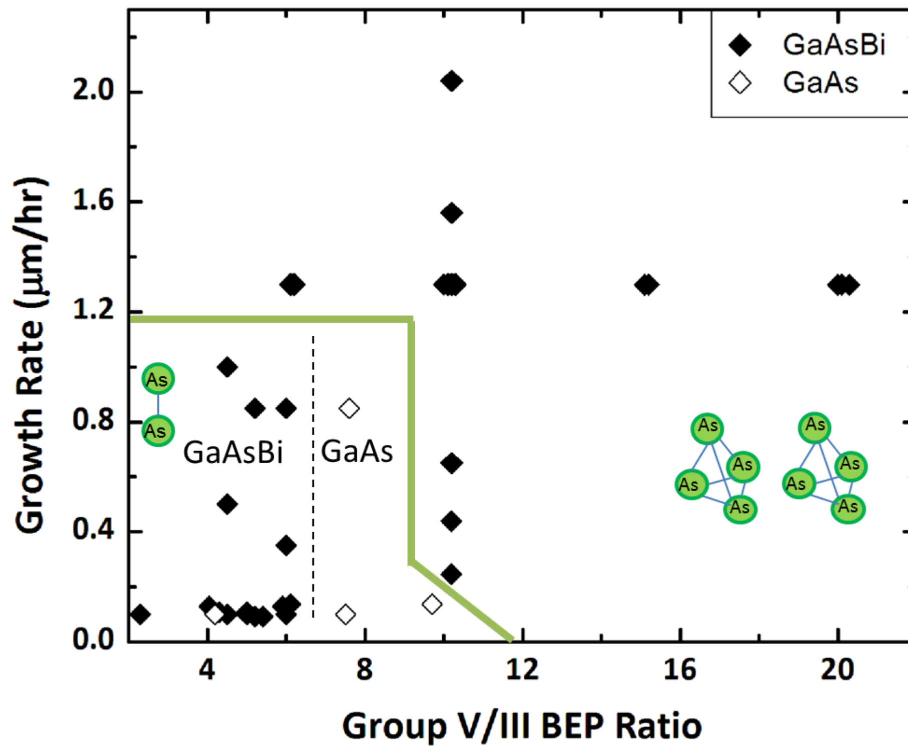


**Figure 4.2** Bi incorporation into GaAs, as a function of growth rate and Group V/III BEP ratio, for various GaAs(Bi) films grown using either $As_2$ or $As_4$. The solid line separates films grown with $As_2$ and $As_4$, with films grown using $As_2$ in the lower-left-hand corner of the plot. All films were exposed to As, Ga and Bi flux. Films with Bi incorporation (no Bi incorporation) are shown as solid (open) symbols. For films grown using $As_2$, a dashed line separates films with Bi incorporation from films without Bi incorporation, with Bi incorporation for Group V/III BEP ratios ≤ 6.

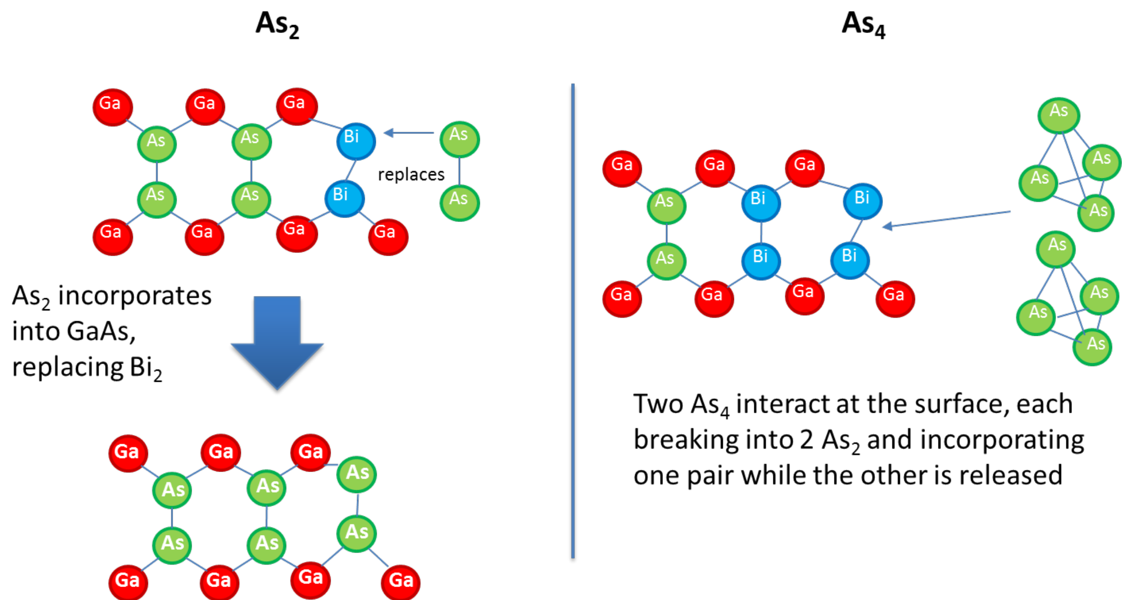


**Figure 4.3** Bi incorporation mechanisms for growth using $As_2$ (left) and $As_4$ (right). We show the surface reconstruction and consider if the active As species can favorably replace Bi dimers on the growth surface. For growth using $As_2$, $As_2$ incorporates into GaAs, replacing surface $Bi_2$. For growth using $As_4$, two $As_4$ interact at the surface, each breaking into 2 $As_2$ and incorporating one pair while the other pair is released.

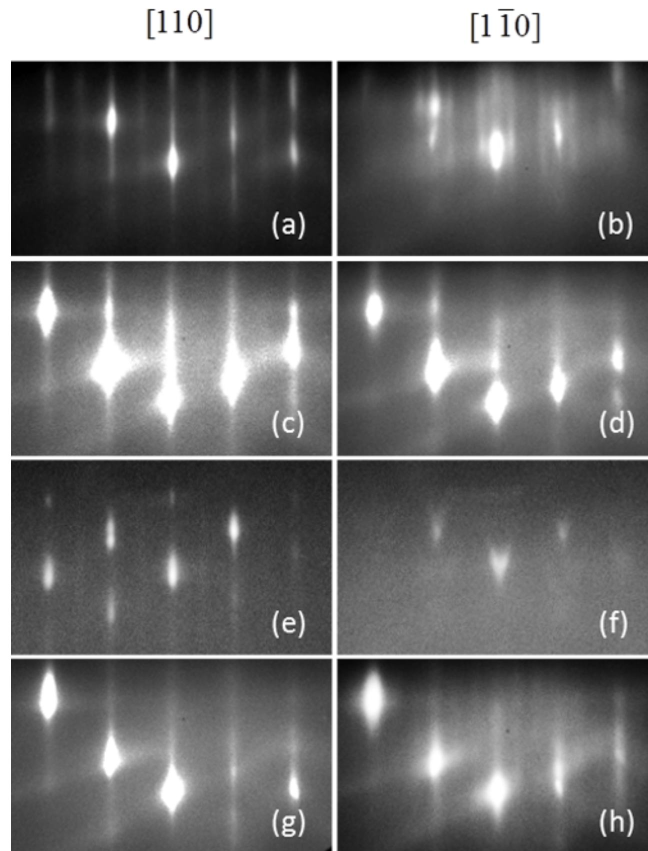


**Figure 4.4** Reflection high-energy electron diffraction patterns collected along [110] and [1 $\bar{1}$ 0] axes during GaAs(Bi):(Si) film growth. [(a), (b)] (2 x 4) pattern during GaAs growth at 600 °C; [(c), (d)] streaky (2 x 3) pattern during GaAs(Si) growth at 280 °C; [(e), (f)] dim (2 x chevron) pattern during *p*-type GaAs(Bi):Si growth at 280 °C; [(g), (h)] streaky (1 x 3) pattern during *n*-type GaAs(Bi):Si growth at 280 °C.

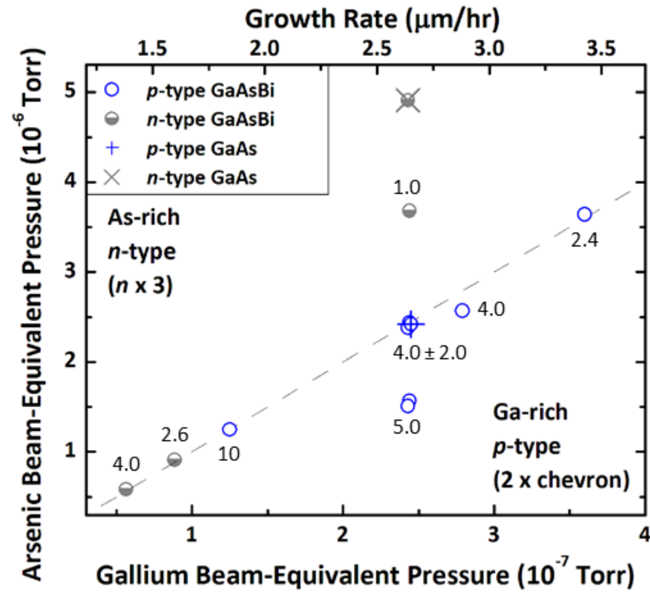


**Figure 4.5** Carrier types and concentrations (x$10^{18}$ cm$^{-3}$) for GaAs(Bi):Si films: arsenic beam-equivalent pressure (BEP) vs. gallium BEP, with growth rate on the upper *x*-axis. We note that the growth rate *x*-axis applies to data in the As-rich growth regime. A dotted line indicates the regime where the Group V/III BEP ratio is equal to 10, "BEPratio10". All GaAsBi:Si films above (below) the BEPratio10 line are *n*-type (*p*-type). In addition, along the BEPratio10 line, there is a carrier-type conversion from *n*-type to *p*-type as the growth rate increases (from 0.25 to 2.0 μm/hr), consistent with the growth rate dependence of the stoichiometry threshold reported in Ref. 31.

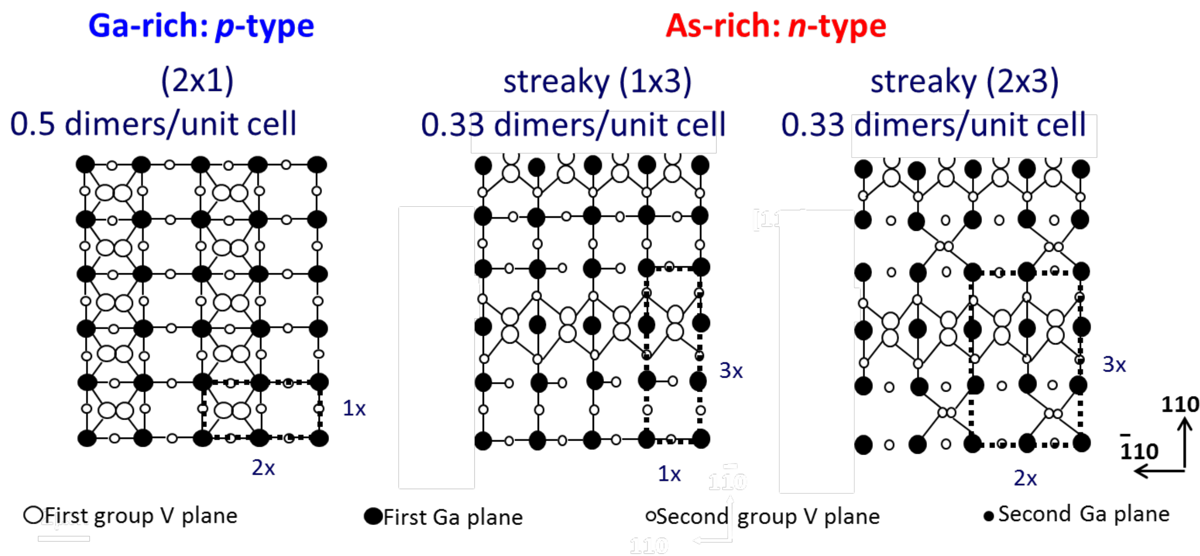


**Figure 4.6** Surface reconstructions for GaAsBi films grown under Ga-rich (left) and As-rich (right) conditions. Films grown under Ga-rich conditions have (2 x 1) reconstructed surfaces, and films grown under As-rich conditions have (*n* x 3) reconstructed surfaces. The (2 x 1) reconstructed surfaces have significantly more Group V sites per unit area than the (*n* x 3) reconstructed surfaces.

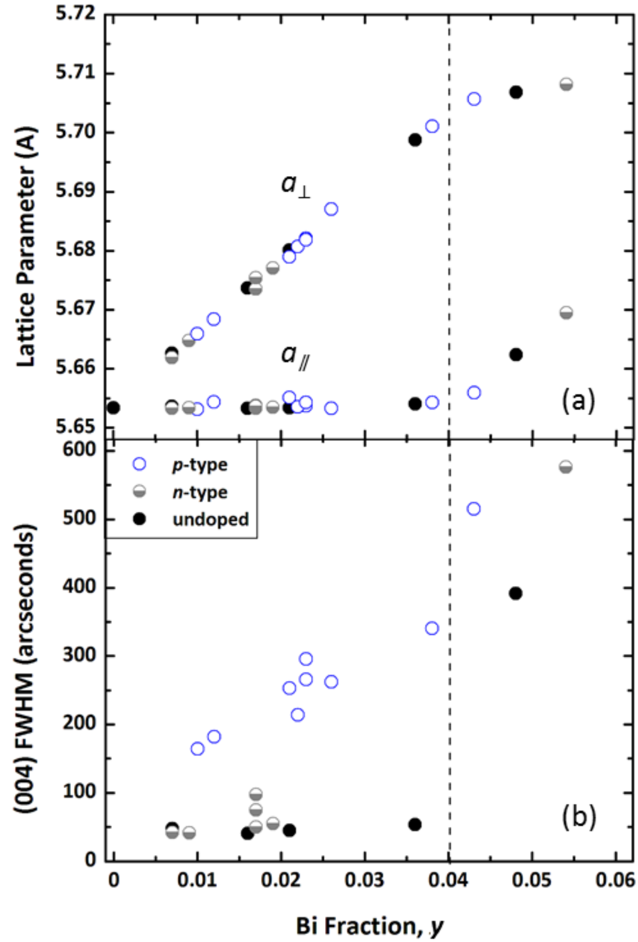


**Figure 4.7** (a) In-plane, $a_{//}$, and perpendicular, $a_\perp$, lattice parameters and (b) FWHM of the (004) GaAsBi diffraction peak, both as a function of Bi fraction, *y*. For $y < 0.04$, $a_\perp$ increases with increasing *y*, independent of doping type and concentration. For $y > 0.04$, $a_{//}$ begins to increase while $a_\perp$ is nearly constant, suggesting that the film lattice has begun to relax to its intrinsic lattice parameter. For undoped GaAsBi and *n*-type GaAsBi:Si with $y < 0.04$, the FWHM of the GaAsBi peak is nearly constant; for $y > 0.04$, the FWHM increases with *y*. For *p*-type GaAsBi:Si, the FWHM of the GaAsBi peak increases monotonically with *y*.

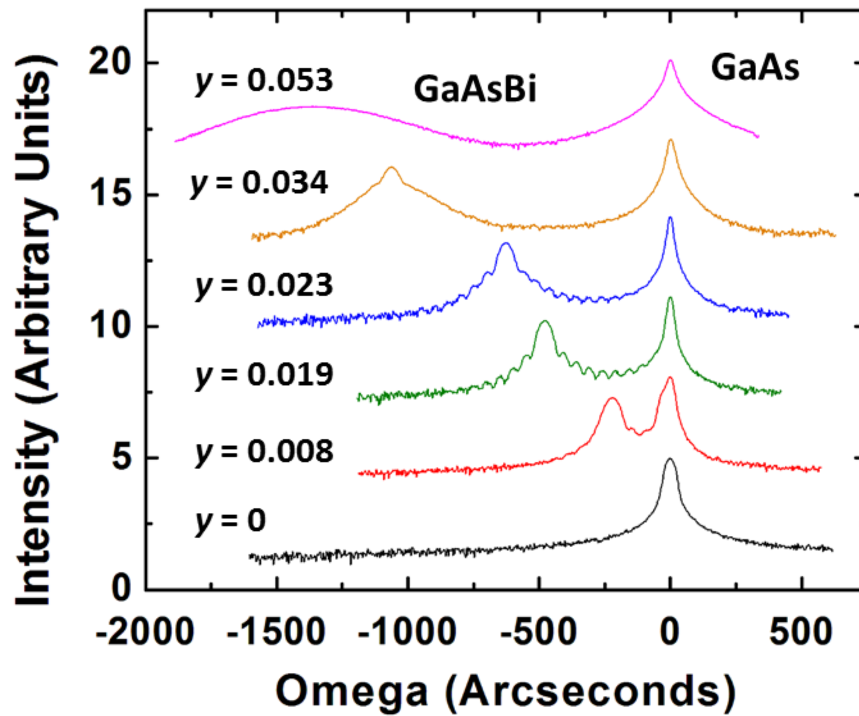


**Figure 4.8** Symmetric (004) high-resolution X-ray rocking curves for GaAsBi films of various Bi fraction, *y*. The peak separation between the GaAs and GaAsBi diffraction peak increases as *y* increases. Furthermore, for $y < 0.04$, Pendellosung fringes are apparent, indicating smooth epilayer surfaces and interfaces.

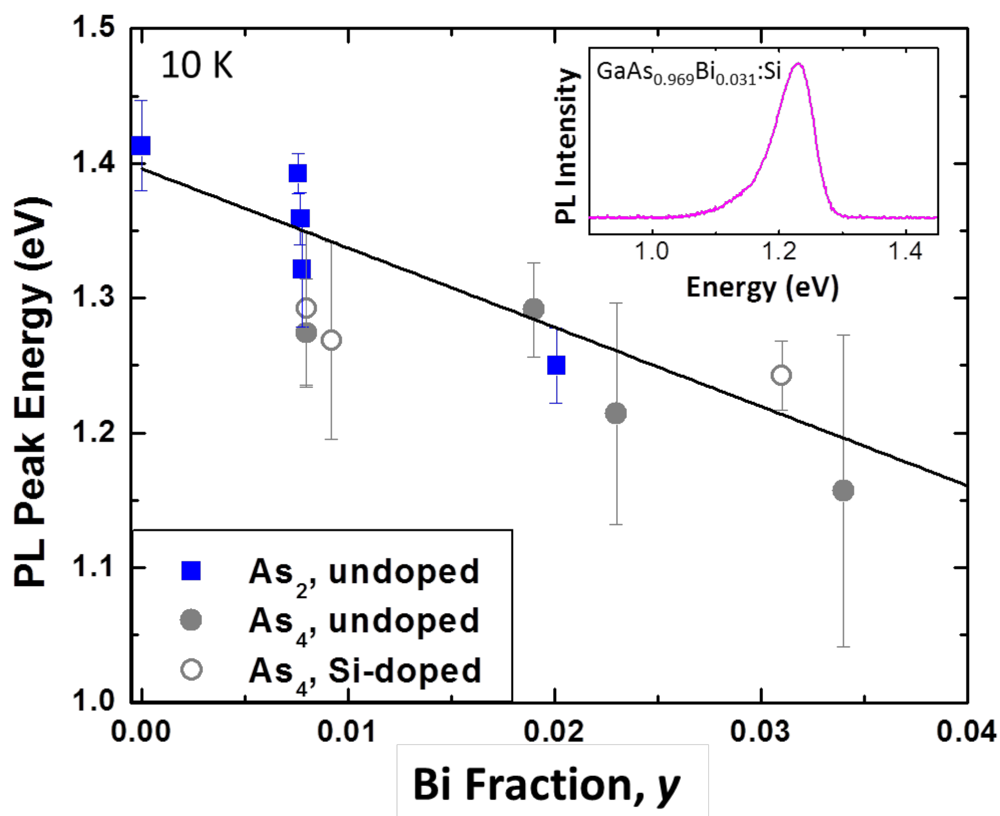


**Figure 4.9** Peak energy of photoluminescence data (10 K) as a function of Bi fraction, $y$, for films grown with $As_2$ and $As_4$. The inset shows a typical PL trace for a $GaAs_{0.969}Bi_{0.031}$:Si film. There is a similar energy decrease per percent Bi fraction, $\Delta E/y$, for films grown with $As_2$ vs. $As_4$.

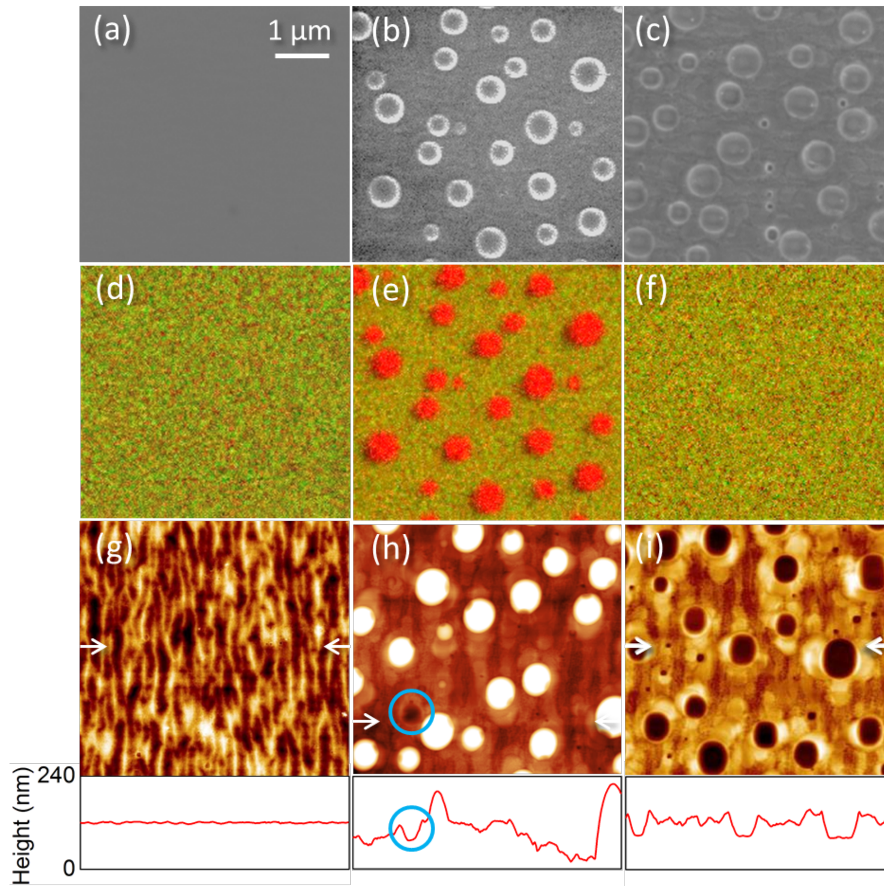


**Figure 4.10** Scanning electron microscopy, corresponding energy dispersive X-ray spectroscopy (EDX), and atomic force microscopy (AFM) images for [(a), (d), (g)] *n*-type $GaAs_{0.992}Bi_{0.008}$:Si, as well as *p*-type $GaAs_{0.991}Bi_{0.009}$:Si [(b), (e), (h)] before and [(c), (f), (i)] after etching with HCl:$H_20$ (1:3). Etching in HCl removes Ga droplets from GaAsBi:Si films. In the EDX images, red, green, and blue correspond to Ga, As, and Bi, respectively. The gray-scale ranges displayed in the AFM images are (c) 10 nm, (f) 160 nm, and (i) 100 nm.

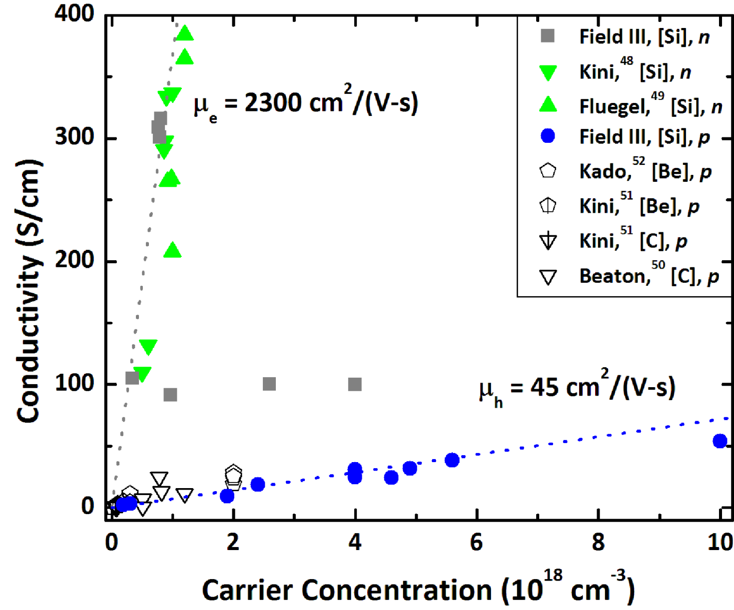


**Figure 4.11** Conductivity vs. carrier concentration for bulk $GaAs_{1-y}Bi_y$:Si films, in comparison with literature reports for GaAsBi films doped with various impurities. The dashed lines form an envelope corresponding to mobilities of ~2300 and ~45 $cm^2/(V\text{-}s)$ for *n*-type and *p*-type films, respectively. The *n*- vs. *p*-type doping of GaAsBi:Si is controlled by varying the Group V/III beam-equivalent pressure ratio and/or growth rate. We demonstrate *n*-type mobilities up to 2500 $cm^2/(V\text{-}s)$ ($n = 8 \times 10^{17}$ $cm^{-3}$), higher than previously reported electron mobilities for GaAsBi For our *n*-type films grown near the stoichiometry threshold, mobilities lie near the mid-range of the envelope. For our *p*-type films with Bi fractions up to 0.05, free carrier concentrations in excess of $5 \times 10^{18}$ $cm^{-3}$ are achieved, a significant increase over literature reports of $\sim 2 \times 10^{18}$ $cm^{-3}$. See Ref. 48. See Ref. 49. See Ref. 50. See Ref. 51. See Ref. 52.

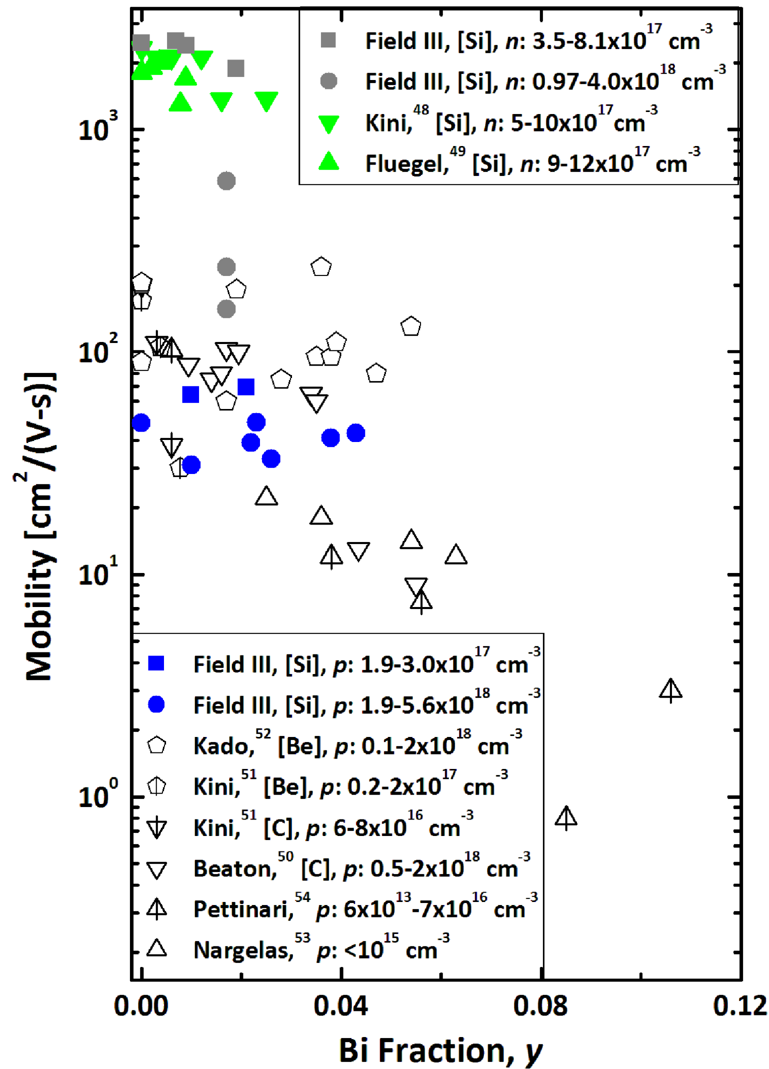


**Figure 4.12** Mobility vs. Bi fraction, $y$, for bulk $GaAs_{1-y}Bi_y$:Si films, in comparison with literature reports for GaAsBi films doped with various impurities. Our films of low and high doping levels are plotted as squares and circles, respectively. The $n$- vs. $p$-type doping of GaAsBi:Si is controlled by varying the Group V/III beam equivalent pressure ratio and/or growth rate. Our $n$-type films exhibit electron mobilities as high as 2500 $cm^2/(V\text{-}s)$ ($n = 8 \times 10^{17}$ $cm^{-3}$), higher than previously reported electron mobilities for GaAsBi. Our $p$-type films exhibit $x$-independent hole mobilities as high as 70 $cm^2/(V\text{-}s)$ ($p = 1.9$ to $4.0 \times 10^{17}$ $cm^{-3}$), in contrast to Be- and C-doped GaAsBi, where a decrease in hole mobility with increasing $x$ has been reported. See Ref. 48. See Ref. 49. See Ref. 50. See Ref. 51. See Ref. 52. See Ref. 53. See Ref. 54.

## 4.8 References

[1] K. Oe, and H. Okamoto, Jpn. J. Appl. Phys. 37, L1283 (1998).

[2] S. Tixier, M. Adamcyk, T. Tiedje, S. Francoeur, A. Mascarenhas, P. Wei, and F. Schiettekatte, Appl. Phys. Lett. 82, 2245 (2003).

[3] A.J. Ptak, S.W. Johnston, S. Kurtz, D.J. Friedman and W.K. Metzger, J. Cryst. Growth 251, 392 (2003).

[4] D.A. Livshits, A.Y. Egorov and H. Riechert, Electron. Lett. 36, 1381 (2000).

[5] W. Li, T. Jouhti, C.S. Peng, J. Konttinen, P. Laukkanen, E.M. Pavelescu, M. Dumitrescu and M. Pessa, Appl. Phys. Lett. 79, 3386 (2001).

[6] K.D. Choquette, J.F. Klem, A.J. Fischer, O. Blum, A.A. Allerman, I.J. Fritz, S.R. Kurtz, W.G. Breiland, R. Sieg, K.M. Geib, J.W. Scott and R.L. Naone, Electron. Lett. 36, 1388 (2000).

[7] G. Steinle, H. Riechert and A.Y. Egorov, Electron. Lett. 37, 93 (2001).

[8] M.J. Antonell, C.R. Abernathy, A. Sher, M. Berding, M. Van Schilfgaarde, A. Sanjuro, and K. Wong, J. Cryst. Growth 188, 113 (1998).

[9] T. B. Massalski and H. Okamoto, Binary Alloy Phase Diagrams (ASM International, New York, 1990), pp. 738.

[10] X. Lu, D.A. Beaton, R.B. Lewis, T. Tiedje, and M.B. Whitwick, Appl. Phys. Lett. 92, 192110 (2008).

[11] G. Vardar, S.W. Paleg, M.V. Warren, M. Kang, S. Jeon, and R.S. Goldman, Appl. Phys. Lett. 102, 042106 (2013).

[12] J. Xu, E. Towe, Q. Yuan, and R. Hull, J. Cryst. Growth 196, 26 (1999).

[13] W. I. Wang, E. E. Mendez, T. S. Kuan, and L. Esaki, Appl. Phys. Lett. 47, 826 (1985).

[14] L. Pavesi, F. Piazza, M. Henini, and I. Harrison, Semicond. Sci. Technol. 8, 167 (1993).

[15] S. Tibebu Kassa, R. Hey, and K.H. Ploog, J. Appl. Phys. 93, 2638 (2003).

[16] G. B. Galiev, V. E. Kaminskii, V. G. Mikerov, and L.E. Velikhovskii, Semicond. 35, 427 (2001).

[17] E. S. Tok, J. H. Neave, M. J. Ashwin, and B. A. Joyce, J. Appl. Phys. 83, 4160 (1998).

[18] H. P. Meier, R. F. Broom, P. W. Epperlein, E. van Gieson, Ch. Harder, H. Jackel, W. Walter, and D. J. Webb, J. Vac. Sci. Technol. B 6, 692 (1988).

[19] N. Sakamoto K. Hirakawa, and T. Ikoma, Appl. Phys. Lett. 67, 1444 (1995).

[20] F. Fisher, D. Schuh, M. Bichler, G. Abstreiter, and M. Grayson, Appl. Phys. Lett. 86, 192196 (2005).

[21] K. Fujita, A. Shinoda, M. Inai, T. Yamamoto, M. Fujii, D. Lovell, T. Takebe, and K. Kobayshi, J. Cryst. Growth 127, 50 (1993).

[22] D. L. Miller, Appl. Phys. Lett 47, 1309 (1985).

[23] A. A. Quivy, A. L. Sperandio, E. C. F. da Silva, and J. R. Leite, J. Cryst. Growth 206, 171 (1999).

[24] T. E. Lamas, A. A. Quivy, S. Martini, M. J. da Silva, and J. R. Leite, Thin Solid Films 474, 25 (2005).

[25] S. Fukushima, T. Obata, and N. Otsuka, J. Appl. Phys. 89, 380 (2001).

[26] D.K. Bowen and B.K. Tanner, *High Resolution X-ray Diffraction and Topography*, (Taylor & Francis, London, 1998), pp. 31.

[27] Z. Pan, Y.T. Wang, L.H. Li, W. Zhang, Y.W. Lin, Z.Q. Zhou and R.H. Wu, J. Cryst. Growth 217, 26 (2000).

[28] A. Janotti, S.-H. Wei, and S. Zhang, Phys. Rev. B 65, 115203 (2002).

[29] C. X. Zheng, W. X. Tang, and D. E. Jesson, Appl. Phys. Lett. 100, 071903 (2012).

[30] C. Somaschini, S. Bietti, N. Koguchi, and S. Sanguinetti, Nano Lett. 9, 3419 (2009).

[31] G. Vardar, S. W. Paleg, M. V. Warren, M. Kang, S. Jeon, and R. S. Goldman, Appl. Phys. Lett. 102, 042106 (2013).

[32] P. Kratzer, E. Penev, and M. Scheffler, Appl. Phys. A 75, 79 (2002).

[33] F. Bastiman, A.R.B. Mohmad, J. S. Ng, J.P.R. David, and S. J. Sweeney, J. Cryst. Growth 338, 57 (2012).

[34] K. Forghani, A. Anand, L.J. Mawst, and T. F. Kuech, J. Cryst. Growth 380, 23 (2013).

[35] R.R. Wixom and G.B. Stringfellow, Phys. Rev. B 64, 201322(R) (2001).

[36] H. Shigekawa, H. Oigawa, K. Miyake, Y. Aiso, Y. Nannichi, T. Hashizume, and T. Sakurai, Appl. Phys. Lett. 65, 607 (1994).

[37] T. Kita, O. Wada, T. Nakayama, and M. Murayama, Phys. Rev. B 66, 195312 (2002).

[38] J. Northrup and S.B. Zhang, Phys. Rev. B 47, 6791 (1993).

[39] S. Fukushima, T. Obata, and N. Otsuka, J. Appl. Phys. 89, 380 (2001).

[40] D. F. Reyes, F. Bastiman, C.J. Hunter, D.L. Sales, A.M. Sanchez, J.P.R. David, and D. Gonzalez, Nanoscale Res. Lett. 9, 23 (2014).

[41] R. S. Goldman, K. L. Kavanagh, H. H. Wieder, V. M. Robbins, S. N. Ehrlich, and R. M. Feenstra, J. Appl. Phys. 80, 6849 (1996).

[42] S. Francoeur, M.-J. Seong, A. Mascarenhas, S. Tixier, M. Adamcyk, and T. Tiedje, Appl Phys. Lett. 82, 3874 (2003).

[43] T. Hanada, B. H. Koo, H. Totsuka, and T. Yao, Phys. Rev. B - Condens. Matter Mater. Phys. 64, 1653071 (2001).

[44] D. W. Pashley, J. H. Neave, and B. A. Joyce, Surf. Sci. 476, 35 (2001).

[45] C. Somaschini, S. Bietti, S. Sanguinetti, A. Fedorov, N. Koguchi and A. Fedorov, Nanotechnology 21, 125601 (2010).

[46] A. Okazaki, K. Horibe, K. Maruyama, and S. Miyazima, Phys. Rev. E 61, 6215 (2000).

[47] S. Wagner and A. Pundt, Phys. Rev. B 78, 155131 (2008).

[48] R. N. Kini, L. Bhusal, A. J. Ptak, R. France, and A. Mascarenhas, J. App. Phys. 106, 043705 (2009).

[49] B. Fluegel, R. N. Kini, A. J. Ptak, D. Beaton, K. Alberi, and A. Mascarenhas, Appl. Phys. Lett. 99, 162108 (2011).

[50] D. A. Beaton, R. B. Lewis, M. Masnadi-Shirazi, and T. Tiedje, J. Appl. Phys. 108, 083708 (2010).

[51] R. N. Kini, A. J. Ptak, B. Fluegel, R. France, R. C. Reedy, and A. Mascarenhas, Phys. Rev. B 83, 075307 (2011).

[52] K. Kado, T. Fuyuki, K. Yamada, K. Oe, and M. Yoshimoto, Jpn. J. Appl. Phys. 51, 040204 (2012).

[53] S. Nargelas. K. Jarasinas, K. Bertulis, and V. Paebutas, Appl. Phys. Lett. 98, 082115 (2011).

[54] G. Pettinari, A. Patane, A. Polimeni, M. Capizzi, X. Lu, and T. Tiedje, Appl. Phys. Lett. 100, 092109 (2012).

# Chapter 5

# Summary and Suggestions for Future Work

## 5.1 Summary

In this dissertation work, we studied the growth and electronic properties of GaAsN and GaAsBi alloys. For GaAsN, we examined the origins of persistent photoconductivity (PPC), and then used PPC to drive a metal-insulator transition in GaAsN and extract the electron effective mass. For GaAsBi, we examined the influence of As species on GaAsBi growth and properties, as well as the influence of the growth-rate dependence of film stoichiometry on dopant incorporation.

In Chapter 3, we investigated the influence of N environment on the PPC effect in $GaAs_{1-x}N_x$. For $x > 0.006$, significant PPC is observed at cryogenic temperatures, with the PPC magnitude increasing with increasing $x$, due to an increase in the density of N-induced levels. Interestingly, rapid thermal annealing suppresses the PPC magnitude and reduces the N interstitial fraction; thus, the N-induced level is likely associated with N interstitials. PPC in GaAsN is attributed to the photoexcitation of carriers from a N-induced level to the CBE, leading to a modified molecular bond configuration of the N-induced level. With sufficient thermal energy, the original N-induced level configuration is restored, and the N-induced level is able to accept carriers once again. The change in molecular bond configuration is likely a bond reorientation or a shift in the center of mass. Furthermore, we have used

PPC to drive a metal-insulator transition in GaAsN, allowing us to extract the electron effective mass using the Mott criterion. It has been reported that the effective mass of GaAsN is dopant-dependent. We find that the effective mass for Si-doped GaAsN is consistent with the linear combination of isolated N resonant states (LCINS) model, suggesting that N cluster states may influence the effective mass in GaAsN:Si.

In Chapter 4, we showed that Bi incorporation into GaAsBi is favorable using $As_4$ in lieu of $As_2$, facilitating growth of smooth, droplet-free films, and leading to a similar reduction in the photoluminescence (PL) peak energy due to Bi incorporation. Additionally, we explored the influence of the stoichiometry threshold on the doping type of silicon in GaAs(Bi) alloys. Growing GaAs(Bi):Si films at low (high) $As_4$/Ga beam-equivalent pressure (BEP) ratios and/or high (low) growth rates leads to growth in the Ga-rich (As-rich) regime. In the Ga-rich regime, growth on (2 x 1) surface reconstructions leads to *p*-type behavior, presumably due to the high areal density of Group V sites available for Si incorporation. Furthermore, free carrier concentrations in excess of $5 \times 10^{18}$ $cm^{-3}$ are achieved for Bi fractions ~0.05, making Si a promising *p*-type dopant for GaAsBi and related bismuthide alloys. The growth-rate dependence of dopant incorporation is likely to be applicable to a wide range of alloys for which epitaxy occurs in the vicinity of the stoichiometry threshold.

## 5.2. Suggestions for future work

### 5.2.1 Resonant electron scattering from isolated N-induced levels

In Chapter 3, we showed that N-induced levels are responsible for extraordinary phenomena, such as persistent photoconductivity in GaAsN alloys. However, the positions of N-induced levels in the bandgap remain unknown. As a method to investigate the positions of N-induced levels, a novel GaAsN heterostructure has been proposed as a spectroscopic probe of the localized states in the dilute nitride layer, as shown in Fig. 5.1.[1] Subsequently, the author has grown this heterostructure via molecular-beam epitaxy (MBE). This heterostructure contains an AlGaAs/InGaAs 2-dimensional electron gas and a GaAsN layer, along with a built-in back gate, enabling control of the Fermi level energy relative to the N-induced levels. The electron mobility is expected to decrease significantly when the Fermi level is resonant with the N-induced levels,[1] due to the reduced electron mobility in GaAsN. Thus, the mobility measurements can be used as a spectroscopic probe of the N-induced levels.

### 5.2.2 Influence of dopants on the properties of GaAsN/GaAsBi heterostructures

In Chapter 3, we introduced a new method to accurately extract the effective mass, $m_e$*, using the Mott criterion, whereby PPC drives a metal-insulator transition. It has been reported that dopants influence $m_e$* in GaAsN.[2] Specifically, N cluster states lead to a non-monotonic increase in $m_e$* with Te- and Se-doping,[3] whereas Si-doping, without the influence of N clusters, reportedly leads to a monotonic increase.[2] However, we found that $m_e$*

for Si-doped GaAsN is higher than the predictions of the BAC model, implying that N clusters may influence $m_e$* in GaAsN:Si. However, a more thorough study of the $x$-dependence of $m_e$* in GaAsN:Si is suggested. Similarly, the influence of alternative (Se, Te) and amphoteric (Si, Ge) dopants on the microstructure, electronic transport, and optical absorption/emission of GaAsNBi-based alloys and heterostructures is suggested.

### 5.2.3 Growth of GaAsN/GaAsBi heterostructures

In Chapter 4, we demonstrated high-quality epitaxial growth of thick, droplet-free GaAsBi films. Furthermore, GaAsBi with substantial Bi incorporation, up to $y = 0.22$, has been reported.[4] Additionally, a crossover such that $\Delta_{SO} > E_g$ has been reported for $y = 0.105$, corresponding to a suppression of Auger recombination, with a corresponding bandgap of 0.8 eV;[5] Therefore, GaAsBi alloys are mature for a variety of optoelectronic applications, such as long-wavelength light emitters[6-8] and detectors,[9-11] high-performance heterojunction bipolar transistors,[12-17] and high-efficiency photovoltaic devices.[18,19]

In order to identify favorable growth conditions for GaAsN/GaAsBi heterostructures and superlattices, as well as GaAsNBi alloys, we suggest examining the growth of GaAsN with $As_4$ at similarly low temperatures ($T$ <300 °C). For growth of GaAsN/GaAsBi heterostructures and superlattices, a balance must be found between increased Bi incorporation around 280 °C,[20] and the window for growth of high-quality GaAsN films in the range 400 – 425 °C. To date, few groups have grown GaAsNBi films, all using MBE with substrate temperatures in the range 350-400 °C.[21,22] For growth using $As_4$, standard V/III BEP ratios (~20) should allow simultaneous incorporation of N and Bi into GaAsNBi. Therefore,

growth of GaAsNBi films at different temperatures in the 350-400 °C range, at V/III BEP ratio of 20, is suggested as a first growth in order to optimize Bi incorporation and surface morphology. However, additional studies of the influence of the V/III BEP ratio, growth temperature, and/or growth rate may be required if smooth films with both N and Bi incorporation are not obtained with this preliminary growth. Furthermore, a strain-balanced $GaAs_{0.956}N_{0.014}Bi_{0.03}$ film with a room-$T$ PL peak at 1.05 eV has been demonstrated.[21] In Prof. Goldman's MBE lab, N and Bi fractions up to 0.031 and 0.06 have been incorporated into GaAs, respectively, implying that a strain-balanced alloy with a 1.05-eV bandgap should be achievable in Prof. Goldman's MBE lab.

As an example of one application, we now consider the inclusion of GaAsBi into high-efficiency photovoltaic devices for space applications. As discussed in Sec. 1.4.3, the optimal heterostructure is predicted to have bandgap energies of sequence 1.9 eV, 1.42 eV, 1.05 eV, and 0.67 eV,[23] which improves efficiency by reducing thermalization losses. To date, GaAsN-based materials have been introduced as the 1.05-eV cell.[24] We propose replacement of GaAsN-based cells with GaAsBi-based cells, due to [1] the higher values of the electron mobility in GaAsBi (see Sec. 1.3.3),[25] and [2] the suppression of Auger recombination.[5] For GaAsBi, a bandgap of 1.05 eV has been obtained for $y$ ~0.05;[5] Bi fractions in this range have also been synthesized in Prof. Goldman's MBE lab. Thus, GaAsBi alloys are currently capable of achieving the 1.05-eV bandgap necessary for inclusion of these alloys into high-efficiency multi-junction PV devices.

Furthermore, incorporation of both N and Bi, to form GaAsNBi alloys, can maintain exact-lattice matching to GaAs for the 1.05-eV cell, making these alloys particularly promising. Experimentally, strain-balanced $Ga(As_{0.33}Bi_{0.67})_wAs_{1-w}$ films, with a room-$T$ PL peak down to 0.96 eV, have been realized.[21,26] An observed reduction in the intensity of the

PL intensity, and subsequent annealing-induced increase in PL intensity, has been reported,[21,26] similar to the case of N in GaAsN and InGaAsN alloys.[27-29] Furthermore, the temperature coefficient of the PL peak energy for GaAsNBi is reportedly 0.16 meV/K, similar to the temperature coefficient for GaAsBi,[21] but smaller than the temperature dependence for InGaAsP alloys.[30] Thus, GaAsNBi alloys are particularly promising since costly, temperature-stabilizing elements may not be necessary for inclusion of these alloys into PV and/or laser applications.

### 5.2.4 Reduction of droplets on *p*-type GaAsBi:Si films

In Chapter 4, we showed that *p*-type GaAsBi:Si films exhibit Ga-based surface droplets, due to MBE growth in Ga-rich conditions. Here, we offer suggestions to eliminate or reduce the droplet surface coverage. Cluster formation is often described in three stages: nucleation (emergence of clusters), early-stage growth (cluster growth), and late-stage growth (cluster coarsening).[31] Therefore, to eliminate/reduce droplet formation, we suggest preventing/reducing droplet nucleation during the first stage of cluster formation.

During the nucleation stage, surfaces remain featureless until a critical ion dose is reached. Droplet formation can be described in terms of surface supersaturation, $S(t)$:

$$S\left(t\right)=\frac{C\left(t\right)-C_{eq}\left(t\right)}{C_{eq}\left(t\right)}\ , \tag{5.1}$$

where, for Ga irradiation on GaAs, $C(t)$ is the total [Ga] concentration and $C_{eq}$ is the bulk Ga solubility in GaAs.[31-33] During initial radiation, $S(t)$ increases to a critical value, $S_c$, at which point nucleation begins. Furthermore, during the nucleation process, clusters with radius $R > R_c$ grow, while clusters with radius $R < R_c$ dissolve. In order to eliminate droplet for-

mation, $S(t) < S_c$ must be maintained throughout growth, which can be accomplished by reducing $C(t)$ as follows: [1] reducing the rate at which Ga is deposited on the surface (increasing the V/III BEP ratio), or [2] reducing the time that the film is exposed to Ga irradiation (increasing the growth rate and/or decreasing the film thickness). In Fig. 5.2, we summarize the droplet surface coverage (percent) for GaAsBi:Si films in the plot of As BEP vs. Ga BEP, with growth rate on the upper $x$-axis. Indeed, the droplet surface coverage decreases as either the V/III BEP ratio or the growth rate is increased. Furthermore, the growth-rate dependence of the stoichiometry threshold will allow simultaneous increase of both the V/III BEP ratio and growth rate, potentially enabling further reduction of the droplet surface coverage. However, for Ga-rich growth of GaAsBi, Bi acts as an anti-surfactant, inducing Ga-Bi droplet formation.[34] Thus, low Bi BEPs may also be required to reduce droplet surface coverage (which would also reduce the Bi fraction in the GaAsBi films).

### 5.3 Figures

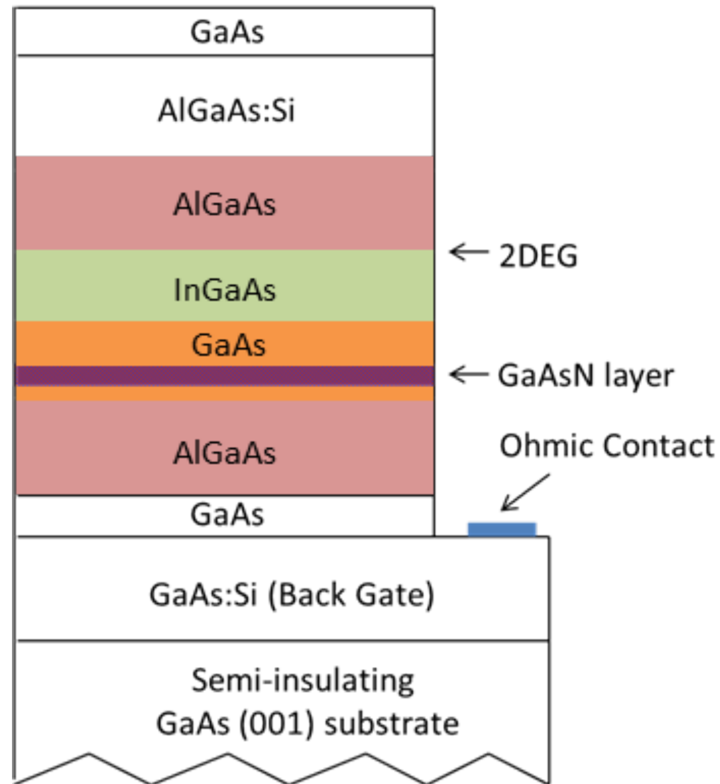


**Figure 5.1** GaAsN heterostructure with a two-dimensional electron gas and a GaAsN layer, including a built-in back gate to control the Fermi level energy relative to the N-induced levels. The electron mobility is expected to decrease significantly when the Fermi level is resonant with the N-induced levels;[1] thus, the mobility measurements can be used as a spectroscopic probe of the N-induced levels.

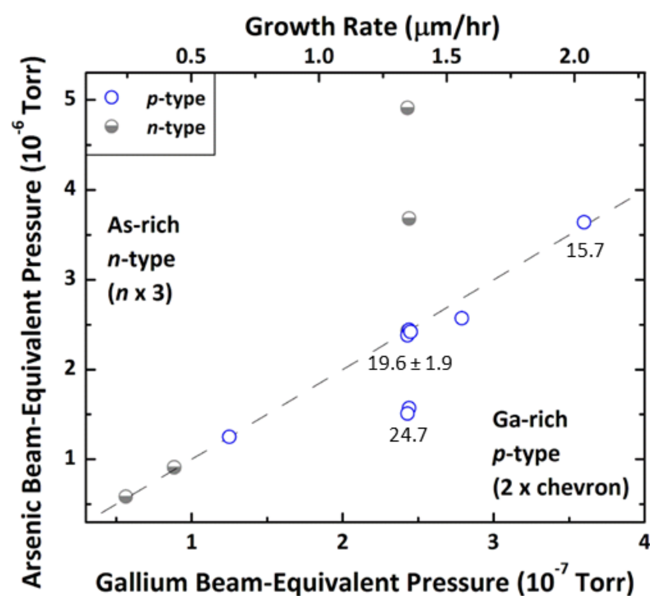


**Figure 5.2** Carrier types and droplet surface coverage (percent) for GaAs(Bi):Si films: arsenic beam-equivalent pressure (BEP) vs. Ga BEP, with growth rate on the upper *x*-axis. We note that the growth rate *x*-axis applies to data in the As-rich growth regime. A dotted line indicates the regime where the Group V/III BEP ratio is equal to 10, "BEPratio10". The droplet surface coverage decreases as either the V/III BEP ratio or the growth rate is increased.

### 5.4 References

[1] J. Buckeridge and S. Fahy, Phys. Re. B 84, 144120 (2011).

[2] P. Pichanusakorn, Y. J. Kuang, C. Patel, C. W. Tu, and P. R. Bandaru, Phys. Rev. B 86, 085314 (2012).

[3] T. Dannecker, Y. Jin, H. Cheng, C.F. Gorman, J. Beckeridge, C. Uher, S. Fahy, C. Kurdak, and R.S. Goldman, Phys. Rev. B 82, 125203 (2010).

[4] R.B. Lewis, M. Masnadi-Shirazi, and T. Tiedje, Appl. Phys. Lett. 101, 082112 (2012).

[5] Z. Batool, K. Hild, T.J.C. Hosea, X. Lu, T. Tiedje, and S.J. Sweeney, J. Appl. Phys. 111, 113108 (2012).

[6] J.S. Harris, Semicond. Sci. Technol. 17, 880 (2002).

[7] L.H. Li, V. Sallet, G. Patriarche, L. Largeau, S. Bouchoule, K. Merghem, L. Travers, and J.C. Harmand, Electron. Lett. 39, 519 (2003).

[8] H. Reichert, A. Ramakrishnan, and G. Steinle, Semicond. Sci. Technol. 17, 892 (2002).

[9] M.R. Gokhale, J. Wei, H. Wang, and S.R. Forrest, Appl. Phys. Lett. 74, 1287 (1999).

[10] B. Sciana, I. Zborowska-Lindert, D. Pucicki, B. Boratynski, D. Radziewicz, M. Tlaczala, J. Serafinczuk, P. Poloczek, G. Sek, and J. Misiewicz, Opto-Electronics Review 16, 1 (2008).

[11] J.-Y. Duboz, M. Hugues, B. Damilano, A. Nedelcu, P. Bois, N. Kheirodin, and F.H. Julien, Appl. Phys. Lett. 94, 022103 (2009).

[12] P.C. Chang, N.Y. Li, A.G. Baca, H.Q. Hou, C. Monier, J.R. Laroche, F. Ren, and S.J. Pearton, IEEE Electron Dev. Lett. 22, 113 (2001).

[13] C. Monier, A.G. Baca, P.C. Chang, N.Y. Li, H.Q. Hou, F. Ren, and S.J. Pearton, Electron. Lett. 37, 198 (2001).

[14] P.M. Asbeck, R.J. Welty, C.W. Tu, H.P. Xin, and R.E. Welser, Semicond. Sci. Techno. 17, 898 (2002).

[15] K.L. Lew, S.F. Yoon, H. Wang, W. Wicaksono, J.A. Gupta, S.P. McAlister, J. Vac. Sci. Technol. B 24, 1308 (2006).

[16] I. Hase, Heterojunction bipolar transistor with a base layer that contains bismuth, US Patent #7,009,225 (2006).

[17] Z.D. Marks, I.W. Haygood, and B. VanZeghbroeck, IEEE Trans. Electron Dev. 60, 200 (2012).

[18] J.F. Geisz and D.J. Friedman, Semicond. Sci. Technol. 17, 769 (2002).

[19] D.B. Jackrel, S.R. Bank, H.B. Yuen, M.A. Wistey, J.S. Harris, A.J. Ptak, S.W. Johnston, D.J. Friedman, and S.R. Kurtz, J. Appl. Phys. 101, 114916 (2007).

[20] M. Reason, N.G. Rudawski, H.A. McKay, X. Weng, W. Ye, and R.S. Goldman, J. Appl. Phys. 101, 083520 (2007).

[21] W. Huang, K. Oe, G. Feng, and M. Yoshimoto, J. Appl. Phys. 98, 053505 (2005).

[22] S. Tixier, S.E. Webster, E.C. Young, T. Tiedje, S. Francoeur, A. Mascarenhas, P. Wei, and F. Schiettekatte, Appl. Phys. Lett. 86, 112113 (2005).

[23] D.J. Friedman, J.F. Geisz, S.R. Kurtz and J.M. Olson, J. Crsyt. Growth 195, 409 (1998).

[24] M. Kondow, K. Uomi, A. Niwa, T. Kitatani, S. Wataiki, and Y. Yazama, Jpn. J. Appl. Phys., Part 1 35, 1273 (1996).

[25] R. N. Kini, A. J. Ptak, B. Fluegel, R. France, R. C. Reedy, and A. Mascarenhas, Phys. Rev. B 83, 075307 (2011).

[26] P. Wei, S. Tixier, M. Chicoine, S. Francoeur, A. Mascarenhas, T. Tiedje, F. Schiettekatte, Nucl. Instr. and Meth. in Phys. Res. B 219-220, 761 (2004).

[27] S.G. Spruytte, C.W. Coldren, J.S. Harris, W. Wampler, P. Krispin, K.H. Ploog, and M.C. Larson, J. Appl. Phys. 89, 4401 (2001).

[28] E.V. Rao, A. Ougazzaden, Y. Le Bellego, and M. Juhel, Appl. Phys. Lett. 72, 1409 (1998).

[29] H.P. Xin, K.L. Kavanagh, M. Kondow, and C.W. Tu, J. Cryst. Growth 201, 419 (1999).

[30] I.A. Buyanova, W.M. Chen, and B. Monemar, MRS Internet J. Nitride Semicond. Res. 6, 2 (2001).

[31] M. Zinke-Allmang, L.C. Feldman, and M.H. Brabow, Surf. Sci. Rep. 16, 377 (1992),

[32] K. Nozawa, M. H. Delville, H. Ushiki, P. Panizza, and J. P. Delville, Phys. Rev. E 72 (2005).

[33] J.-H. Wu, Ph.D. Thesis, University of Michigan, Ann Arbor, 2013.

[34] G. Vardar, S.W. Paleg, M.V. Warren, M. Kang, S. Jeon, and R.S. Goldman, Appl. Phys. Lett. 102, 042106 (2013).

# Appendix A

# Growth Parameters for GaAsBi Films

## A.1. Overview

In this section, GaAsBi growth parameters are tabulated for growth using $As_4$ (Sec. A.2) and $As_2$ (Sec. A.3).

## A.2 GaAsBi growth using $As_4$

**Table A.1:** Growth parameters for GaAsBi:(Si) films grown using $As_4$, including growth rate, epilayer thickness, substrate temperature, As/Ga beam-equivalent pressure (BEP) ratio, Bi/Ga BEP ratio, V/III BEP ratio, and Si cell temperature for GaAsBi:(Si) films of various Bi fractions, *y*.

| GaAsBi:(Si) grown with $As_4$ | | | | | | | | | |
|---|---|---|---|---|---|---|---|---|---|
| | CMBE | *y* | Growth Rate (μm/hr) | Epilayer Thickness (nm) | Substrate Temperature (°C) | As/Ga BEP Ratio | Bi/Ga BEP Ratio | V/III BEP Ratio | Si Cell Temperature (°C) |
| undoped | 37 | 0 | 1.2 | 400 | 280 | 20.0 | 0 | 20 | |
| | 30 | 0.036 | 1.2 | 400 | 280 | 20.0 | 0.44 | 20.44 | |
| | 32 | 0.007 | 1.2 | 400 | 280 | 20.0 | 0.1 | 20.1 | |
| | 33 | 0.016 | 1.2 | 400 | 280 | 20.0 | 0.2 | 20.2 | |
| | 34 | 0.021 | 1.2 | 400 | 280 | 20.0 | 0.3 | 20.3 | |
| | 36 | 0.048 | 1.2 | 400 | 280 | 20.0 | 0.58 | 20.58 | |
| *n*-type | 45 | 0 | 1.2 | 400 | 280 | 20.0 | 0 | 20 | 1150 |
| | 46 | 0.0076 | 1.2 | 400 | 280 | 20.0 | 0.1 | 20.1 | 1150 |
| | 65 | 0.0080 | 1.2 | 400 | 280 | 15.0 | 0.1 | 15.1 | 1150 |
| | 93 | 0.017 | 0.45 | 400 | 280 | 10.0 | 0.2 | 10.2 | 1250 |
| | 92 | 0.018 | 0.28 | 400 | 280 | 10.0 | 0.2 | 10.2 | 1250 |
| | 62 | 0.019 | 1.2 | 400 | 280 | 15.0 | 0.2 | 15.2 | 1250 |
| | 47 | 0.021 | 1.2 | 400 | 280 | 20.0 | 0.3 | 20.3 | 1150 |
| | 48 | 0.060 | 1.2 | 400 | 280 | 20.0 | 0.6 | 20.6 | 1150 |
| *p*-type | 66 | 0 | 1.2 | 400 | 280 | 10.0 | 0 | 10 | 1250 |
| | 67 | 0.0092 | 1.2 | 400 | 280 | 10.0 | 0.1 | 10.1 | 1250 |
| | 64 | 0.012 | 1.2 | 400 | 280 | 10.0 | 0.1 | 10.1 | 1150 |
| | 63 | 0.023 | 1.2 | 400 | 280 | 6.0 | 0.1 | 6.1 | 1150 |
| | 85 | 0.025 | 1.45 | 400 | 280 | 10.0 | 0.2 | 10.2 | 1250 |
| | 84 | 0.026 | 2.2 | 400 | 280 | 10.0 | 0.2 | 10.2 | 1250 |
| | 86 | 0.026 | 1.45 | 400 | 280 | 10.0 | 0.2 | 10.2 | 1250 |
| | 61 | 0.031 | 1.2 | 400 | 280 | 10.0 | 0.2 | 10.2 | 1250 |
| | 60 | 0.046 | 1.2 | 400 | 280 | 6.0 | 0.2 | 6.2 | 1250 |
| | 68 | 0.051 | 1.2 | 400 | 280 | 10.0 | 0.3 | 10.3 | 1250 |

### A.3 GaAsBi growth using $As_2$

**Table A.2:** Growth parameters for GaAsBi:(Si) films grown using $As_2$, including growth rate, epilayer thickness, substrate temperature, As/Ga beam-equivalent pressure (BEP) ratio, Bi/Ga BEP ratio, V/III BEP ratio, and Si cell temperature for GaAsBi:(Si) films of various Bi fractions, *y*.

| GaAsBi:(Si) grown with $As_2$ | | | | | | | | | |
|---|---|---|---|---|---|---|---|---|---|
| | CMBE | *y* | Growth Rate (μm/hr) | Epilayer Thickness (nm) | Substrate Tem-perat-ure (°C) | As/Ga BEP Ratio | Bi/Ga BEP Ratio | V/III BEP Ratio | Si Cell Temperature (°C) |
| undoped | 772 | 0.029 | 1 | 500 | 300 | 1.5 | 3 | 4.5 | |
| | 809 | 0.008 | 0.1 | 100 | 315 | 5 | 0.05 | 5.05 | |
| | 810 | 0.000 | 0.1 | 100 | 350 | 7.5 | 0.075 | 7.575 | |
| | 811 | 0.000 | 0.1 | 100 | 350 | 10 | 0.1 | 10.1 | |
| | 812 | 0.008 | 0.1 | 100 | 335 | 5 | 0.05 | 5.05 | |
| | 813 | 0.008 | 0.1 | 100 | 335 | 6 | 0.06 | 6.06 | |
| | 816 | 0.000 | 0.1 | 30 | 325 | 7.5 | 0.075 | 7.575 | |
| | 824 | 0.013 | 0.1 | 30 | 315 | 5.0 | 0.05 | 5.05 | |
| | 825 | 0.011 | 0.1 | 30 | 320 | 6 | 0.06 | 6.06 | |
| | 859 | 0.000 | 0.1 | 100 | 350 | 6 | 0.06 | 6.06 | |
| | 860 | 0.000 | 0.35 | 100 | 350 | 6 | 0.06 | 6.06 | |
| | 861 | 0.018 | 0.85 | 100 | 350 | 6 | 0.06 | 6.06 | |
| | 984 | 0.022 | 0.85 | 100 | 350 | 6 | 0.06 | 6.06 | |
| | 987 | 0.020 | 0.35 | 100 | 350 | 6 | 0.06 | 6.06 | |
| | 989 | 0.009 | 0.35 | 100 | 335 | 6 | 0.06 | 6.06 | |
| | 990 | 0.029 | 0.35 | 100 | 315 | 6 | 0.06 | 6.06 | |
| | 1000 | 0.020 | 0.85 | 30 | 335 | 6 | 0.06 | 6.06 | |
| | 1001 | 0.036 | 0.85 | 100 | 335 | 6 | 0.06 | 6.06 | |
| | 1002 | 0.025 | 0.85 | 200 | 335 | 6 | 0.06 | 6.06 | |
| | 1003 | 0.020 | 0.85 | 300 | 335 | 6 | 0.06 | 6.06 | |
| *n*-type | 850 | 0.000 | 0.1 | 200 | 350 | 6 | 0 | 6 | 1265 |
| | 851 | 0.001 | 0.1 | 200 | 350 | 6 | 0.03 | 6.03 | 1265 |
| | 852 | 0.003 | 0.1 | 200 | 350 | 6 | 0.06 | 6.06 | 1265 |

# Appendix B

# Data Analysis

## B.1 Overview

This appendix describes non-standard methods of data analysis used in this dissertation work which are not described in the text. These include an approximation calculation for determining Bi fraction, $y$, from Rutherford backscattering spectroscopy data (Sec. B.2), image enhancement techniques for dim reflection high-energy electron diffraction images (Sec. B.3), and size analysis procedures for surface droplet analysis (Sec. B.4).

## B.2 Rutherford backscattering spectroscopy analysis

### B.2.1 Overview

The N and Bi fractions of GaAsN and GaAsBi films were measured using Rutherford backscattering spectroscopy (RBS) in conjunction with simulation of nuclear reaction analysis code (SIMNRA). The simulation results can be compared with an approximation method. This section presents the details of the approximation method for GaAsBi films.

For RBS spectra taken at a given scattering angle, the scattering signals from elements at the film surface occur at specific energies characteristic to the atomic mass of the target element. Scattering yields from atoms below the film surface have lower energy, due to secondary scattering within the bulk of the film. In Figs. B.1 and B.2, we show RBS spectra for thin and thick GaAsBi films, respectively. Scattering from thin GaAsBi films (Fig. B.1) produces a sharp Bi peak. On the other hand, for thick GaAsBi films, the Bi peak is broadened to lower energies (Fig. B.2). Ga and As have similar atomic masses; thus, scattering from Ga and As occurs at comparable and indistinguishable energies. Furthermore, scattering from Ga and As are extensively broadened to lower energies due to the thick GaAs substrate. For the purpose of this analysis, we define GaAsBi films as "thin" ("thick") if the Bi peak merges (does not merge) into the Ga/As peaks. The analysis is treated differently for these two cases, as described below.

### B.2.2 Background

We now present an approximation calculation for determining Bi fraction from Rutherford backscattering spectroscopy (RBS) data. For $GaAs_{1-y}Bi_y$ film, the number of Ga, As, and Bi atoms experiencing a scattering event can be expressed as

$$N_{Ga} = 0.5\, N\,, \tag{B.1}$$

$$N_{As} = 0.5\,(1 - y)\, N\,, \tag{B.2}$$

and

$$N_{Bi} = 0.5\, y\, N\,, \tag{B.3}$$

where $N$ is the total number of atoms on the film surface exposed to the ion beam. The cross-section, $\sigma_i$, for a scattering event from one target of an element with atomic mass $Z_i$ is given by[1]

$$\sigma_i(\vartheta) = \left(\frac{Z_i Z_B e^2}{4E}\right)^2 \csc^4\left(\frac{\vartheta}{2}\right)\,, \tag{B.4}$$

where $Z_B$ is the atomic mass of beam nuclei, $E$ is the energy of the beam nuclei, $e$ is the electron charge, and $\vartheta$ is the scattering angle. The number of scattered particles from a single target is given by the integrated cross-section

$$(\sigma_T)_i = \int \sigma_i(\Omega)\, d\Omega = AZ_i^2\,, \tag{B.5}$$

where we integrate over the solid angle of the detector and $A$ is a proportionality constant. The total intensity for scattering from all targets of a given element is then

$$I_i = (\sigma_T)_i N_i = AZ_i^2 N_i\,. \tag{B.6}$$

Scattering from GaAsBi films can then be expressed as

$$I_{Ga} = AZ_{Ga}^2[0.5N]\,, \tag{B.7}$$

$$I_{As} = AZ_{As}^2[0.5(1-y)N] \quad \text{(B.8)}$$

and

$$I_{Bi} = AZ_{Bi}^2[0.5yN] \ . \quad \text{(B.9)}$$

The intensity of each element is given by the scattering yield at the surface of the film—i.e., at the high-energy side of the scattering peak from the RBS spectrum. When determining the intensities from RBS data, an estimate of the background is subtracted from the peak energy.

### B.2.3 RBS of thin GaAsBi films

To determine $y$ in thin GaAsBi films (Fig. B.1), we consider the ratio of intensities from the Bi and substrate peaks (containing yields from Ga and As), $R_{\text{thin}}$:

$$R_{thin} = \frac{I_{Bi}}{I_{Ga} + I_{As}} = \frac{6.326y}{1.882 - y} \ . \quad \text{(B.10)}$$

Solving for $y$ yields

$$y = \frac{1.882R_{thin}}{6.326 + R_{thin}} \ . \quad \text{(B.11)}$$

Thus, $y$ can be calculated by measuring the ratio of intensities from the Bi and substrate peaks.

### B.2.4 RBS of thick GaAsBi films

To determine $y$ in thick GaAsBi films (Fig. B.2), we consider the ratio of intensities from the Bi and substrate peaks (containing yields from Ga, As, and Bi), $R_{\text{thick}}$:

$$R_{thick} = \frac{I_{Bi}}{I_{Ga} + I_{As} + I_{Bi}} = \frac{6.326\,y}{1.882 - y + 6.326\,y} \quad . \tag{B.12}$$

Solving for $y$ yields

$$y = \frac{1.882 R_{thick}}{6.326(1 - R_{thick}) + R_{thick}} \quad . \tag{B.13}$$

Thus, $y$ can be calculated by measuring the ratio of intensities from the Bi and substrate peaks

**B.3 Size Analysis**

This section describes the size analysis procedure used in this dissertation work for scanning electron microscopy (SEM) images. For size analysis, particles are detected by adjusting a threshold; thus, care must be taken to prevent detection of noise. The procedure below uses ImageJ software, but can also be done using SPIP. As an example, we will consider size analysis of a $GaAs_{0.954}Bi_{0.046}$:Si film [Fig. B.3(a)].

- The scale bar is cropped from the image.
- The threshold for particle detection is set such that the large droplets are detected and the background is not detected [for example, see the threshold 159 detection of droplets in Fig. B.3(b)]. This eliminates noise introduced by detection at low thresholds, since the resolution of the SEM is smaller than the distance/pixel. Then, the droplets with only the perimeter detected are filled in. For droplets along the image edge, the pixels are manually enclosed.

- The distance is calibrated using a pixel count from the scale bar. The pixel aspect ratio should be taken automatically by ImageJ or SPIP from the image metadata and is dependent on the specific SEM used to collect the data.
- A list containing droplet sizes is produced; the area of each droplet is converted to a droplet diameter, assuming that each droplet is a circle.
- To detect the smaller droplets, the above procedure is repeated at a smaller threshold [for example, see the threshold 86 detection of droplets in Fig. B.3(c)].
- This entire procedure is repeated for SEM images taken from multiple areas of the sample (3 areas preferable), and the resulting lists are combined.
- To determine droplet surface coverage (percent), the area of all the droplets (including droplets on edges) is summed, and then divided by the total area.
- To determine the distribution of droplet diameters, droplets along the image edges are excluded. A histogram of the droplet diameters is produced, using the standard deviation of the droplet diameters as the bin size.[2] For bimodal distributions, there are two peaks, each with their own standard deviation; in this case, each peak is fitted separately.
- For single peaks, the data is fitted to (1) a Gaussian for symmetric peaks, or (2) a log normal distribution for asymmetric peaks. For multiple peaks, Origin's "fit multi-peaks" feature (Gaussian) is used.

## B.4 Enhancement of reflection high-energy electron diffraction images

This section describes the methods used to enhance dim reflection high-energy electron diffraction (RHEED) images, so that dim RHEED patterns can be distinguished

above background levels. This method may also be applied to other image types, such as atomic force microscopy or scanning electron microscopy images. Additionally, this procedure can be used to enhance images prior to size analysis, as described in Sec. B.3.

- The original RHEED image is exported with as much bit depth as possible, in order to maximize the number of bits between the signal and background (16-bit or higher is preferable). In this dissertation work, the kSA software limited the output to 8-bit image files.
- Photoshop, or other image editing software (such as Lightroom), is used to increase the exposure, recovery, fill lights, brightness, and/or contrast of the image, with the goal of making the RHEED pattern more visible. Note that different software may use different terminology for these functions; however, the goal is to increase the light curve. Additionally, the light curve is manually adjusted, so that lights, mediums, and darks may be increased at different rates. The goal here is to increase the signal more than the background, thereby maximizing the bit depth between the signal and background.
- To further increase the bit depth, layer blending is completed in Photoshop. The image must be in RGB color mode, and is blended with itself in two layers (the original layer is duplicated). Different layer-blending algorithms may increase (decrease) the signal (background) more than the background (signal). Once the algorithm that most enhances the RHEED pattern is determined, the image is export as a 16-bit file.

### B.5 Figures

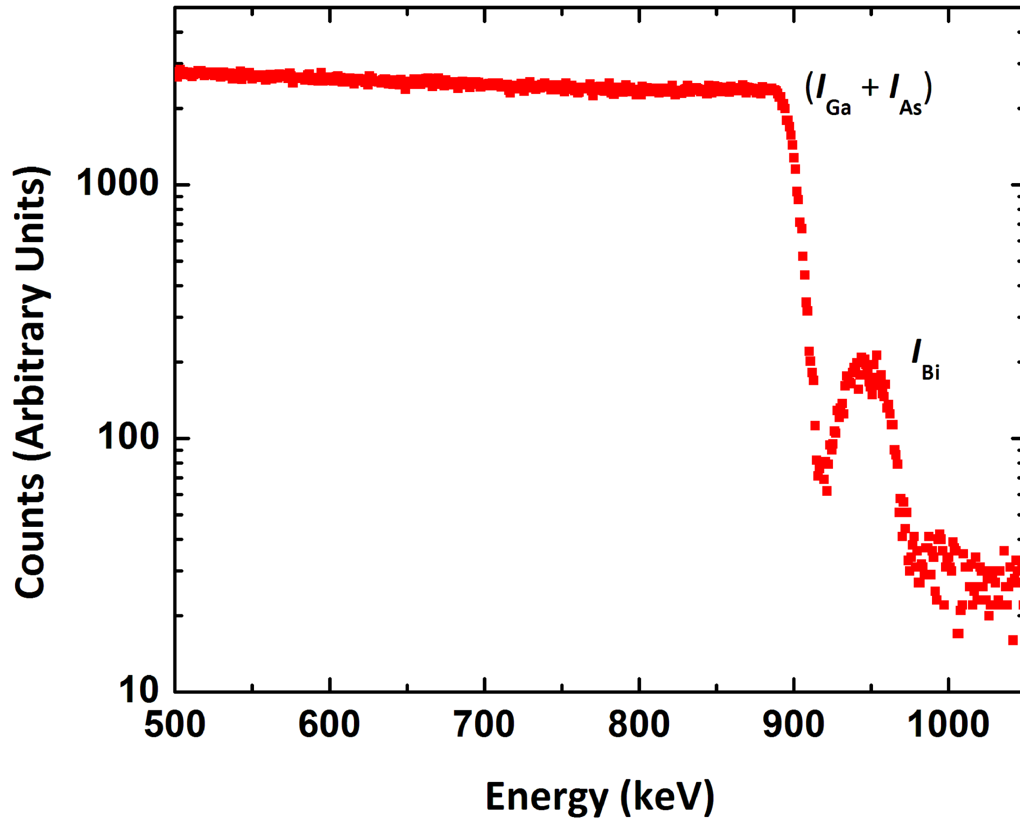


**Figure B.1** Rutherford backscattering data from a thin 200-nm $GaAs_{0.979}Bi_{0.021}$ film: counts of backscattered particles as a function of energy of the backscattered particle. For thin films, counts from the Bi peak ($I_{Bi}$) do not merge into the Ga/As peak ($I_{Ga}$ + $I_{As}$).

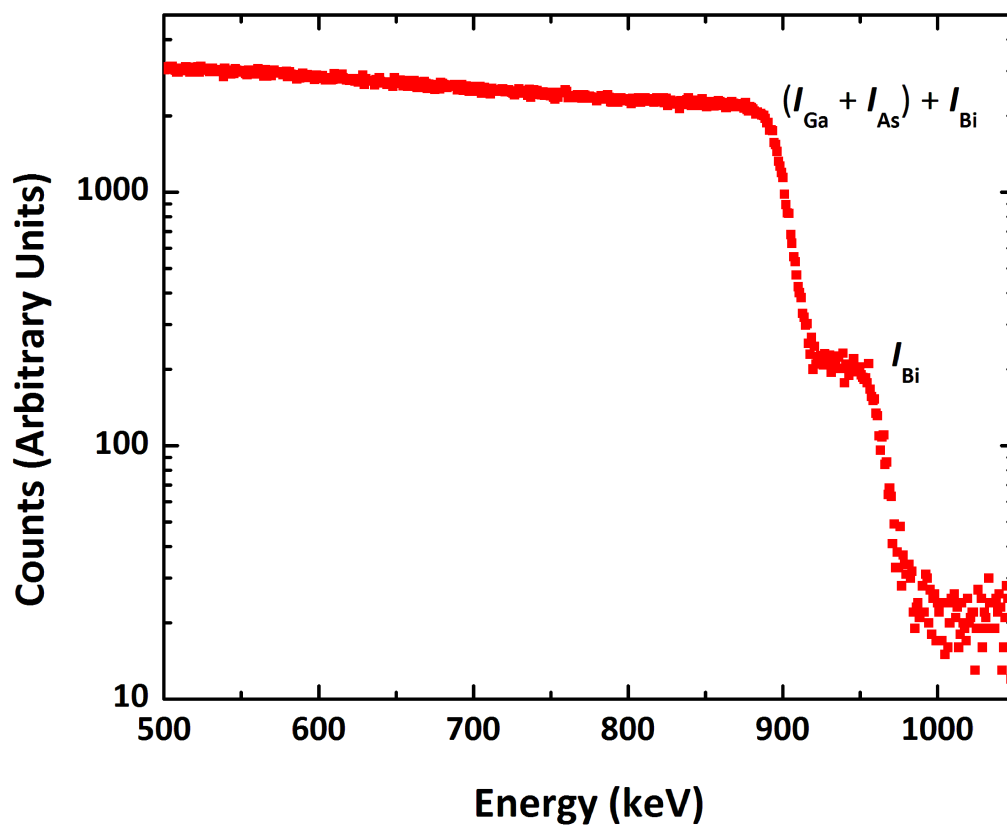


**Figure B.2** Rutherford backscattering data from a thick 300-nm $GaAs_{0.974}Bi_{0.026}$ film: counts of backscattered particles as a function of energy of the backscattered particle. For thick films, counts from the Bi peak ($I_{Bi}$) merge into the Ga/As peak ($I_{Ga} + I_{As}$).

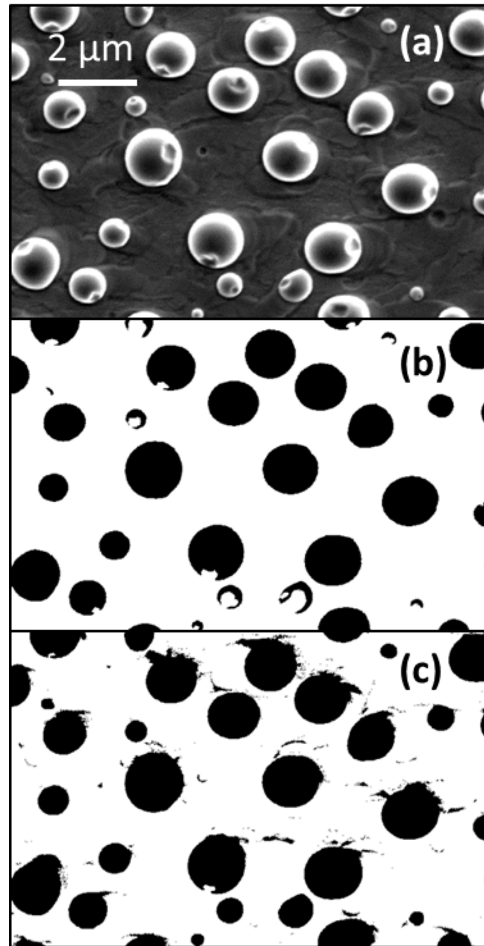


**Figure B.3** Size analysis of a (a) $GaAs_{0.954}Bi_{0.046}$:Si film. (b) For a high threshold, 159, large particles are detected, and small particles are only partially detected. (b) For a low threshold, 86, small particles are detected, but background noise is amplified, especially around larger droplets.

## B.6 References

[1] H. Goldstein, C. Poole, and J. Safko, Classical Mechanics (Addison Wesley, San Francisco, CA, 2002) pp 110.

[2] S. Huang, Ph.D. Thesis, Append. B, University of Michigan, Ann Arbor, 2015.

# Appendix C

# Tabulated Data

## C.1 Overview

In this Appendix, data from various measurements of GaAsN and GaAsBi are tabulated, including high-resolution X-ray rocking curve data (Sec. C.2), Rutherford backscattering spectroscopy data (Sec. C.3), energy dispersive X-ray spectroscopy and Auger electron spectroscopy data (Sec. C.4), size analysis data (Sec. C.5), Hall and resistivity data (Sec. C.6), photoluminescence data (Sec. C.7), GaAsN energy scale data (Sec. C.8), and GaAsN persistent photoconductivity magnitude data (Sec. C.9).

## C.2 X-ray rocking curve data

**Table C.1**: High-resolution X-ray rocking curve data, including (004) peak separation, (224) peak separation, in-plane lattice parameter, $a_{\parallel}$, out-of-plane lattice parameter, $a_{\perp}$, (004) GaAsBi peak width, and (224) GaAsBi peak width, for GaAsBi:Si films of various Bi fractions, *y*.

GaAsBi:(Si)

| Dopant type | CMBE | *y* | (004) peak separation (arcseconds) | (224) peak separation (arcseconds) | $a_{\parallel}$ (Å) | $a_{\perp}$ (Å) | (004) GaAsBi peak width (arcseconds) | (224) GaAsBi peak width (arcseconds) |
|---|---|---|---|---|---|---|---|---|
| | 37 | 0 | | | 5.65338 | 5.65338 | | |
| | 32 | 0.007 | -219.4 | -360 | 5.65365 | 5.66259 | 40 | 70 |
| | 33 | 0.016 | -478.5 | -789.44 | 5.65325 | 5.67366 | 45 | 64 |
| undoped | 34 | 0.021 | -630.9 | -1035 | 5.65338 | 5.6801 | 54 | 69 |
| | 30 | 0.036 | -1065.2 | -1751.4 | 5.65403 | 5.69873 | 47 | 94 |
| | 36 | 0.048 | -1360.05 | -2152.7 | 5.66242 | 5.70694 | 392 | 395 |
| | 45 | 0 | | | 5.65338 | 5.65338 | | |
| | 46 | 0.0076 | -200.33 | -330.01 | 5.65331 | 5.66184 | 42 | 66 |
| | 65 | 0.0080 | -268.21 | -441.11 | 5.65341 | 5.66472 | 41 | 65 |
| | 93 | 0.017 | -474.713 | -778.9445 | 5.65362 | 5.67537 | 75 | 126 |
| *n*-type | 92 | 0.018 | -495.29 | -802.162 | 5.6548 | 5.67394 | 50 | 77 |
| | 62 | 0.019 | -518.592 | -854.5665 | 5.65325 | 5.67535 | 97 | 158 |
| | 47 | 0.021 | -557.68 | -917.5 | 5.65348 | 5.67701 | 55 | 87 |
| | 48 | 0.060 | -1283.25 | -2013.8 | 5.66943 | 5.70812 | 576 | 547 |
| | 66 | 0 | | | 5.65338 | 5.65338 | | |
| | 67 | 0.0092 | -295.8485 | -488.289 | 5.65315 | 5.66589 | 164 | 255 |
| | 67 etch | 0.0092 | -284.0315 | -469.9605 | 5.65297 | 5.66539 | 146 | 227 |
| | 64 | 0.012 | -354.97 | -578.056 | 5.6435 | 5.6684 | 182 | 268 |
| | 63 | 0.023 | -602.97 | -981.9 | 5.65511 | 5.67894 | 253 | 392 |
| *p*-type | 85 | 0.025 | -644.297 | -1059.75 | 5.65357 | 5.68071 | 214 | 348 |
| | 84 | 0.026 | -677.095 | -1113.05 | 5.65369 | 5.68211 | 296 | 430 |
| | 86 | 0.026 | -671.243 | -1099.7 | 5.65428 | 5.68186 | 266 | 403 |
| | 61 | 0.031 | -788.07 | -1298.6 | 5.66275 | 5.687 | 263 | 314 |
| | 60 | 0.046 | -1119.9 | -1840.15 | 5.65428 | 5.70108 | 340 | 570 |
| | 68 | 0.051 | -1225.9 | -2004.95 | 5.65591 | 5.70565 | 515 | 731 |

### C.3 Rutherford backscattering spectroscopy data

**Table C.2**: Rutherford backscattering spectroscopy determination of the Bi fraction, $y$, for various GaAsBi:(Si) films.

| GaAsBi:(Si) | | |
|---|---|---|
| Dopant type | CMBE | $y$ |
| undoped | 32 | 0.008 |
| | 33 | 0.019 |
| | 34 | 0.023 |
| | 30 | 0.034 |
| | 36 | 0.053 |
| *n*-type | 46 | 0.0076 |
| | 47 | 0.021 |
| | 48 | 0.060 |

## C.4 Energy dispersive X-ray spectroscopy and Auger electron spectroscopy data

**Table C.3**: Droplet compositions of surface droplets on GaAsBi:Si films of various Bi fractions, $y$, as determined by X-ray spectroscopy (EDX) and/or Auger electron spectroscopy (AES).

| GaAsBi:Si | | | | |
|---|---|---|---|---|
| Dopant type | CMBE | $y$ | Droplet Composition | Method |
| *n*-type | 65 | 0.008 | Ga-Bi | AES |
| | 62 | 0.019 | Ga-Bi | AES |
| *p*-type | 66 | 0 | Ga | AES |
| | 67 | 0.0092 | Ga or Ga-Bi | EDX, AES |
| | 67 etch | 0.0092 | craters | EDX, AES |
| | 85 | 0.025 | Ga-Bi | AES |
| | 84 | 0.026 | Ga-Bi | AES |
| | 86 | 0.026 | Ga-Bi | AES |
| | 60 | 0.046 | Ga-Bi | AES |
| | 68 | 0.051 | Ga-Bi | EDX |

### C.5 Size analysis data

**Table C.4**: Droplet surface coverage for GaAsBi:Si films of various Bi fractions, *y*.

| GaAsBi:Si | | |
|---|---|---|
| CMBE | *y* | Droplet Surface Coverage (Fraction) |
| 67 | 0.0092 | 21.0 |
| 84 | 0.026 | 15.7 |
| 60 | 0.046 | 24.7 |
| 68 | 0.051 | 18.3 |

### C.6 Hall and resistivity data

**Table C.5**: Room-temperature dopant type, resistivity, $\rho$, free carrier concentration, $n$, and mobility, $\mu$, for GaAsBi:Si films of various Bi fractions, $y$.

| GaAsBi:Si | | | | | |
|---|---|---|---|---|---|
| Dopant type | CMBE | $y$ | $\rho$ ($\Omega$-cm) | $n$ ($\times 10^{18}$ cm$^{-3}$) | $\mu$ (cm$^2$/Vs) |
| *n*-type | 45 | 0 | 0.0031 | 0.81 | 2438 |
| | 46 | 0.0076 | 0.0032 | 0.77 | 2505 |
| | 65 | 0.0080 | 0.0038 | 0.79 | 2385 |
| | 93 | 0.017 | 0.0098 | 2.64 | 241 |
| | 92 | 0.018 | 0.0100 | 4.00 | 156 |
| | 62 | 0.019 | 0.0109 | 0.98 | 587 |
| | 47 | 0.021 | 0.0096 | 0.35 | 1879 |
| | 48 | 0.060 | highly resistive | | |
| *p*-type | 66 | 0 | 0.0327 | 3.97 | 48 |
| | 67 | 0.0092 | 0.1070 | 1.88 | 31 |
| | 67 etch | 0.0092 | 0.0959 | 2.33 | 28 |
| | 64 | 0.012 | 0.3194 | 0.30 | 64 |
| | 63 | 0.023 | 0.4660 | 0.19 | 69 |
| | 85 | 0.025 | 0.0391 | 4.08 | 39 |
| | 84 | 0.026 | 0.0550 | 2.36 | 48 |
| | 86 | 0.026 | 0.0181 | 10.20 | 34 |
| | 61 | 0.031 | 0.0409 | 4.64 | 33 |
| | 60 | 0.046 | 0.0308 | 4.94 | 41 |
| | 68 | 0.051 | 0.0260 | 5.65 | 43 |

### C.7 Photoluminescence data

**Table C6**: Photoluminescence data, including the peak position and full-width-at-half maximum (FWHM), for GaAsBi:Si films of various Bi fractions, *y*, grown using either $As_2$ or $As_4$.

| GaAsBi:(Si) | | | | | |
|---|---|---|---|---|---|
| Arsenic species | Dopant type | Sample Number | *y* | 10-K Peak Energy (eV) | 10-K Peak FWHM (eV) |
| $As_2$ | undoped | RMBE 860 | 0 | 1.41 | 0.08 |
| | | RMBE 813 | 0.0076 | 1.39 | 0.03 |
| | | RMBE 809 | 0.0077 | 1.36 | 0.04 |
| | | RMBE 812 | 0.0078 | 1.32 | 0.10 |
| | | RMBE 1003 | 0.020 | 1.25 | 0.07 |
| $As_4$ | undoped | CMBE 32 | 0.007 | 1.27 | 0.09 |
| | | CMBE 33 | 0.016 | 1.29 | 0.08 |
| | | CMBE 34 | 0.021 | 1.21 | 0.19 |
| | | CMBE 30 | 0.036 | 1.16 | 0.27 |
| | *n*-type | CMBE 46 | 0.0076 | 1.29 | 0.13 |
| | *p*-type | CMBE 67 | 0.0092 | 1.27 | 0.17 |
| | | CMBE 61 | 0.031 | 1.24 | 0.06 |

### C.8 GaAsN energy scales

**Table C.7**: Activation energy, $E_a$, and electron-capture barrier, $E_c$, for GaAsN:Si films of various N fractions, $x$.

| GaAsBi:Si | | | | |
|---|---|---|---|---|
| RMBE | $x$ | Dopant | $E_a$ (eV) | $E_c$ (eV) |
| 584 | 0.0075 | Te | 105 | 250 |
| 583 | 0.01 | Te | 99 | 290 |
| 596 | 0.013 | Te | 93 | 330 |
| 597 | 0.013 | Si | 92 | 230 |
| 581 | 0.015 | Si | 61 | 330 |
| 598 | 0.019 | Te | 73 | 270 |

## C.9 GaAsN persistent photoconductivity magnitude

**Table C.8**: Persistent photoconductivity magnitude (the increase in conductivity following the termination of illumination, normalized to the preillumination conductivity), for GaAsN:Si films of various N fractions, *x*.

| GaAaN:Si | | |
|---|---|---|
| RMBE | *x* | PPC Magnitude |
| 850 | 0 | 0.005 |
| 597 | 0.0013 | 0.005 |
| 425 | 0.0022 | 0.005 |
| 445 | 0.0048 | 0.018 |
| 421 | 0.0067 | 0.052 |
| 444 | 0.0082 | 1.01 |
| 420 | 0.01 | 0.72 |
| 426 | 0.012 | 0.77 |
| 446 | 0.013 | 2.2 |
| 581 | 0.015 | 5.1 |
| 581 anneal | 0.015 | 3.0 |

## Appendix D

## Hall Bar Photolithography Process

This section describes the photolithography process used to fabricate Hall bar devices. This process requires the GaAs bay spinner station and the MJB3 Mask Aligner in the Lurie Nanofabrication Facility at the University of Michigan.

- The sample is cleaned with Acetone and Isopropanol, and then dried with $N_2$.
- The sample is mounted on a glass slide, using a couple of drops of S1813 photoresist as an adhesive. The photoresist is then baked on a hot plate for 2-3 minutes between 110 and 130 °C to solidify the photoresist.
- The sample surface is coated with photoresist (2-4 drops of S1813), spun at 4000 rpm for 30 sec. and then baked for 3-4 minutes between 110 and 130 °C (the time may vary depending on the sample).
- The photoresist is exposed for 6 seconds in the MJB-3.
- The photoresist is developed for 60 seconds in MF-319 developer (not diluted), gently moving the sample back and forth. Then, the sample is rinsed in deionized water for 30 seconds, gently moving the sample back and forth.
- The photolithography is verified by examining the sample under a microscope, to ensure that the Hall bar is fully developed. If the Hall bar is not fully defined, the sample is developed in MF-319 for additional time.

# Appendix E

## Contact Error in Van der Pauw Measurements

### E.1 Overview

In this section, we quantify contact error in the resistivity, $\rho$, and the Hall coefficient, $R_H$, for samples prepared in the Van der Pauw geometry.[1]

### E.2. Contact error in Van der Pauw samples

Figure E.1 shows a schematic for contacts that are finite in size, or not along the sample perimeter, for a sample of diameter $D$. For a contact which is extended a length $l$ along the perimeter [Fig. E.1(a)], the errors in the resistivity, $\Delta\rho$, and Hall coefficient, $\Delta R_H$, are given by

$$\frac{\Delta\rho}{\rho} \approx \frac{-l^2}{16D^2 \ln 2}, \tag{E.1}$$

and

$$\frac{\Delta R_H}{R_H} \approx \frac{-2l}{\pi^2 D}. \tag{E.2}$$

For a contact extended radially by a length $l$ [Fig. E.1(b)], $\Delta\rho$ and $\Delta R_H$ are given by

$$\frac{\Delta\rho}{\rho} \approx \frac{-l^2}{4D^2 \ln 2} \ , \tag{E.3}$$

and

$$\frac{\Delta R_H}{R_H} \approx \frac{-4l}{\pi^2 D} \ . \tag{E.4}$$

Finally, for a contact removed from the sample edge by a distance $l$ [Fig. E.1(c)], $\Delta\rho$ and $\Delta R_H$ are given by

$$\frac{\Delta\rho}{\rho} \approx \frac{-l^2}{2D^2 \ln 2} \ , \tag{E.5}$$

and

$$\frac{\Delta R_H}{R_H} \approx \frac{-2l}{\pi^2 D} \ . \tag{E.6}$$

### E.3 Figures

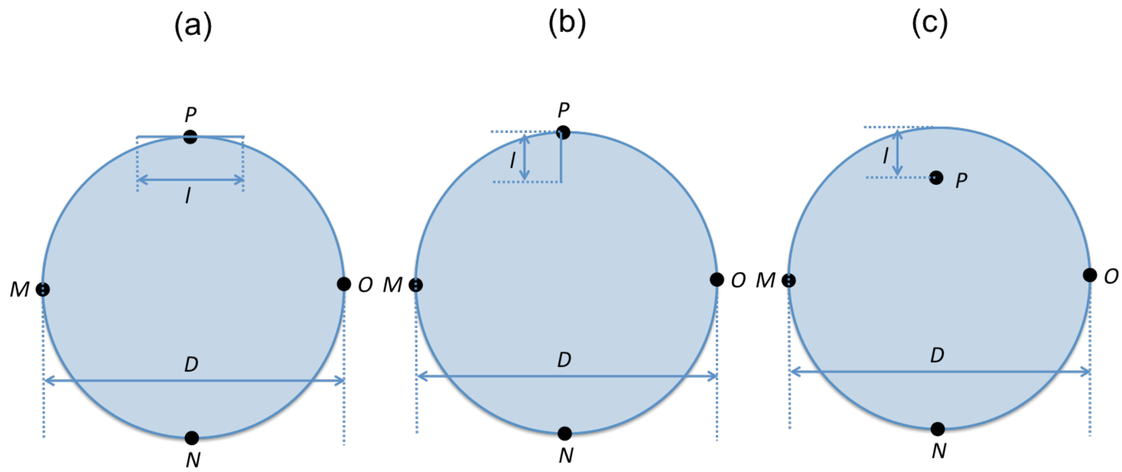


**Figure E.1** Non-ideal Van der Pauw samples: (a) a contact is extended along the perimeter, (b) a contact is extended radially, and (c) a contact is not on the sample edge.

## E.4 References

[1] L.J. van der Pauw, Philips Res. Repts. 26, 220 (1958).